AAPM REPORT NO. 202

Physical Uncertainties in the Planning and Delivery of Light Ion Beam Treatments

The Report of AAPM
Task Group 202

March 2020

Physical Uncertainties in the Planning and Delivery of Light Ion Beam Treatments

The Report of AAPM Task Group 202

Michael F. Moyers[1], Thomas L. Toth[2], Ramaswamy Sadagopan[3], Alexei Chvetsov[4],
Jan Unkelbach[5], Radhe Mohan[3], David A. Lesyna[6], Liyong Lin[7],
Zuofeng Li[8], Falk Poenisch[3], Wayne D. Newhauser[9],
Stanislav M. Vatnitsky[10], and Jonathan B. Farr[11]

---

[1] Shanghai Proton and Heavy Ion Center, Shanghai, China
[2] Plexar Imaging, Shaker Heights, OH
[3] The University of Texas M. D. Anderson Cancer Center, Houston, Texas
[4] University of Washington, Seattle, WA
[5] Massachusetts General Hospital, Boston, MA
[6] Optivus Proton Therapy, San Bernardino, CA
[7] Emory University, Atlanta, GA
[8] University of Florida, Jacksonville, FL
[9] Louisiana State University, Baton Rouge, LA, and Mary Bird Perkins Cancer Center, Baton Rouge, LA
[10] MedAustron, Wiener Neustadt, Austria
[11] Applications of Detectors and Accelerators to Medicine, Meyrin, Switzerland

ISBN: 978-1-936366-70-5
ISSN: 0271-7344

Published by

American Association of Physicists in Medicine
1631 Prince Street
Alexandria, VA 22314

Contents

Abstract

Light ion beam treatments are becoming more widely used. Safe and optimal treatments may only be achieved when uncertainties are considered at every step of the planning and delivery process. These uncertainties include, but are not limited to, penetration uncertainties due to beam delivery, uncertainties in dose compliance, uncertainties of x-ray computed tomography numbers, absolute and relative linear stopping powers, absolute and relative linear scattering powers, conversion of x-ray computed tomography numbers to relative linear stopping power, lateral alignment uncertainties, and uncertainties due to inter-fractional and intra-fractional anatomical variations. Knowing the source and magnitude of these uncertainties, the planner must optimize the plans to mitigate the effect of these uncertainties as much as possible without making the plan undeliverable. Visualization of dose distributions considering the effects of these uncertainties is an important step in evaluating the safety and effectiveness of the plans. This report by Task Group 202 of the AAPM has endeavored to address each of these topics as a guide to the user of light ion beam treatments.

1. Introduction

1.1 Background

Between 1954 and 1990, approximately 13,000 patients were treated with a variety of light ion and pion beams at a number of research centers around the world. During this period, techniques for planning and delivering charged particle beams were developed and refined in a conservative and deliberate fashion so that no patients were harmed. In 1990, the first hospital-based center was opened, and since that time several other hospital or clinic-based centers have opened. This move out of the laboratory setting allowed patients with all types of diseases and sites to be treated in a routine fashion. At the same time, because the patient load at each facility was gradually increasing, the staff was able to learn the intricacies of light ion treatments from the pioneers in the field who developed the planning and delivery techniques. Within the next several years, the number of light ion facilities is expected to increase, and the patient load at each facility is expected to rise much more quickly than in the previous eras of exploratory treatment. Individual-based education and training during a gradual patient buildup is no longer practical and will no longer sustain the demand for educated and trained medical physicists and support staff. Since each step of planning and delivering light ion beam treatments involves uncertainties—both human and technology-based—it is important to understand the nature of these uncertainties and their propagation into all of the stages of the treatment process. The purpose of this report is to provide a readily available resource that provides a description of typical physical uncertainties encountered in light ion beam treatments and basic information to minimize the effects of those uncertainties when optimizing plans to provide safe treatments to patients.

1.2 Scope

Light ions are considered to be ions with atomic numbers less than 20 (Blakeley et al., 1986; Chu et al., 1993; Wambersie et al., 2004). Although six different ions have been used for human treatments, as of 2013 the majority of patients have been treated with protons (>83,000), helium ions (>2,100), and carbon ions (>8,800) (Vatnitsky and Moyers, 2013). The planning and delivery of treatments with the different light ion beams is nearly identical—except for differences in radiobiological effectiveness (RBE)—but there are several key differences compared to the planning and delivery of treatments with megavoltage x-ray beams. The primary differences between light ion and megavoltage x-ray beam planning and delivery are the necessity of explicitly accounting for, on a portal-by-portal basis, geometrical uncertainties that affect alignment of the beams with the patient tissues and radiological uncertainties that affect the penetration of the light ions through beamline devices and patient tissues. Typically the lateral uncertainties also affect the radiological uncertainties. This report addresses physical uncertainties and how these uncertainties are used for applying margins and optimizing plans. This report does not address issues such as determination of the target or normal tissue volumes, which are often considered the weakest links in the search for accuracy (Njeh, 2008), nor how the RBE values should be applied to different tissues for different radiation characteristics (such as linear energy transfer) and fractionation schemes. Although the magnitude of biological uncertainties can be much larger than physical uncertainties, the consequence of physical uncertainties can result in a geometric miss with more than a 100% error in dose, especially when adjacent or abutting portals are involved.

The reader should already have familiarity with light ion beam treatments before reading this report. Several useful references concerning light ion therapy include Moyers and Vatnitsky (2012), Delaney and Kooy (2008), Paganetti (2012), and Linz (2012). A couple of useful references concerning uncertainties in radiation therapy include Van Dyk (2013) and Palta and Mackie (2011).

In addition to the physical uncertainties that are the topic of this report, another issue that impacts the accuracy and safety of light ion beam treatments is uncertainty in terminology. Often different facilities use different terms to describe the same thing, and sometimes a single term is used to describe different things at different facilities. Some jargon is also contradictory to the common denotations and connotations of the English language. This report has attempted to use terminology in a consistent and logical manner and correctly supported by the English language. A list of acronyms is provided in an appendix.

An uncertainty category not addressed in this report is a consequence of the small light ion teletherapy user base. The various control systems—including both hardware and software used for planning, alignment, and delivery—are used by only tens of people rather than thousands of people. This means that bugs and errors in the systems and in the operational procedures are much more likely to go unnoticed for a long time, but they may have severe consequences when they occur. Compared to procedures used for megavoltage x-ray and electron teletherapy, extra vigilance is required for acceptance testing, commissioning, and routine QA of light ion teletherapy equipment. In planning, larger margins and other mitigation strategies may need to be applied to promote safety.

1.3 Charge of Task Group

When the American Association of Physicists in Medicine (AAPM) leadership formed the Working Group on Particle Beams (WGPB), it was believed that the experience in designing portals to treat targets and protect normal tissues had not been well documented. This was mainly due to a lack of widespread interest (i.e., most journal readers did not have ion beams) and, therefore, much of the work and information performed at the few existing facilities treating patients was never published in the open literature and only available in internal documents. It was felt that without this information new facilities could waste too much time and effort "reinventing the wheel." The WGPB believed that collecting and disseminating previous methods and data would promote patient safety while assisting facilities in reaching their necessary patient throughput goals. Due to the paucity of information regarding physical uncertainties and planning techniques at the time of its inception, the task group was charged with not only reviewing published literature, but also investigating and collating unpublished data and past and current practices from light ion facilities that had been treating patients for many years. With regard to the magnitude of uncertainty values, when consensus was available, the task group would determine the typical values. When consensus was not available, the range of values would be given.

During the formation of the task group, it was suggested that members new to the field of light ion teletherapy should be polled as to what they felt was needed, while experienced members would provide much of the information. This procedure was useful in determining what was and was not important for inclusion into the report. The content of the report follows the outline approved by the AAPM Therapy Physics Committee (TPC), although the names of some sections have been changed and the sections have been reordered to improve continuity.

In light of the information needs described above, it was recommended that the task group write two separate but related documents: a full-length report to be published online at the AAPM website and a relatively brief executive summary to be published in the journal *Medical Physics*. This dissemination practice, as recommended by the Therapy Physics Committee of the AAPM at the time of inception of Task Group 202, is to provide, free of charge, a full-length report detailing the scientific and technical information needed by practicing medical physicists (given in the task group's charge approved by the AAPM leadership in 2010) and a short executive summary to alert readers of the journal *Medical Physics* of the existence of the full-length report and to concisely introduce its contents. Both of these documents comply with AAPM guidelines and precedents for task group reports, including scope and length. The task group's full-length report was reviewed and approved by the Working Group on Particle Beams, Treatment Delivery Subcommittee, Therapy Physics Committee, and Scientific Council. The executive summary was separately reviewed by the same groups and additionally reviewed using established editorial procedures at the publishing journal. To keep the information presented in the report fresh and relevant, it is anticipated that the online report will be periodically updated by a standing committee of the AAPM.

2. Types of Uncertainties

2.1 Definitions

Optimized and safe planning and delivery of light ion beam treatments requires an understanding of the physical uncertainties associated with each process, such as applying margins around targets and critical normal tissues (organs at risk), establishing tolerances for beam delivery, and setting up quality improvement program corrective actions. This section provides a basic review of different types of uncertainties and their propagation. Those with a firm command of uncertainty propagation may wish to skip this section.

The first part of understanding uncertainties is to clearly distinguish accuracy from precision or reproducibility. The term accuracy expresses the proximity of the result of a measurement to the true value of the measured quantity. In theory, accuracy could be expressed in terms of the difference between the measured value and the true value of the quantity but, of course, this number is never known. An adequate uncertainty budget thus gives an indication of the accuracy. Accuracy represents the bias between the average measured value and the true value. Precision represents the spread of the measured values and is a synonym for either the repeatability or reproducibility. Figure 1 illustrates these concepts.

Reproducibility is the closeness of the agreement between the results of measurements (usually understood to be corrected) of the same quantity carried out under changed conditions of measurement. Reproducibility can be expressed as a standard deviation and the changed conditions, which should be specified, may include: principle of measurement, method of measurement, observer, measuring instrument, reference standard, location, conditions of use, and time.

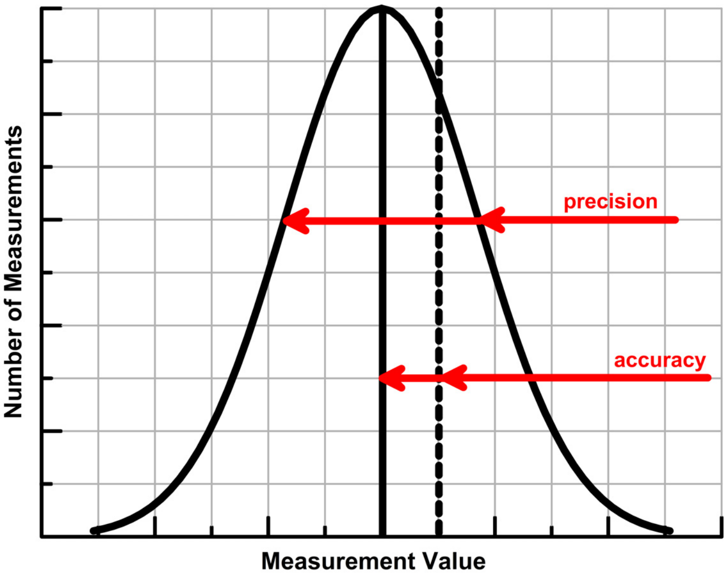

Figure 1. Plot of measurement values of a quantity. The solid vertical line represents the mean value of the measurements. The dotted vertical line represents the true value. The spread of the measured values is the precision while the difference between the average and true values is the accuracy.

Any measured or calculated value has an associated and quantifiable attribute called the uncertainty. Even when all of the known or postulated components of error have been evaluated and corrections have been taken into account, there remains some degree of doubt about the accuracy of the corrected result. This doubt is termed uncertainty. It is important to underscore the distinct and separate concepts represented by the terms “uncertainty” and “error.” An error is defined as a stated result minus its corresponding true value. Because the true value cannot be known exactly, neither can the error nor the uncertainty. The term “uncertainty” is thus commonly used in two senses: to refer to qualitative “doubt” about the accuracy of a result and to refer to “quantitative measures” of the uncertainty of a result. The remainder of this section will focus on the latter.

The physical uncertainties in the planning and delivery of light ion beam treatments originate from many different causes. Historically, these uncertainties were classified as being either random or systematic in nature. Random errors arise presumably from stochastic variations in influence quantities over time and space. Although it is not possible to reduce the random error in any individual measurement or calculation, it is possible to reduce the associated uncertainty by repeating the measurement or calculation. Examples of random uncertainties include x-ray CT image noise and inter-fraction errors in the lateral alignment of the patient and treatment radiation field. Like random errors, systematic errors cannot be eliminated, but it may be possible to reduce the systematic error if the effect can be recognized, quantified, and a correction factor applied to compensate for the systematic effect. Common systematic uncertainties include dosimeter calibration factors and artifacts in kilovoltage x-ray CT images due to metal implants. These and other uncertainties will be examined in detail in subsequent sections of this report. In the remainder of this section, basic aspects of uncertainties will be briefly reviewed, including definitions, nomenclature, and mathematical methods to combine uncertainties, closely following the recommendations published by the International Organization for Standardization (1994) and the Joint Committee for Guides in Metrology (JCGM) (2008), which are widely used in the literature of radiation therapy.

The uncertainty of the result of a particular measurement generally consists of several components which the JCGM (2008) groups into two categories according to the methods used to estimate their numerical values. Both types of uncertainties u(x_i) are based on probability distributions and are quantified by distributions that are models used to represent the state of our knowledge. Type A uncertainties are evaluated by statistical methods and can be estimated from a series of repeated independent observations. For example, the experimental variance of the probability distribution of quantity q is represented by Equation 1:

$$s^2(q_k) = \frac{1}{n-1}\sum_{k=1}^{n}(q_k - \bar{q}_k)^2 \qquad \text{(Eq. 1)}$$

where q_k is the k$^{\text{th}}$ independent individual observation of the quantity q made under the same conditions of measurement, n is the number of observations, and $\bar{q}$ is the average of n observations. Type B uncertainties can only be estimated by an analysis of the process under consideration and assigning reasonable variations to parameters whose uncertainties are not exactly quantifiable. The type B standard uncertainty may be obtained from an assumed probability density function (PDF), usually based on a pool of comparatively reliable information. The information may include previous measurement data, experience, and general knowledge of the equipment and instruments, manufacturer’s specifications, and uncertainties assigned to reference data taken from handbooks. If there is a type B uncertainty, such as a systematic offset, then every effort should be made to eliminate the uncertainty since it is known to be the result of an incorrect procedure. In some situations, however, the user knows a type B uncertainty exists but may not have control over the elimination of the uncertainty. This is typical for a treatment planning system (TPS), where the dose calculation algorithm may have a reproducible deviation from the measured value at certain points within the beam, e.g., at points in or near the penumbra region. It may also be typical of the sag of the radiation head when loaded with accessories of different weights. Although it is recognized that there is a reproducible difference, the user may not be able to adjust for this difference without causing larger differences elsewhere or making the treatment impractical or uneconomical. The established practice of radiotherapy shows that reproducibility of dose delivery is critical when considering one facility and one radiation modality, but when results between facilities or between modalities are compared, some type B uncertainties may also be important. On the other hand, some type B uncertainties may be common to all participants and can, therefore, be omitted from routine consideration, e.g., if all the participants follow the same dosimetry protocol, or if the same basic physics data are used in multiple protocols.

Generally, type A uncertainties are of a random nature from different sources and are added in quadrature. Suppose a measurement or calculation result y is determined by the functional relationship between different quantities given in Equation 2:

$$y = \mathrm{f}(x_1, x_2, ..., x_\mathrm{N}) \qquad \text{(Eq. 2)}$$

where x_1, x_2, …, x_N represent the various input estimates for quantities. In general, the combined standard uncertainty in y, denoted by $\mathrm{u_c}(y)$, depends on the standard uncertainties $\mathrm{u}(x_i)$, each of which may be evaluated individually. The overall uncertainty is a combination of both type A and type B uncertainties. Uncertainties of both type A and B can often be combined in quadrature to provide an estimate of the overall uncertainty (JCGM, 2008). In the special case in which the input quantities are uncorrelated, the combined uncertainty in y, or $\mathrm{u_c}$(y), is given by the square root of the combined variance. The combined variance is given by Equation 3:

$$\mathrm{u}_c^2(y) = \sum_{i=1}^{n} \left(\frac{\delta f}{\delta x_i} \right)^2 u^2(x_i) \qquad \text{(Eq. 3)}$$

where $\frac{\delta f}{\delta x_i}$ is the partial derivative of $f(x_1, x_2, ..., x_N)$ in Equation 2 with respect to x_i and each $u(x_i)$ is the corresponding standard uncertainty. This equation is termed the law of propagation of uncertainty. In the general case where input quantities may be correlated, the law is expressed as given by Equation 4:

$$\mathrm{u}_c^2(y) = \sum_{i=1}^{n} \left(\frac{\delta f}{\delta x_i} \right)^2 u^2(\mathrm{x}_i) + 2\sum_{i=1}^{n-1} \sum_{j=i+1}^{n} \left(\frac{\delta f}{\delta x_i} \right) \left(\frac{\delta f}{\delta x_j} \right) u(\mathrm{x}_i, \mathrm{x}_j) \qquad \text{(Eq. 4)}$$

where $u(x_i, x_j)$ is the estimated covariance associated with x_i and x_j. The degree of correlation may be characterized by the correlation coefficient given in Equation 5:

$$r(x_i, x_j) = \frac{u(x_i, x_j)}{u(x_i)u(x_j)} \qquad \text{(Eq. 5)}$$

where $-1 \le r(x_i, x_j) \le 1$. If $r(x_i, x_j) = 0$, then x_i and x_j are independent of one another and Equation 4 reduces to Equation 3.

The combined standard uncertainty $u_c(y)$ corresponds approximately to the 68% confidence interval. That is to say, $y \pm k_p\, u_c(y)$ encompasses a large fraction ($p = 68.3\%$, $k_p = 1$) of the distribution of values where k_p is the coverage factor. The product $k_p\, u_c(y)$ is called the expanded uncertainty. In many situations in radiotherapy, a coverage factor other than one is applied to increase the confidence interval. Assuming a normal distribution of values, larger confidence intervals that are commonly used include expanded uncertainties of $k_p = 1.5$ ($p = 86.6$), $k_p = 2$ ($p = 95.5$), and $k_p = 3$ ($p = 99.7$).

2.2 Non-normal Distributions

There are many instances in radiation therapy delivery where interlocks are used to truncate possible deviations from an expected value. In many cases, the untruncated distribution follows a normal distribution between the tolerance limits, with truncation occurring only at the far tails of the Gaussian distribution. In these cases, the variance may be calculated normally. In some cases, the untruncated distribution may consist of fairly uniform values between the tolerance limits. In these truncated uniform distribution cases, the variance of the probability distribution of y can be represented by Equation 6 (JGCM, 2008; Castrup, 2009):

$$u^2(y) = \frac{a^2}{3} \qquad \text{(Eq. 6)}$$

where *a* represents the tolerance limit on both sides of the expected value.

2.3 Recommendations

- When reporting an uncertainty, the type of uncertainty should be provided; e.g., Gaussian, truncated Gaussian, truncated uniform, etc.
- The expanded uncertainty should always be presented with the numerical value of the uncertainty; e.g., $k_p = 2$.

3. Penetration Uncertainties Due to Beam Delivery (PUBD)

3.1 Introduction

There are many items associated with beam delivery that contribute to the uncertainty in penetration. The items listed in this section are typically combined into one uncertainty value for use by TPSs in determining proper margins and calculations of "what if" scenarios. Not all discussed items are present in all systems, and the items may behave differently and have different uncertainty values in different TPSs and delivery systems.

3.2 Uniform Range Shifters (URSs)

As of 2014, all commercially available light ion accelerators operating for human treatment were either synchrotron-based or cyclotron-based. Although many cyclotrons can extract beam at many different energies, the current generation of clinical cyclotrons deliver ions at a single energy. Synchrotrons can deliver a multitude of energies. Between 4 and 18,000 discrete energies can be requested by the user (Moyers, 2002) depending upon on the manufacturer. If an accelerator produces only one or a few energies, then so-called uniform range shifter (URS) devices can be inserted into the beam path to decrease the penetration of the entire beam into a patient. Sometimes uniform range shifters (URSs) are used with scanning beams to treat superficial tumors (water-equivalent depths less than 2 to 7.5 cm, depending upon the system) because, although the accelerator may be able to produce and transport a low-energy beam to the patient, low-energy ions scatter more than high-energy ions, resulting in a large penumbra and reduced ability to modulate the fluence distribution. Uniform range shifters may consist of individual slabs of uniform thickness, a set of binary thickness slabs (e.g., thicknesses of 0.5, 1.0, 2.0, 4.0, 8.0, 16.0, or 32.0 mm), or a pair of wedges arranged in a linear or spiral fashion. The uncertainty of the thickness of the slab(s) placed in the beam path must be considered in the overall penetration of the beam into the patient. If the URS is placed upstream near the accelerator or entrance to the radiation head where the beam is narrow, only the thickness of the small area where the beam passes through the slab must be known. If the URS is placed near the patient, then the thickness throughout the entire lateral extent of the slab must be known. The thickness distribution of simple slab URSs can be measured carefully before installation and thereafter periodically. The thickness of upstream binary URSs should be fairly stable and well known. On the other hand, programmable double wedge URSs are susceptible to slippage and backlash of the wedge-positioning apparatus and, thus, a conscientious continuing quality assurance (QA) program or real-time range check must be implemented to maintain a small uncertainty. With all types of URSs, the 2 standard deviation (SD) uncertainty due to URS thickness is generally maintained at less than about 0.2 mm of water.

The beam penetration and its uncertainty may depend strongly on the thickness and elemental composition of URSs. URSs are typically, but not always, made from low-atomic-number (low-Z) materials, such as plastic, to reduce scattering. The amount of range shift depends on many factors, including the elemental composition and mass density. In addition, the range shift depends on the energy of the light ion beam passing through the slab. In lead, the amount of range shift in water produced by a given thickness of lead may vary by several millimeters over the clinically encountered light ion beam energies. In low-Z materials, such as water and plastic, the range shift is virtually independent of effective Z at high energies, but may vary slightly for low energies. Methods to measure and calculate range shift in various materials were reported by Moyers et al. (1992), Moyers et al. (2006), Zhang and Newhauser (2009), Moyers et al. (2010), and Zhang et al. (2010). The user should carefully examine the algorithms associated with URSs, both in the planning and delivery systems, to determine the uncertainties (such as lack of energy dependence) associated with these devices.

3.3 Energy

The accuracy of the energy delivered from the accelerator is one component of the penetration uncertainties due to beam delivery (PUBD). Synchrotrons have an inherent phase stability (i.e., high-energy ions receive less acceleration than low-energy ions) and feedback, whereas cyclotrons are susceptible to magnet temperature changes, leading to instability. To account for instability of the cyclotron energy, an energy spectrometer (energy selection system) is typically placed in the beam path to restrict delivery of ions to only the desired energy.

The energy of a synchrotron can be derived from a velocity measurement of the accelerated ion bunches orbiting around the containment ring. This can be accomplished by using multiple beam position monitors placed around the ring to measure the circumference of the orbit and redundant frequency counters to determine the revolution frequency (Moyers et al., 2007). These measurements can be used for simple interlocks on the energy, elaborate feedback mechanisms, or both. At Loma Linda University (LLU), both methods are used. In this scheme, the energy of the beam is checked each acceleration cycle before the bunch of accelerated protons is extracted and sent to the patient. As seen in Figure 2, if the energy is within the deliverable region, the beam is extracted from the accelerator and sent to the patient. At LLU, the interlock value for extraction is set at ±0.1 MeV. The uncertainty of delivered energy could be calculated using Equation 6 if the distribution of energies was uniform across the tolerance region. If the energy is within the correctable region, the extraction is aborted and the accelerator settings changed slightly to provide the correct energy of protons on the subsequent cycle. At LLU this value is set at ±0.3 MeV. If the energy is within the uncorrectable region, the extraction is aborted, the treatment terminated, and the accelerator operator notified. Moyers and Ghebremedhin (2008) measured the maximum variation in spill-to-spill energy from the LLU accelerator in terms of water-equivalent range to be within ±0.03 mm for 250, 155, and 70 MeV energies and at

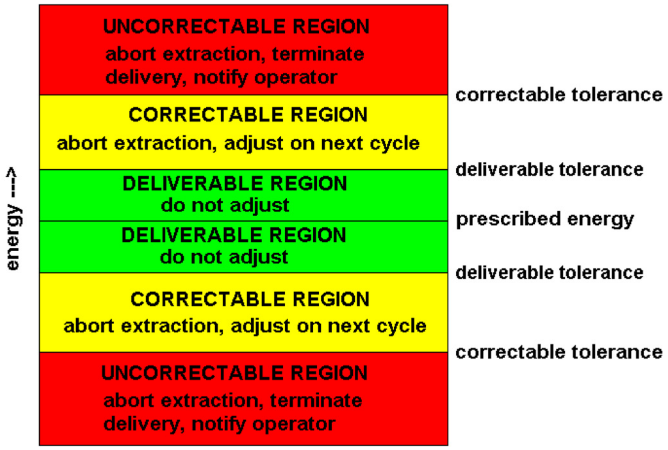

Figure 2. Interlock and feedback scheme for synchrotron energy.

full, three-quarters, one-half, and one-quarter beam fluxes. The average variation of the energy was much smaller. The day-to-day energy variation was also measured during an 11-month period for an energy of 149 MeV. Using a standard daily QA device placed at the treatment position, the 2 SD variation in measured range (including beam passage through a variable thickness double scatterer system) was less than 0.08 mm, with the maximum measured variation in range being within ±0.11 mm, corresponding to a maximum energy variation within ±0.06 MeV, or about half of what would be calculated using the interlock setting and Equation 6. The energy interlock is thus observed not to be used to truncate a uniform distribution of energies, but rather to prevent occasional outlying energies from being transported. Calculations for a Hitachi synchrotron showed that the uncertainty in range for a proton beam should be less than 0.025 mm in water. This value was determined using an assumption that the beam orbit position in the synchrotron is always within ±1 mm (Gillin et al., 2010).

As a backup for the primary method of monitoring the energy, a magnetic field probe may be placed into a bending magnet, where it can be used as a secondary monitoring system to verify that the bending magnet is set to allow only the appropriate energy to the patient. Due to the large energy acceptance of the magnet, which is sometimes set up in an achromatic configuration, the tolerance on this secondary backup method is usually significantly larger than the primary accelerator monitor, possibly allowing a range difference of up to ±4 mm of water (Moyers and Vatnitsky, 2012).

Since cyclotrons do not have an inherent method of monitoring the beam energy, they often rely on the backup method just described above for synchrotrons as their primary method. To reduce the energy uncertainty, a collimation slit may be placed after the bending magnet to prevent transport of ions with unwanted energies. This magnet and collimator configuration, similar to a spectrometer, has often been used with clinical electron accelerators for either an energy interlock mechanism or a feedback mechanism. There are no reports, however, of these mechanisms being used for light ion beam therapy. Instead, the slit is typically used only to limit the energy spread (Schippers et al., 2006; Grevillot et al., 2010) and other methods, such as described in the following two paragraphs, are used for monitoring and interlocking the energy.

Another method of monitoring the energy is to use a multi-layer Faraday cup (MLFC) or multilayer ionization chamber (MLIC). These devices may be placed between the accelerator and the gantry, or they may be placed inside the radiation head distal to all the beam delivery URS devices (patient-specific, range-shifting devices would, of course, not be included). If the device is placed between the accelerator and the gantry, it must be removed from the beam path before each treatment commences, meaning that the range is checked only before the treatment, and range changes that occur during treatment can not be detected. If the MLFC or MLIC is placed inside the radiation head and scatterers are used to spread the beam laterally, the MLFC or MLIC can be located such that it only intercepts unused ions at the lateral periphery of the beam. This configuration allows the beam energy to be monitored continuously during treatment, with the results fed back through the control system to adjust the energy or trip an interlock. The uncertainty in range for an MLFC placed upstream of a gantry may be as small as ±0.2 mm (Hsi et al., 2009), but the uncertainty for an MLFC placed in the radiation head and measuring the periphery of the beam may be between ±1 mm and ±3 mm.

For beams delivered with a modulated scanning mode—a scanning mode wherein a small-diameter light ion beam is scanned across a target to create a field large enough to cover the target such that the intended fluence delivered to the patient is different at different lateral locations (DICOM, 2006; IEC, 2014)—a check of the beam energy may also be performed by using the spot scanning magnet as a spectrometer. In this scheme, for each energy level the position of the first spot may be checked for proper location off-axis, and if it is not within a specified tolerance, the beam delivery can be aborted. The spot position is, however, dependent upon several factors besides the beam energy, so the check is not solely an energy check.

3.4 Scatterers

If an adjustable thickness scatterer is placed downstream of the energy-measuring system, then some method of guaranteeing the correct thickness is required. One example for a double wedge configuration is to have two or more positioning screws for each wedge, with position encoders on both the driving and verification screws (Moyers and Siebers, 1995). As mentioned above, measured data with this configuration showed the overall beam range, including the accelerator component, was always within ±0.11 mm, so the reproducibility of the water-equivalent thickness of the wedges is less than that value. Binary-configured scatterers are somewhat simpler, as the monitors simply have to monitor that the scatterer is in place or not. With both types of scatterers, however, typically the monitor only detects that the scatterer holder is in the correct position; if the scatterer were to become dislodged from the holder, the change in thickness would not be detected. To detect this unlikely but possible event, downstream beam monitors that detect changes in the 2-D fluence distribution must also be implemented (Moyers and Vatnisky, 2012). To maintain the specified uncertainty allowance in planning, periodic inspection and QA measures should be implemented.

Uncertainties in penetration range may depend on proton beam energy in some cases. As mentioned in section 2.2, the amount of range shift in high-Z materials depends on the ion beam's energy. Scatterers are commonly made of high-Z materials, such as lead. It is thus essential to take into account the energy dependence when calibrating the range shift associated with high-Z beamline components; otherwise, additional penetration uncertainty must be added when planning the patient.

3.5 Gases within the Beamline

To reduce the scatter of scanning beams and improve fluence modulation, some radiation heads are evacuated or filled with helium gas. If helium is used, the gas is usually flowed through the beam path at a low rate. This flow rate is controlled via a helium differential pressure switch and a pressure relief valve that creates a safety interlock intended to prevent destruction of the gas window from too much internal helium pressure. In case of an improperly working interlock system or wrong gauge reading, changes in the density of the gas can result in changes of the beam range and width of the scanning spot. The size of the spot at the isocenter would almost double if the helium gas was wholly replaced with air. This change in spot size can be detected by a beam fluence distribution monitor (typically a multi-wire ion chamber) and a comparison with the expected spot size. A disagreement between the sizes would abort the beam delivery. The change in spot size is much more pronounced than the change in beam range. A similar effect would be seen if the radiation head used a vacuum and a small air leak occurred. The uncertainty in beam penetration due to radiation head-filling gases is thus considered small.

3.6 Energy Stacking / Range Modulation

The extent to which the energy stacking / range modulation method can affect the dose coverage of the target, and thus the uncertainty in range modulation width, is considered under the category of beam penetration uncertainties. There are numerous methods to perform energy stacking / range modulation, and each has different uncertainties.

Traditionally, range modulation was most commonly performed using rotating propellers (for scattered beams) or ridge filters (for scattered or scanned beams); for examples see (Moyers, 1999). These discrete devices each provided only one modulation width and were installed either by hand or on a programmable exchanger inside the radiation head. The only way that the delivered modulation width could change for these devices was if damage occurred. Periodic QA procedures and inspection of the devices ensured that they performed the same as when they were commissioned. The uncertainty in range modulation width with these devices is thus near zero.

A related method of range modulation is to combine a rotating propeller with beam gating or flux modulation. In this method, a propeller is used that is manufactured to provide a maximum amount of range modulation. In the gating method, the beam is synchronously gated with the modulator propeller rotation. Specifically, it is gated off before all thickness steps are encountered, thereby reducing the range modulation width compared to the maximum possible. Similarly, the beam may be gated on after some steps have already been encountered. Alternatively, the beam may be gated on while the modulator propeller is at an occluding step (i.e., water-equivalent thickness of step greater than the beam penetration range). With the gating method, the accuracy and precision of the range modulation width depends upon the accuracy and precision of the synchronization of the gating signal with respect to the modulator propeller angle, the latency of the control system in gating the beam current, and the slew rate of the beam current during transitions from beam-on to beam-off, or beam-off to beam-on, or both. Inaccuracy or imprecision can cause the properties of the delivered portals to deviate from those prescribed in the patient's plan. This may also change the delivered dose, as the same number of monitor units (MU) are delivered but in a different pattern. The timing may also be affected by wear of the rotation bearings, which can cause a wobble in its rotation speed or a change in the performance of the timing system. Another possibility of error is if the propeller rotation position is provided by a potentiometer voltage and the output voltage of the potentiometer changes. A non-intentional variance of the beam flux also has the potential to change the range modulation width, but the most likely effect of this event would be to affect the uniformity of the depth dose distribution within the target region. An extension of the gating method is to purposely modulate the beam flux while the propeller is rotating. Generally this method is used with propellers that are placed upstream in the nozzle and are thereby sensitive to different scattering properties at different energies. By providing different flux modulation patterns for different energies, one propeller can be used over a large range of energies and still provide a uniform depth dose distribution across the target region. As with the gating method, a deviation of the beam flux modulation pattern or rotation characteristics of the propeller could lead to nonuniformities in the depth dose distribution. Another issue with upstream propellers when used with the gated or beam flux modulation methods is the effect of variances in the sizes and shapes of the beam spot hitting the propeller. If the spot size and shape changes, this effectively alters the beam flux pattern hitting the propeller, thereby changing the range modulation width. This effect may become apparent if the beam shape entering the gantry is asymmetric and, therefore, the shape of the beam spot hitting the propeller is a function of the gantry angle. Beam delivery systems that use beam flux modulation have shown day-to-day variations in the modulation width from the prescribed value of ±3 mm (Moyers and Vatnitsky, 2012) and ±7 mm (Lu et al., 2007).

Another method of range modulation is to use multiple energies from the accelerator, in other words energy stacking. This method is often used with the uniform scanning beam delivery technique and most modulated scanning beam techniques, but it can also be used with scattered beams (Moyers and Siebers, 1995). The energy uncertainty for each individual energy is the same as described in section 3.3, so if the system delivers the correct MU for each energy, then the uncertainty in the range modulation width should be quite small. If the MU for one or more of the energies were in error, however, then the range modulation width could be in error, particularly if the MU for the lowest energy levels were not correct. The energy stacking method can also be performed by inserting different thicknesses of URS (Farr et al., 2008). In this case, the modulation width uncertainty is governed not only by the energy accuracy and MU delivery, but also by the uncertainty in the URS thickness. The conformity of the modulation width to the target is determined by the available URS thickness intervals.

3.7 Patient-specific Two-dimensional Range Shifters (2DRSs)

3.7.1 Materials

Dose delivered to tissues distal to the target can be reduced by inserting a customized two-dimensional range shifter (2DRS) into the path of the beam upstream of the patient. This patient-specific 2DRS—historically called a bolus and sometimes erroneously a range compensator—can be designed to limit dose to specific critical normal structures distal to the target volume (distal blocking) or to generally limit the integral dose to non-specific tissues distal to the target volume by stopping the entire beam as close to the downstream side of the target as possible, but adding a margin to allow for penetration uncertainties that might reduce target volume coverage. To minimize scattering from the device, the 2DRS is typically constructed of a low-atomic-number material, such as polymethylmethacrylate (PMMA) or a machinable wax. Advantages of wax over PMMA are that it is cheaper to buy, faster to machine, and can be reused by melting and recasting; however, care must be taken when recycling the wax to avoid introducing contaminates or air bubbles into the material, which could lead to variances from the planned range during beam delivery. In addition, because PMMA is harder and more brittle than wax, PMMA requires more time for machining and, if dropped during treatment, may break more easily. An advantage of PMMA over wax is its transparency, which makes detection of heterogeneities within the material easier. In addition, the water equivalence (WEQ) of PMMA is relatively constant from batch to batch. For all materials, since the WEQ may vary from batch to batch and from supplier to supplier, it is important to periodically check the WEQ of blank devices (regularly shaped blocks before being milled into patient-specific shapes). When proper handling and QA procedures are used, 2 k_p variances in the water-equivalent thickness (WET) can be kept below ±0.5%; for a description of k_p usage, see section 2.

3.7.2 Effect of Design Algorithms

The thickness distribution of the 2DRS is generally calculated in multiple iterations. First, the algorithm determines the WET along a ray line from the patient surface to the distal point of the target by means of ray tracing. In a second step, the device is modified by the application of various filters.

The most important of these filters is cavity expansion, often referred to as smearing (Urie et al., 1983). The intent of this expansion is to account for loss of lateral scatter from nearby ray lines with shorter ranges and to account for possible misalignments or motion of patient tissues with respect to the beam. For example, if a patient was to be misaligned by 3 mm and an expansion of 3 mm was applied, then the target volume would still be adequately covered during treatment. The cavity expansion technique works by replacing the thickness at a particular point of the device by the minimum thickness found in the raw thickness distribution within a given area. The technique basically thins out the device, resulting in a larger range to the patient at locally thick regions of the device. Prior to 1990, some dose calculation algorithms used the shape of the initial design of the 2DRS to calculate the dose distributions rather than the shape of the "as built" 2DRS. Generally, this resulted in a calculated dose distribution around heterogeneities that showed a slightly less penetrating beam than delivered. In 1994, dose calculation algorithms started appearing that used the "as built" shape, thereby increasing the accuracy of the calculated dose distribution.

The uncertainty in beam penetration within the patient is dependent upon the algorithms used, so it is important for the user to know and understand the algorithms used by their TPS for both designing 2DRSs and calculating dose distributions associated with 2DRSs.

3.7.3 Effect of Manufacturing Techniques and Parameters

There are many different ways to construct a 2DRS. The most common method uses a milling tool that is almost flat on the bottom with sides that are slightly conical with an incline of typically 3 degrees. A computer numerically controlled (CNC) milling machine plunges the conical tool into the blank material in a direction perpendicular to its front surface. By superposition of 100 to 10,000 plunge positions of different depths, a cavity is generated. This method results in a device with many discrete ledges instead of a smooth surface. Although milling techniques that create smooth surfaces were investigated as early as 1990, users have chosen to stay with the discrete plunge method, perhaps because it is easier to identify problems during QA procedures when the discrete plunge method is used. Although the produced distal edge of the dose distribution may not be as conformal, the uncertainties are better understood.

The milling tool size has a large effect on the final appearance of the 2DRS. At the M. D. Anderson Proton Therapy Center, 3- and 5-mm diameter tools are used. The smaller tool is usually used only for portals with small field sizes and thicknesses; i.e., cavity areas less than 100 cm^2 and maximum device thicknesses less than 120 mm. This restriction is mostly due to manufacturing speed limitations (it takes much more time to mill a large cavity with a 3-mm tool than with a 5-mm tool) and the length of a tool with sufficient strength to prevent wobbling or bending during manufacturing.

Another aspect of manufacturing that affects uncertainties occurs for very thick PMMA devices. If PMMA is used for devices thicker than 60 mm, then the blank device may be made by gluing two or more slabs together. In such cases, the glue melts the PMMA surfaces together, creating a thin, very strong layer; however, this layer may have a different density and may change the assumed WET of the device by up to 1 mm for each bonding layer.

3.7.4 Quality Assurance Techniques

Many techniques can be used to assure that the thickness distribution of a manufactured device matches the prescribed distribution. Although laser scanning is capable of measuring the entire thickness distribution with a sub-millimeter resolution, most facilities measure fewer than 20 points. These measurements may be made with a computerized measuring machine (CMM) or by hand using a micrometer or vernier caliper with a 2 SD uncertainty less than 0.04 mm. Typical agreements between the measured and planned thicknesses are within 0.2 mm when the flat surfaces of individual plunges are measured.

Li et al. (2010) imaged 20 different 2DRS devices using a conventional x-ray CT scanner in high-resolution mode (voxel size of 0.5 mm × 0.5 mm × 0.625 mm) and confirmed agreement between the exported TPS data and measured x-ray CT data. A comparison of treatment plan data with measured x-ray CT data found that, using a 1-mm distance-to-agreement (DTA) criteria, in some cases only 80% of pixels passed, whereas when using a 2-mm DTA criteria the pass rate increased to more than 94%.

Yoon et al. (2008) used x-ray CT data with a 1-mm slice thickness to compare the manufactured thickness distribution of 2DRSs with that produced by the TPS. The x-ray CT data were registered with the reference depth map from the TPS, and a comparison showed that only about 1% of the points were above a 2-mm DTA criterion. Those points exceeding the tolerance were generally found at high-gradient regions. It is worth noting that the TPS used to design these 2DRSs did not model the tapered drill bit (3°) used for milling, thereby making the comparison between the planned and actual thickness distributions appear worse. Not modeling the tapered drill bit shape also affects the accurate estimation of the dose distribution by the TPS (Yoon et al., 2008).

3.7.5 Installation into the Radiation Head

The positioning of a 2DRS into a beam applicator varies from installation to installation and depends upon the tolerances of the mounting fixtures, tolerance of device manufacturing, and gantry angle. Typical lateral mounting tolerances are between 0.25 mm and 0.75 mm. This lateral mounting uncertainty translates into a beam penetration uncertainty due to a different thickness of the device occurring at different off-axis positions. The change in beam penetration at a given off-axis position depends upon the thickness of the slope at that position. A device with a highly sloped distribution will be more susceptible to penetration uncertainties.

3.7.6 Applicator Carriage Extension

Most light ion beams appear to emanate from a virtual source, producing a diverging beam. This means that placement of a given device at different distances between the virtual source and the patient results in different off-axis thickness distributions projected to the patient. Most radiation heads are equipped with a translatable applicator carriage to place the patient-specific beam-shaping devices as close to the patient as possible while allowing variable isocenter-to-skin distances for different patients. Although some TPSs automatically calculate the applicator carriage position based upon an input applicator-to-skin distance, these algorithms are not perfect and, if a table top, patient shoulder, etc. has not been taken into account properly during treatment planning, the distance during the actual treatment may deviate from the planned distance by 50 mm or more. This deviation can result in a significantly altered off-axis thickness distribution, particularly if the thickness gradients are large. In addition to a penetration error, a possible error in dose can result due to the differences in distance from the 2DRS scattering source. To reduce deviations between the prescribed treatment plan and the delivered dose distributions, it is recommended that portal verification plans use the actual planned applicator carriage extensions and that the extension values be documented.

3.8 Registration and Immobilization Devices

Some registration and immobilization devices—such as tabletops or pods made of carbon fiber, aramid fiber (e.g., Kevlar™), or polyvinyl chloride (PVC)—do not lie on the x-ray computed tomography number to relative linear stopping power (RLSTP) conversion function curve (see section 5) for tissue and thus can cause errors in penetration. If the errors are known, the plan may be adjusted. Alternatively, if the errors are difficult to correct, such as having different adjustments for different beam entry directions and positions, then the error can be considered to be one component of the penetration uncertainties due to beam delivery (PUBD). Such errors may contribute up to a millimeter in range uncertainty (Moyers et al., 1992).

Some devices with varying thickness—such as facemasks with holes or non-patient-specific devices not formed to the patient—may not align to the patient identically every fraction, causing errors in penetration and should be included in the determination of the total penetration uncertainties (see section 3.10). A typical facemask is one to two millimeters thick, so this much penetration uncertainty should be added when facemasks with holes are used. The commissioning of such devices should include a measurement of their WETs and comparisons with the WETs calculated by the TPS.

The uncertainty in the WET (range shift) is more difficult to determine, but in some cases may be crudely estimated based on the difference between multiple measured and calculated values. Other devices, such as tabletops and pods, may have unintentional varying thicknesses due to manufacturing tolerances. If one device is used in the x-ray CT scan but a different one is used for treatment (i.e., the device does not follow the patient throughout the planning and delivery process), then the deviations from a uniform thickness needs to be carefully investigated.

Another effect on beam penetration is the drawing of the external contours that the TPS uses to define the region within which to calculate. It is important to use a very low x-ray CT number threshold when drawing or using automatic tools to generate these contours. When using automatic tools, it is also important to check that all objects through which a beam may pass are completely within the x-ray CT image reconstructed field of view (RFOV) and have been properly contoured.

3.9 Size of Energy Increments (Discreteness)

Compared to a beam delivery system that uses variable thickness scatterers, URSs, and 2DRSs, a system that uses energy stacking and modulated scanning without these devices has fewer sources of uncertainty that could lead to a change in penetration. On the other hand, the discreteness of the energy levels compared to a system where a finely milled 2DRS is used can result in a less-optimized plan, particularly one that is less conformal on the distal side of the target. Although the discreteness due to the size of the energy increments is known and is part of the plan, the delivered distribution may not be as optimized as desired, often resulting in larger (or smaller, depending on how the rounding or truncation are performed) margins around targets and organs at risk. This limitation in conformality due to the energy increments should be taken into consideration along with uncertainties when setting margins. By varying the spot and energy weights, it may be possible to conform a given isodose level to the desired shape, but the proximal and distal dose gradients are often decreased as a result of that modulation process.

3.10 Total Penetration Uncertainty Due to Beam Delivery (PUBD)

Each facility, and sometimes different equipment and different techniques at one facility, may have different penetration uncertainties due to beam delivery (PUBDs). As an example, Table 1 summarizes PUBDs for four hypothetical beam delivery methods. The total value can be entered into the TPS for designing margins.

Table I: Example summaries of penetration uncertainty due to beam delivery (PUBD) with four different delivery systems. All values are given in millimeters of water and at the 2 SD level.

Item	Synchrotron, Double Scattered, 2DRS	Synchrotron, Modulated Scanned, No 2DRS	Cyclotron, Double Scattered, 2DRS	Cyclotron, Modulated Scanned, No 2DRS
Absolute range measurement	1.14*	1.14*	1.14*	1.14*
Accelerator energy, range shifter thickness reproducibility	0.1	0.1	2.0[†]	2.0[†]
Scatterer thickness	0.1 (double wedge)	n.a.	0.1 (discrete)	n.a.
TPS depth dose model	0.5	0.5	0.5	0.5
Manufactured 2DRS thickness	0.3	n.a.	0.3	n.a.
2DRS material density	0.4 (wax)	n.a.	0.4 (PMMA)	n.a.
2DRS voids or impurities	0.5 (wax)	n.a.	0.2 (PMMA)	n.a.
Discreteness of distal edge	0.0	1.0	0.0	1.0
Registration and immobilization devices	1.0	1.0	1.0	1.0
TOTAL (quadrature sum)	1.8	1.9	2.6	2.7

* ≡ value taken from Moyers (2010) and Moyers and Vatnitsky (2012).
[†] ≡ value taken from Summers et al. (2012).

3.11 Recommendations

- The user should study the details of the beam delivery system and determine which uncertainties, such as provided in the previous sections, pertain to their system.
- At attempt to quantify the penetration uncertainties stemming from the beam delivery system shall be performed either by assessment of individual components or by system tests. It is suggested here that using the method of assessing individual components will give the user a better understanding of the equipment and more information to design a reliable and efficient quality assurance program.
- Typically all penetration uncertainties stemming from the beam delivery system can be combined into one value, the PUBD, and then used in treatment planning.

4. Uncertainties in Dose Compliance

4.1 Reference Dose per Monitor Unit Calibration

The dose per monitor unit (D/MU) under reference conditions is measured similarly to x-ray and electron beams, and the uncertainty in D/MU is expected to be similar. Moyers et al. (2010, 2014) reported on measurements performed by the Radiological Physics Center at eight proton treatment facilities in the United States. The ratios of facility-to-RPC measured D/MU under reference conditions were found to be within a 2 SD of 2.4%. For the modulated scanned beam delivery technique, some facilities have chosen to define one monitor unit (MU) as equal to the charge produced in the beam monitor detector by one ion traversing the detector and calibrated the beam monitors for a single-energy beam incident on a phantom, or its equivalent in terms of energy deposition, which is the dose-area-product to water at the reference depth (Palmans and Vatnitsky, 2015). In general, the uncertainty due to reference D/MU calibration for proton beams is quite small and similar to x-ray and electron dosimetry. Due to the small number of light ion facilities using ions heavier than protons, such a large comparison similar to that performed by Moyers et al. (2014) has not yet been performed for ions heavier than protons.

4.2 Patient-specific Dose per Monitor Unit Calibration

The uncertainty in the D/MU for patient portals is larger than for reference dosimetry for many reasons. Some of these reasons are given in the following subsections. In the same study cited in the previous section, Moyers et al. (2014) compared clinical portals delivered to a flat phantom and found the ratios of facility-to-RPC measured D/MU to be within a 2 SD of ±3.2%. The uncertainty in patients is expected to be higher than in the flat phantom.

4.2.1 TPS Calculations

The major uncertainty in TPS calculations of the D/MU is poor modeling of scatter from the various beamline devices—such as trimming collimators, apertures, and 2DRSs—but incomplete modeling of the effect of heterogeneities within the patient also contributes. For scattering and uniform scanning systems, the lack of high-accuracy D/MU modeling forces the user to either use look-up tables or parametric fitting for calculating the D/MU or alternatively perform D/MU measurements for each portal (Moyers, 1999; Kooy et al., 2005; Sahoo et al., 2008; Hsi et al. 2009; Engelsman et al., 2009). The accuracy of the parametric fitting and measurements is typically at the 1% to 2% level for regularly shaped portals, but higher uncertainties are associated with "unusual" portals, such as those having small field sizes or highly modulated 2DRSs. For modulated scanning systems, the TPS usually calculates the D/MU directly. The calculated D/MU for regularly shaped box targets typically agrees to the measured D/MU at the 2% to 3% level (Zhu et al., 2015). To achieve this level of accuracy, nuclear interactions must be accounted for in the calculations (Pedroni et al., 2005). In highly modulated plans with large dose gradients, confirming the D/MU for each beamlet of a given energy level is a measurement challenge, so planar dosimetry is typically performed, and a gamma analysis using both dose agreement and distance-to-agreement metrics is employed for determining the accuracy (Low et al., 1998).

4.2.2 Phantom Measurements

The TPS has knowledge of the anatomical geometry of the patient and the geometry of the beam, and thus should be the best estimator of the D/MU. Under extreme conditions, the TPS model may not be sufficient, and phantom measurements must be made. Such cases might involve small field sizes, large gaps between the beam-shaping devices and the patient, severely oblique or tangential incidence, or transmission through devices that do not lie on the standard tissue x-ray CT-number-to-RLSTP function curve. In these cases, selection of the appropriate phantom (anatomically shaped or rectangular parallelpiped, plastic or water, etc.) and radiation detector (e.g., diode or film) are important.

A second reason to do phantom measurements is that some TPSs do not provide the D/MU, so either a phantom measurement or independent calculation method must be performed. Typically these are done using a flat phantom that does not represent what happens in the patient. In these cases, the plan should be recalculated on a simulated patient with the same characteristics as the flat phantom so that a fair comparison can be made. This type of measurement will help verify that the plan was delivered appropriately, but it may not provide the D/MU that would be achieved in the patient.

When phantom measurements are made, several uncertainties must be considered. One is that the phantom material may not match the plan in terms of RLSTP, relative linear scattering power (RLSCP), or nuclear interactions. Another is the response of the detector in the local radiation environment (secondary particle spectrum, instantaneous dose rate, detector size, etc.). The uncertainties in the measurements should thus be investigated and taken into account when evaluating agreement between the plan and phantom measurements.

4.2.3 Independent Calculations

The D/MU from the TPS or phantom measurements must be checked with an independent method. For delivery techniques using scattered or uniform scanning beams, this method usually takes the form of a simple model calculation done by hand or a small computer algorithm. This simple model typically does not take into account cross-talk between various parameters and, therefore, may not be as accurate as the TPS calculations or phantom measurements. Nevertheless, there may be situations that are beyond the limits where the other methods are accurate, and the manual calculations may be the primary determinate of the D/MU. The uncertainty in these calculations will be substantially greater than normally expected and should be explained to the physician of record. The independent method for the modulated scanning delivery technique can be based on assessing the MU values and position accuracy as recorded by the daily treatment records (logs) of the treatment control system. Performing test irradiations to obtain these records can also verify the feasibility of using the prescribed spot positions and MU values to treat the patients (Li et al., 2013). The treatment log file for a modulated scanning delivery system should be precise enough to serve as a quality assurance tool to monitor variations in spot positions and MU values and determine the delivered dose uncertainty from the treatment delivery system (Zhu et., 2015).

4.3 Scattered Beam Delivery

4.3.1 Beam and Scatterer Alignment

The goal of scattering beam production systems is to produce a uniform (flat) lateral dose profile. Among other things, achieving this goal requires that the beam and scattering elements be accurately aligned. Figure 3 shows a radiation head that houses two scatterers: one that is proximal and referred

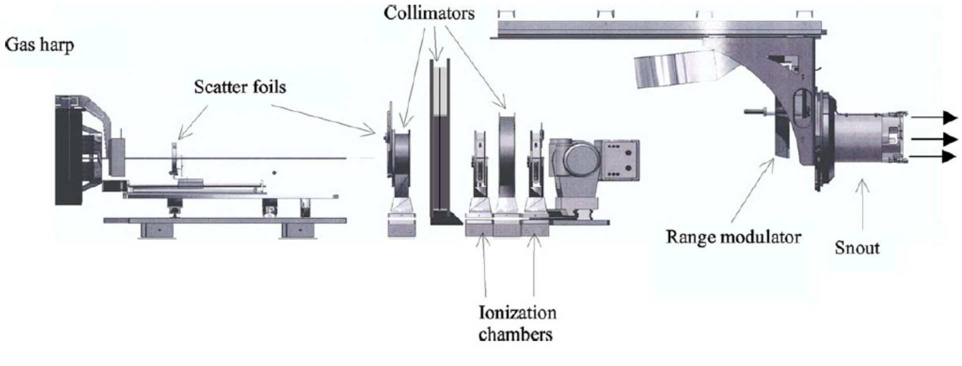

Figure 3. An example radiation head for a simple double-scattered and -collimated system. In addition to the scatterers, various beam monitors and collimators are included. The gas harp is commonly known as a multi-wire ionization chamber (MWIC). The item that holds an aperture and 2DRS close to the patient and that is labeled in the figure as a "snout" is referred to in both DICOM and IEC nomenclature as a "beam applicator" (DICOM, 2006; IEC, 2014). Figure reproduced from Mesolores et al. (2006).

to as the 1st scatterer and one that is distal and referred to as the 2nd scatterer. The function of the 1st scatterer is to laterally broaden the beam into an approximately Gaussian profile which then impinges onto a 2nd scatterer, where the beam is further broadened but yielding a flatter profile. Given a "well-functioning" delivery system, there are the three main sources for error: (1) a broken or cracked scatterer, (2) misalignment along the beam direction, and (3) misalignment perpendicular to the beam direction.

Verifying the integrity of the scatterers must be part of a QA program (Arjomandy et al., 2009). In the event of a damaged scatterer, it must be replaced and verified to produce the same beam properties. Change of beam penetration or dose due to use of a damaged scatterer is usually not included in uncertainty estimates or margins.

The main source of error due to misalignment along the beam direction is the interaction between the lateral dose profile created by the 1st scatterer and the shape of the 2nd scatterer. The 2nd scatterer has a variable thickness with off-axis distance to provide higher scattering in the center of the field produced by the 1st scatterer (the lateral fluence profile having a Gaussian shape) and less scattering at the periphery of the field (in the tail regions of the Gaussian fluence profile). The appropriate amount of scatter mix is optimized by the drift distance between the two scatterers or, in the case of a carousel system, the selection of correct scatterer combinations ("options"). Should there be a mismatch, "overscattering" can occur, resulting in a underdose in the center of the field, or "underscattering" can occur, resulting in an overdose in the center of the field and a quasi-Gaussian lateral dose profile. Although testing for this error source is part of the acceptance tests, even a well-designed system will retain portions of uncertainty due to the under- and over-scattered behavior from the boundary performance at the ends of a commissioned option, either 1st scatterer location or carousel element, of the systems. The uncertainty of an acceptably performing scattering system is the clinical tolerance, usually a flatness within ±3%.

Although the field edge is defined by distal collimation in a scattering system, it can also be affected by misalignment of the scatterers to the beam, to the other scatterers, and to the collimators. Lateral misalignment of the 2nd scatterer, sensitive at the mm level, can result in a skewed beam opposite to the direction of misalignment. This can also be observed to a lesser degree in single scattering systems. As with longitudinal misalignment, the uncertainty magnitude of a properly performing system is within ±3% skewness and symmetry. Arguably more important is a change in the lateral penumbra width, which can dramatically change the dose delivered at the edge of a field. Typically, only 1 mm of uncertainty in the penumbra width is included in the planning margins, but the penumbra can change much more than this if there is misalignment, therefore emphasizing the need to include frequent measurement of the penumbra in a QA program.

4.3.2 Monitoring System Feedback

In addition to the routine QA program that should verify the field flatness, skewness, and symmetry, these dose distribution characteristics must be monitored and interlocked by the beam delivery system. Some delivery systems deliver beam in a two-phase approach. The first phase is a beam-tuning phase just prior to beam delivery where the beam can be magnetically steered onto the correct location of the 1st scatterer. The beam properties are then verified to be within the configured tolerances. Subsequently the beam is delivered and also monitored during the delivery. Monitoring of a scattering system during beam delivery with interlock capability is usually done at the millisecond level, with the goal of no more than a certain portion of a portal's dose allowed to be delivered outside of the tolerance. As an example, the following specification is taken from an internal report by Klein (2003): "Should beam monitoring devices indicate an out of tolerance condition, beam delivery must be stopped before an additional 1% of the total dose has been delivered." Delivery uncertainties within the range of the monitor feedback system should be included into the treatment planning process, but errors in beam delivery that result in interlocks are typically not included.

4.4 Uniform Scanning and Energy Stacking Delivery

4.4.1 Spot Position Entering the Radiation Head

As opposed to the critical alignment of the radiation beam required with modulated scanning systems where distal collimation is often not used, a uniform scanning system retains the distal collimator of a scattering system and, therefore, relies more on the physical alignment of the components of the radiation head. In addition, because uniform scanning systems do not have a contoured second scatterer requiring critical alignment, the sensitivity of absolute beam alignment can be further relaxed. Experience indicates that misalignment of a uniform scanning system at the centimeter level can produce clinically acceptable dose profiles. Another reason that the alignment can be relaxed is the large over-scanning of the beam onto the aperture commonly used with uniform scanning systems. Should the amount of over-scan be reduced, the beam alignment would become more critical (Anferov, 2009).

4.4.2 Spot Spacing Versus Spot Size

Probably the most significant parameter in a uniform scanning system affecting lateral dose profile uniformity is the relationship between the spot size and the scan line density, also known as spacing. Due to their design, uniform scanning systems have a fixed scanning pattern, a fixed scan speed, and a constant beam flux. The pattern is usually governed by the maximum current oscillations that the scanning magnet power supplies can deliver, typically 3–6 Hz in one direction and 12–30 Hz in the perpendicular direction. This leaves scan line density as the controllable parameter for field uniformity. There are several uniform scanning systems in current use. Example systems include the one developed by the Indiana University Cyclotron Facility (IU-US) for the Midwest Proton Radiotherapy Institute (name later changed to Indiana University Health Proton Therapy Center, but facility closed in 2015) (Farr et al., 2008) and the IBA system (IBA-US) included as a mode of their "Universal Nozzle." Significantly, the IU-US does not control the spot size of the system, whereas the IBA system employs a scattering element to do so (Nichiporov et al., 2012). The IU-US system is, therefore, more susceptible to the relationship between scan line density and variations in spot size, the spot size varying with energy and depth in the media. This is mitigated to some extent because higher-energy beams with associated smaller spot sizes also penetrate deeper into the media, which gives a countering effect as the spot spreads due to multiple Coulomb scattering (MCS). Even so, some optimization is usually needed, resulting in noticeable ripple in the lateral dose profiles at shallow depths and roundedness toward the distal end of the delivery volume. Another type of uniform scanning system is about to enter service as a delivery mode of the PSI Gantry 2 modulated scanning system (Zenklusen et al., 2011). Acceptable uncertainty in the field uniformity is the same as for scattering systems, ±3%.

4.4.3 Scan Path Reproducibility

Differences of accuracy and precision can be observed between scattering and uniform scanning systems. A scattering system is capable of delivering more uniform lateral dose profiles than a uniform scanning system, but the delivery-to-delivery reproducibility can be worse due to the sensitivity of the beam alignment with the scatterers. Conversely, uniform scanning systems with a constant scan pattern (as opposed to a non-repeating Lissajous pattern) can exhibit some transverse ripple, but are very reproducible. Anecdotally, the scan path from a constant uniform scanning system with a repeatable scan pattern is reproducible enough that measurements with a small-volume ionization chamber can vary up to a few per cent, depending on position with respect to the scan lines. At a given position and with an unlimited number of field deliveries, the reproducibility can be, however, within the precision of the ion chamber, which is typically about 0.5%.

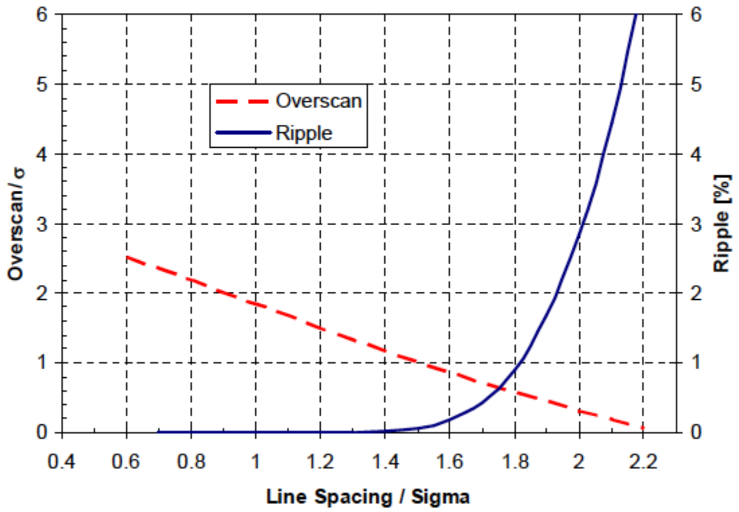

Figure 4. Relationship between scan ripple, scan line spacing, and spot size in uniform scanning. Reprinted from Anferov (2009) with permission from *Medical Physics*.

4.4.4 Spot Size Reproducibility

With uniform scanning systems, a slight increase in spot size is usually tolerated by the system without impact on the clinical field quality. In other words, the uncertainty in delivered dose is smaller than the uncertainty in spot size. Figure 4 indicates the relationship between dose uniformity (ripple) and over-scan value normalized to the sigma of the spot size (Anferov, 2009). (Note that the over-scan distance in this example is defined as twice the scan amplitude minus the field size at the 95% dose level divided by the spot sigma.) An increase in the spot size would effectively increase the normalized over-scan amount (dashed curve), thereby reducing ripple (solid curve). Reductions in spot size are another matter. This is because any significant reduction in spot size could potentially lead to significant field nonuniformity due to the required optimization between spot size and scan line density. Functionally, this is mitigated by the fact that a design goal of any scanning system is to usually achieve the smallest possible spot size (IU-US) or control it with a scatterer (IBA-US). Due to the optimization of the magnetic transport optics, the spot size can usually only be made larger. It is, therefore, important to mitigate the risk by monitoring and interlocking the spot size before and during beam delivery. Setting the appropriate interlock tolerance is extremely important, because if the interlocks are set too tight, then the beam cannot be delivered, but if the interlocks are set too loose, then the increased uncertainty of the true spot size leads to an increase in the uncertainty of the delivered dose. For interlock testing purposes, a special mini-aperture can be placed into the IU-US system or the scatterer removed with the IBA-US system in service mode to demonstrate the response of the beam spot size monitor/interlock.

4.4.5 Beam Flux Stability

Most uniform scanning systems operate at fixed X and Y scanning speeds and, therefore, rely on an appropriate and stable flux to deliver uniform fields. If the flux is lower than planned, the scan pattern frame will be repainted more times than planned, which should only increase the lateral dose profile uniformity. This effect will be seen down to the practical lower limit of clinical use, usually 0.5 Gy/min. On the other hand, a higher-than-nominal flux (one that could deliver greater than 2 Gy/min) can present a problem because the number of scan pattern frames will be reduced, possibly resulting in nonuniformity. Practically this can be tested to establish the acceptable fluxes for clinical use. Flux control is deeply integrated into the delivery safety system. In at least one commercial uniform scanning system, the effect of uncertainty in flux stability is partially mitigated by mandatory repainting of the highest energy level. Unacceptable variations in the flux should be detected within 1 msec, allowing the system to interrupt within a single scan pattern frame. The uncertainty of beam flux instability is built into the overall dose compliance uncertainty.

4.4.6 Uncertainty of Energy Level Spacing

Similar to the situation with scattering, beams of multiple energies must be combined to produce a depth dose distribution that is flat over the intended target within the clinical dose tolerance. For accelerators and energy selection systems that deliver a beam with an energy spread that is a function of energy, a weighting scheme designed for one range of energies can deliver a tilted dose distribution across the target when used at other energy ranges. If an energy-stacking method is used with uniform scanning, then the tilt in the dose distribution can be reduced either by re-weighting (IU-US) (Farr et al., 2008) or by beam current modulation (IBA-US) (Lu and Kooy, 2006). These distributions may only be achieved, however, by having an accurate relative spacing between energy levels, as described in section 3.3. If the interval between energy levels during treatment does not match that during commissioning, then a ripple in the depth dose distribution may be generated that does not match the treatment plan. In addition to adequate distal and proximal coverage of the target, it is thus seen that the dose within the target is uncertain due to the uncertainty in energy level spacing. Typically, the system is designed to limit this dose uncertainty to within ±3%.

4.4.7 Low MU Per Energy Level

The minimum deliverable number of monitor units and the dynamic range of the dose monitoring system are practically limited by the number of portals and field size within a treatment plan given a specified fraction dose. For example, if the number of repaintings for an energy level is less than 30, the error due to partial delivery of that last painting will be 3.3% of the dose in that level. Low-dose portals may thus have larger uncertainty than high-dose portals, and the planner should consider this issue when contemplating the use of these portals.

4.4.8 Motion

Uniform scanning systems, sometimes termed "simulated scattering," attempt to mimic the dose distributions that result from a scattering system, i.e., uniform lateral dose profiles. One advantage of a uniform scanning system over a scattering system is that, for large field sizes, a deeper range can be achieved for the same maximum energy. Theoretically, a uniform scanning system also has the possibility of providing a slightly smaller lateral penumbra, but in practice the difference has not been clinically significant. A potential disadvantage of uniform scanning is the additional sensitivity to target motion because of the dynamic lateral scanning and energy stacking depth. This sensitivity may be due to their lateral and longitudinal time structures in comparison to tissue motion, the so-called interplay effect (Zhao et al., 2008). Initial reports indicate that the amount of uncertainty with moving targets may be clinically acceptable when low dose rates are used (Su et al., 2010).

4.5 Modulated Scanning Delivery

4.5.1 Beam Flux Stability

Provided that beam flux remains within the beam delivery system's tolerances, no observed effect on dose delivery would be expected from a deviation of beam flux. At exceedingly high fluxes, excessive recombination may occur in the dose monitor system, while at very low fluxes, the beam monitors and feedback loops (Furukawa, 2012) will struggle to maintain beam alignment. The maximum and minimum operating values should be obtained from the manufacturer and confirmed as part of the acceptance testing process.

4.5.2 Spot Size and Shape Reproducibility

It is important that the beam spot size and shape be reproducible in comparison to the values used for dose modeling in the TPS. Although the spot size is often described in terms of multiples of sigma (σ) using a single Gaussian distribution, the field edge penumbra is sometimes used as an indication of scanned field quality. Spot shapes are usually circular or elliptical, but other shapes have also been observed. In one study evaluating spot shape, the metric "spot flattening" (X–Y)/X in percent was used with X representing the horizontal and Y the vertical directions. Spot flattening in air at the isocenter was evaluated across energies from 70 to 230 MeV, multiple gantry angles, and two types of scanning radiation heads. The composite result was an average beamlet flatness of 2% with a maximum of 5% (Farr et al., 2013). In a different study, unusual comet-like shapes were observed at very low intensities for a type of multi-modality radiation head with scanning modes adapted from scattering technology (Lin et al., 2013). The authors reported that modeling of the beamlet tails is not included in the TPS and that uncertainties of less than 2% in field dose were possible, but as high as 5% could occur. Uncertainties in the spot size and shape exiting the radiation head dominate for beams used to treat shallow tumors, while uncertainties in modeling tissue scattering dominate for beams used to treat deep tumors

4.5.3 Spot Overlap

Theoretically a spot spacing factor of approximately 1.5 σ results in an acceptably uniform dose (Baumer and Farr, 2011) but practically 0.65–1.2 σ is used at most facilities clinically (Zhu et al., 2011). Wider spot spacing is not recommended, but reduced spot spacing has been considered to provide deliveries that are more tolerant of target motion. This is at the expense of decreased MU per spot, which is sometimes a limiting factor itself in the planning optimization process (see section 4.5.6). An alternative method to changing the spot spacing for motion mitigation is to perform spot rescanning at the nominal spacing. Increased spot overlap (reduced spacing) is also used when the spot shapes are asymmetric to reduce the dose compliance uncertainty.

4.5.4 Accuracy of Spot Placement

The magnitude of potential dose errors from misplaced spot aiming positions depends on the same factors as the spot shape errors (see section 4.5.2). Several studies have been reported for a variety of spot sizes. A displacement of four consecutive spots with a σ in air of 10 mm—representative of a linear displacement along the scan direction of a partial row of spots—can reportedly give a 5% local overdose for random displacements of the four spots by 1 mm and up to a 3% reduction in target coverage from random displacements of the four spots by 1.5 mm (Peterson et al., 2009). Dose error effects from similar displacements of smaller spots can be expected to be worse. One study reported up to a 20% local dose deviation from a 1.5-mm displacement of a 3-mm σ spot (Zenklusen et al., 2011). These studies support system design decisions to strictly control spot aiming positions through acceptance testing, QA, and treatment interlocks. Actual delivered spot placements should be recorded in the delivery system log files and be available for comparison with the treatment plans. Li et al. (2013) showed good correlations between the delivered positions and planned positions, providing confidence in the system interlocks.

4.5.5 Energy Accuracy/Reproducibility

Uncertainties in level-to-level energy accuracy/reproducibility are exacerbated when energy stacking is combined with modulated scanning. This combination can result in dose uncertainties in the middle of the target region in addition to the distal and proximal edges. One study considered the combined effects of spot dislocation and energy errors. The position error and energy error simulated were 0.2 cm and 0.2 MeV, respectively (Coutrakon et al., 2010). Results of the study indicated that in the proximal half of the target, spot position errors dominated, whereas in the distal half of the target, both energy and spot position errors contributed about equally. In the distal region, the energy error dominated. The dose compliance uncertainty should be carefully analyzed over the range of allowed combinations of parameters for each different type of beam delivery system.

4.5.6 Low MU Per Spot

Based on the dynamic range of the control system, all scanning systems have minimum and maximum deliverable MU per spot limitations. The maximum MU limitation can be circumvented by "splitting" spots of large MU into multiple spots of smaller MU. The minimum deliverable spot MU can, however, affect the delivered dose distribution quality (Zhu et al., 2010). This has implications on how many total spots are planned, their spacing, and repainting. Spot MU rounding errors that occur post planning can result in doses within the proximal region of the range-modulated volume to be different from that planned. The importance of this phenomenon increases when repainting for motion mitigation is used because the integrated flux for each aiming point is decreased. If the beam is turned off and back on between each aiming location, there are additional uncertainties due to estimates in the calculations of the spot time prediction algorithms.

4.5.7 Dose Halo

"Dose halo" is the descriptive term for low levels of dose contributed from a single beamlet at significant distance lateral to the beamlet's axis. Although the amount of halo dose contribution is small, it can contribute a considerable fraction of the total dose in situations where either a small number of beamlets contribute dose to a small volume or many beamlets contribute to a large volume. If halo doses are not properly included into the dose calculation model under these conditions, additional errors can be introduced into the dose calculation. Sometimes the dose calculation model uses a superposition of two or more Gaussians (Schwaab et al., 2011; Sawakuchi et al., 2010), one for the primary beamlet dose and the other a much lower-weighted but broader distribution to better model the halo dose component. Several groups have looked at this issue and reported dose calculation errors of 5% to 10% when the dose halo components were not included, especially for small fields (Pedroni et al., 2005; Gottschalk, 2015). Using a double Gaussian dose calculation algorithm usually results in errors of less than 3% for typical clinical cases (Zhu et al., 2013).

4.6 Relative Biological Effectiveness

For the intents and purposes of this report, it is recommended that medical physicists implement a formal system of dosimetry that relates the prescribed dose (either using the quantity absorbed dose or an RBE-weighted absorbed dose) and the delivered dose (e.g., in monitor units). Consistency must be achieved in treatment planning (e.g., dose prescription), beam characterization (e.g., measurements of beam dose per monitor unit), treatment delivery (e.g., dose metering and recording), and quality assurance (e.g., chart reviews). Typically, these activities involve multiple software and hardware systems, as well as a team of individuals from varying disciplines. Due to the potential for errors or omissions, it is important that the system of dosimetry is transparent and clear.

More broadly, the RBE is a function of multiple variables, including tissue type, endpoint, fractionation schedule, and linear energy transfer effects. The topic of RBE is beyond the scope of this report. In principle, a comprehensive analysis of the uncertainties associated with these variables is critical to the overall assessment of uncertainties in patient dosimetry. In practice, this is not possible because of incomplete information on RBE in humans (e.g., from radiobiological, epidemiological, and clinical studies). Interestingly, this is in stark contrast to the situation for therapies with ions heavier than hydrogen, where an abundance of evidence forms a compelling case to take selected RBE values and their associated uncertainties into account in patient dosimetry. Indeed, after more than half a century of clinical proton beam therapy, there is still a lack of knowledge of RBE values in humans for any endpoint or tissue, not to mention their uncertainties. Exacerbating this situation, the knowledge of how RBE values vary between individuals, populations, and other host factors is still lacking. For these reasons, an uncertainty analysis can not, at the present, take into account RBE in a comprehensive manner. More information about RBE issues with ion beams may be found in the International Atomic Energy Agency technical report #461 (2008). A separate AAPM task group is currently preparing a report that aims to address RBE issues with proton beams.

4.7 Recommendations

- Setting of interlock thresholds is part of the commissioning process, but the threshold values directly impact the uncertainties. The magnitude of the uncertainties due to the interlock settings must be considered in the treatment planning process.
- Despite extensive commissioning tests, when new equipment is first put into operation at a facility, reliable estimates of the dose compliance uncertainties may not be available. This is particularly the case with patient-specific D/MU. In such cases, the user may use historical data from similar equipment. Once the equipment is used for some period of time, facility-specific data should be used.

5. X-ray Computed Tomography Numbers

5.1 Introduction

Arguably, the largest physical uncertainty that affects treatments with light ion beams is the accuracy of x-ray computed tomography numbers. To compute the dose distribution from therapeutic light ion beams in the patient geometry defined by x-ray CT images, most dose calculation algorithms currently used in the clinic require ratios of the stopping power and scattering power of the medium to that of water. These ratios—the relative linear stopping power (RLSTP) and relative linear scattering power (RLSCP)—are both related to the x-ray CT number. Conversion of the x-ray CT numbers to light ion RLSTPs presents a major challenge in light ion therapy because of the related computational errors in the finite light ion penetration and, correspondingly, in the dose distributions in a patient.

The total uncertainty of the computed light ion penetration is affected by both the uncertainties in x-ray CT numbers and the uncertainties of converting x-ray CT numbers to light ion RLSTPs. To quantitatively evaluate the relationship between the uncertainties related to x-ray CT numbers and the light ion penetration uncertainties, the RLSTP in each x-ray CT voxel can be defined as:

$$RLSTP = CF \cdot XCTN, \qquad \text{(Eq. 7)}$$

where CF is the x-ray CT-number-to-RLSTP conversion function and XCTN is the x-ray computed tomography number. Typically, this conversion function consists of several discrete lines that pass through the origin and the point representing water as seen in Figure 18 (section 7.1). Using Equation 3, we obtain the combined uncertainty u_c(RLSTP) of the RLSTP:

$$u_c^2(RLSTP) = XCTN^2 \cdot u^2(CF) + CF^2 \cdot u^2(XCTN), \qquad \text{(Eq. 8)}$$

where u(CF) and u(XCTN) are the uncertainties of the conversion function CF and the x-ray CT number, respectively. The uncertainties u(CF) of the conversion function CF will be discussed in section 7, while the uncertainties u(XCTN) of x-ray CT number are discussed in this chapter. The uncertainty in x-ray CT number, u(XCTN) can, in turn, be separated into the random uncertainty due to x-ray CT image noise and the systematic uncertainty due to image artifacts, as seen in Equation 9:

$$u^2(XCTN) = u^2(Random) + u^2(System) \tag{Eq. 9}$$

The systematic and random errors in the x-ray CT numbers introduce corresponding systematic and random uncertainties in the RLSTPs and the computed range (CR). As seen in Equation 10, a relationship between the error of RLSTP and the computed range error can be obtained using the fundamental range-stopping power relationship:

$$CR \pm \Delta_{CR} = \int_{E_0}^{0} \frac{dE}{LSTPW \times (RLSTP \pm \Delta_{RLSTP})} \tag{Eq. 10}$$

where E_0 is the initial proton energy and LSTPW is the linear stopping power in water.

The goal of this section is to describe the uncertainty u(XCTN), its components, and their influence on light ion penetration. The x-ray CT number uncertainty management strategies to reduce the associated errors of the light ion penetration will also be discussed. Many of the factors associated with x-ray CT number accuracy and artifacts are discussed in considerable detail in textbooks (Hsieh, 2003; Bushberg et al., 2001), reports (AAPM, 1993; AAPM, 2003), and general articles (Groell, 2000; Barrett and Keat, 2004; Yamamoto et al., 2008; Moyers et al., 2010; Yang et al., 2012). This section provides a summary of factors associated with x-ray CT number accuracy and expands on many of the factors that are not commonly discussed in detail in the literature.

5.2 Random Uncertainties in Pixel Value (Noise)

5.2.1 Properties of X-ray CT Image Noise

Noise in x-ray CT images is manifested as random fluctuations in x-ray CT numbers due to quantum noise in the detected x-rays and other noise sources, such as electronic noise. In most clinical circumstances, image noise is dominated by quantum noise; however, an observed increase in image noise can be due to detector problems causing a larger electronic noise component. Noise in an x-ray CT image is a stochastic phenomenon, which is usually assumed to have a Gaussian distribution. The standard deviation of the voxel x-ray CT numbers within a region of interest (ROI) can be predicted analytically within a homogeneous medium, such as an air or water cylinder (Kijewski and Judy, 1987; Bushberg et al., 2001; Siewerdsen et al., 2002). In highly heterogeneous media (for example, a patient), noise may be increased compared to that in a homogeneous phantom, and its value is difficult to compute analytically; however, one can expect the quantum noise to follow the basic analytical dependencies, such as inverse proportionality to the square root of dose and thickness of the acquired slice. Using the notation of AAPM Report 39 (1993), the standard deviation of the quantum noise is defined up to a constant of proportionality for a given photon energy spectrum by Equation 11:

$$\sigma_{noise} \sim \frac{1}{\sqrt{w^3 hQ}} \tag{Eq. 11}$$

where w is the spatial resolution, h is the imaged slice width, and Q is the x-ray tube mAs. According to AAPM Report 39 (AAPM, 1993), “Any scan parameter which results in improved spatial resolution causes an increase in noise. Conversely, factors which degrade resolution improve noise.” An

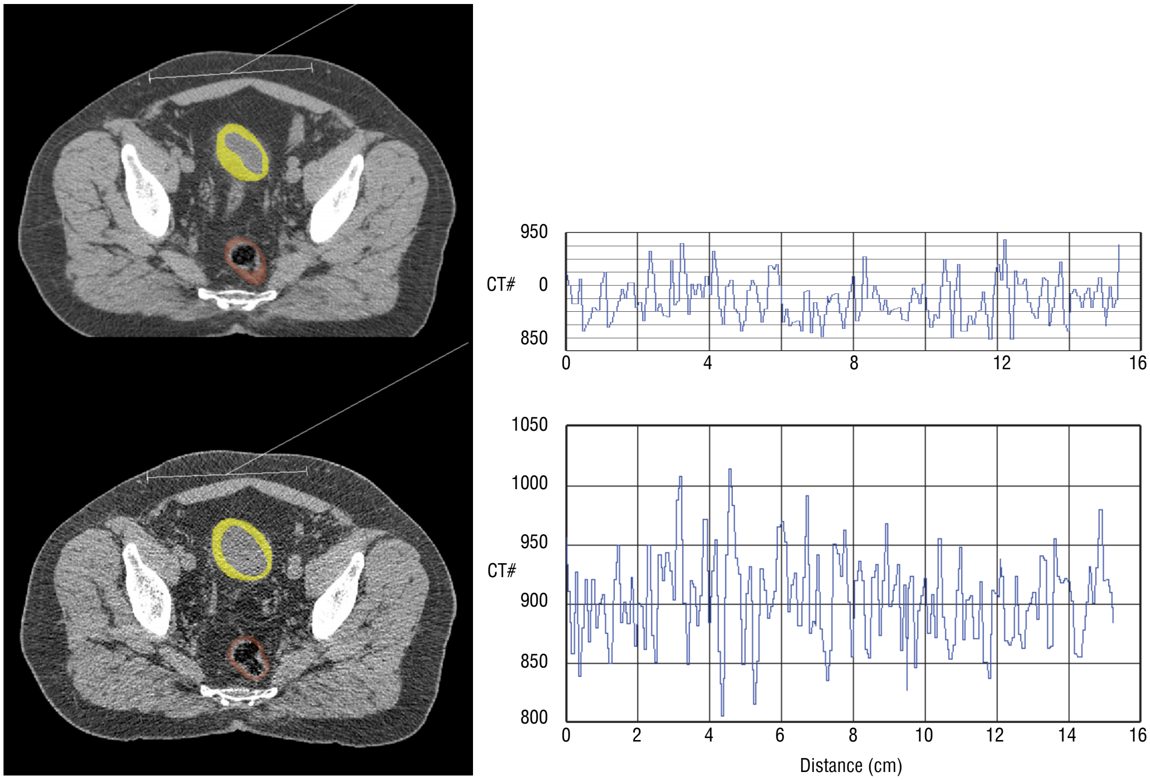

Figure 5. Numerical noise in soft tissue: a) x-ray CT image with 3-mm slice thickness, b) x-ray CT image with 1-mm slice thickness.

example of noise in a patient is seen in Figure 5. One can see that the x-ray CT noise increased approximately by the factor of $\sqrt{3} \approx 1.7$ by changing the x-ray CT slice width from 3 mm to 1 mm.

Being Gaussian in its basic characteristics, the x-ray CT image noise has a high degree of spatial correlation, which is evident in the noise-power spectrum and the “texture” of the noise. When the projection’s raw measurements (sinogram) have additive white noise, the noise in the reconstructed x-ray CT image is not white. The x-ray CT image has much more noise at higher frequencies than at lower frequencies, which is a direct result of oversampling of the lower frequencies during the reconstruction procedure (Schulthess, 1998). For a slice-based fan-beam x-ray CT scanner, the noise power-spectrum properties apply only to the axial (x, y) domain, and the noise is uncorrelated in the longitudinal slice (z) domain.

In addition to quantum noise, x-ray CT images can be contaminated by electronic noise. Electronic noise adds to the quantum noise in the detected signal as the square root of the sum of the squares. Since electronic noise is generally relatively constant and is a small value compared to the detected signal plus quantum variations, it will not have a significant effect, except when the detected x-ray signal is weak due to a large patient or low technique settings. Electronic noise is most evident as lateral streaks in scans through the shoulders or when the patient’s arms are positioned at their sides. Many, if not all, scanner vendors apply mitigation algorithms (often in the form of low-pass filters) that become active for projections contaminated by electronic noise. This reduces resolution, but can substantially improve an otherwise unacceptable image.

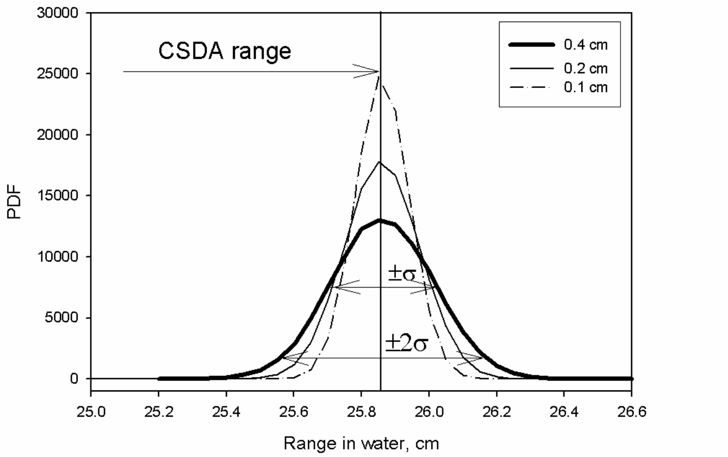

Figure 6. The probability density function (PDF) of the computed proton range in the presence of x-ray CT image noise as a function of the computational grid for a 200 MeV proton beam in water-equivalent media. Reprinted from Chvetsov and Paige (2011) with permission from *Physics in Medicine and Biology.*

5.2.2 Influence of X-ray CT Image Noise on Computation of Light Ion Beam Range

The light ion beam range computed in the geometry defined by x-ray CT images can be considered a random parameter because of the stochastic component of the x-ray CT numbers; therefore, the stochastic beam range uncertainty should be included in the distal margin when designing portals. The deviation of a random computed light ion beam range from the true range should be characterized by the probability density function (PDF). The standard deviation σ of the light ion beam range can be used as a measure of the range uncertainty.

The uncertainties in the proton beam range computed in an x-ray CT image-based geometry in the presence of x-ray CT noise have been evaluated based on Equation 10, continuous slowing down approximation (CSDA) for the range simulation, and uncorrelated white noise for the x-ray CT image noise (Chvetsov and Paige, 2011). The uncorrelated white noise approximation was valid only in the z-direction on 3D x-ray CT images; however, it was also accepted in all other directions to obtain rotationally symmetric margins in treatment planning. The approximation of the white uniform power spectrum is acceptable as a worst-case scenario because (1) higher noise frequencies produce smaller proton range errors due to stronger x-ray CT error cancellation effect and (2) most of the x-ray CT noise power spectrum is in the higher frequencies. A random-number generator was used to simulate a white Gaussian noise in the x-ray CT numbers along the proton path with the standard deviations of the noise simulated between a low value of 2.5% to a hypothetically high value of 10%. To simulate the statistical straggling of the computed proton range, this procedure was iteratively repeated to obtain a convergence of the proton range probability function (PDF), which approached a normal distribution (Gaussian) according to the central limit theorem (Figure 6).

In general, the performed numerical experiments demonstrated that the relative standard deviation (σ) of the random proton range is about five times smaller than the relative standard deviation of x-ray CT image noise because of the error cancellation process in different voxels; however, the 95% confidence interval width of the range PDF, which is defined as 4σ, can be significant under typical simulation conditions. If the full range variation would be defined as 4σ, it can be of the same order of 1% to 2% as the uncertainties arising from the x-ray CT-number-to-RLSTP conversion process (see section 7). The computational results also showed a linear relationship between the standard deviation of

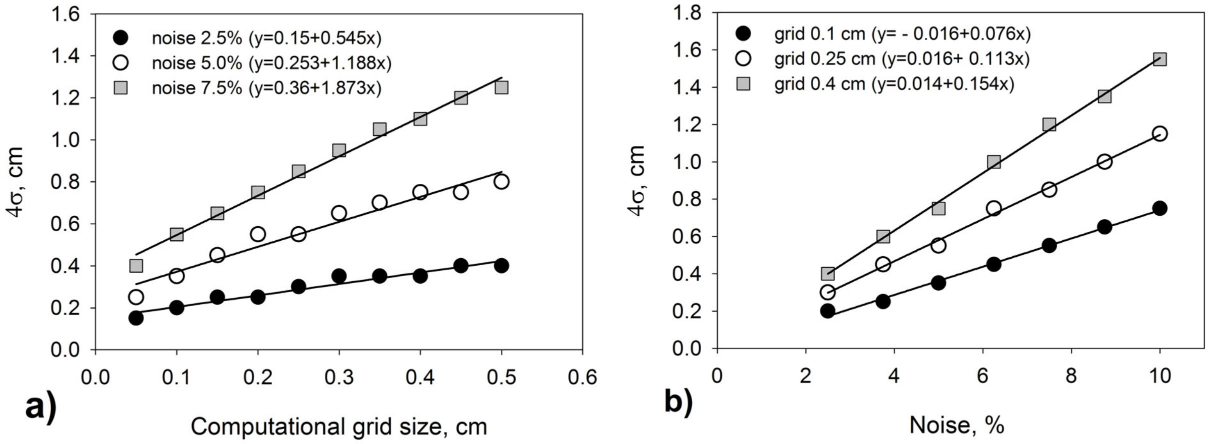

Figure 7. Doubled 95% confidence interval width (4σ) of computed proton range for a 200-MeV proton beam in water-equivalent media as a function of (a) computational grid size for different magnitudes of noise and (b) standard deviation of x-ray CT numbers for different magnitudes of computational grid.

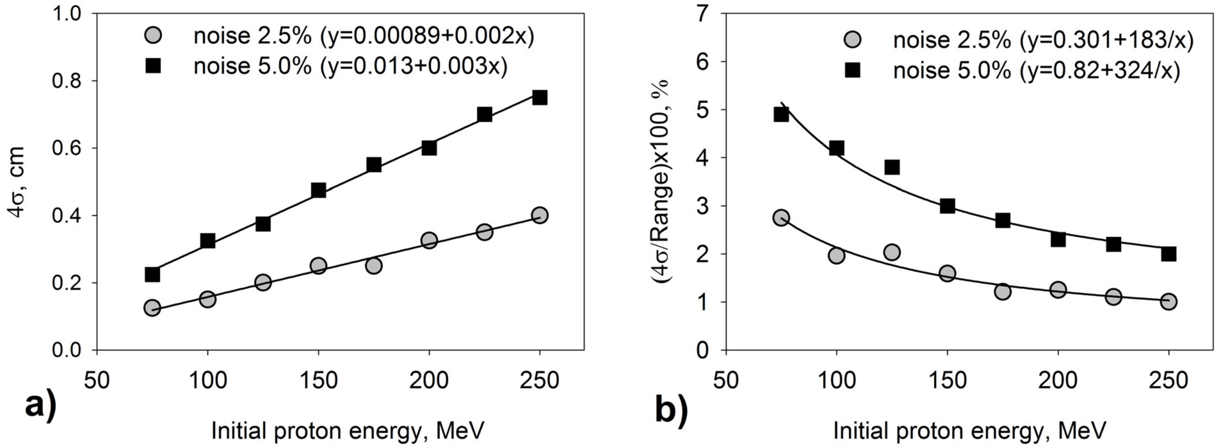

Figure 8. Doubled 95% confidence interval width (4σ) of computed proton range computed as a function of the initial proton energy for different magnitudes of image noise and 0.3-cm grid: (a) absolute value and (b) absolute value divided by the range in water.

the computed proton range and all variables evaluated: dose computational grid size (Figure 7a), standard deviation of x-ray CT numbers (Figure 7b), and initial proton energy (Figure 8a). The linear relationship between the grid size and the range standard deviation indicates that smaller grid sizes can be used to reduce the standard deviation of the proton range. Furthermore, it was determined that the relative standard deviation of the proton range increases as the initial proton energy decreases (Figure 8b).

5.3 Systematic Uncertainties in Pixel Value (Artifacts)

In this report, the classification of the systematic uncertainties in x-ray CT numbers which was used in the AAPM Report 39 and originally proposed by Joseph and Spital (1982) is applied. According to this classification, artifacts are categorized as geometrical errors, algorithm effects, and attenuation measurement errors. Artifacts due to systematic errors are exhibited mostly as rings or streaks due to the nature of rotational geometry and the back projection process. We also note that, despite the broad category of artifacts as presented below, their influence on the image quality is usually quantitatively characterized by a single parameter called field uniformity.

AAPM Report 39 (1993) proposed a uniformity test as a simple and direct approach to determine the accuracy of the reconstruction process and quantitatively evaluate the systematic uncertainties due to artifacts. The uniformity test included scanning a uniform phantom and sampling mean x-ray CT numbers for ROIs of fixed areas throughout the phantom that quantify the presence of systematic variations. There is no universally accepted value for field uniformity; however, modern scanners can provide field uniformity of ±5 x-ray CT number units or better under most scan conditions.

5.3.1 Geometric Artifacts

Geometric artifacts are those related to the geometry of the source and detector array of the scanner. They can appear on an x-ray CT image due to errors from inadequate ray sampling and inconsistencies in the spatial position of rays or projections. AAPM Report 39 (1993) provided a description for the following geometric artifacts:

1. aliasing that appears as faint streaks radiating from bone edges or other high-frequency objects,
2. edge gradient streaks due to sharp discontinuities in attenuation within the finite width of the sampling ray,
3. geometric misalignment in the detector or x-ray source, and
4. motion artifacts due to patient motions.

In addition to the classifications above, it is important to mention artifacts due to:

5. partial volume averaging,
6. presence of objects outside the scan field-of-view, and
7. high-density metallic objects.

Partial volume averaging artifacts can occur when different materials are present within a voxel. This type of artifact can be minimized by reducing the voxel size and slice width. The presence of objects outside the scan field-of-view (SFOV) affects the x-ray CT number significantly due to incomplete information of the anatomy. Large patient size, arm position, and the patient not being centered within the reconstruction circle are typical causes of this artifact. Wide-bore scanners with large SFOVs can be used to minimize this effect.

The presence of high-density metallic objects such as prostheses, dental implants, or implanted seed markers can create severe streaking artifacts due to incomplete attenuation data. Solutions for minimizing metal artifacts when metal objects cannot be excluded from the scan volume include increasing the kV or mA and using a thinner slice thickness. One of the ways of increasing the photon energy is to use megavoltage x-ray CT scanning, which will be discussed in detail in section 5.6.2. Several other reconstruction methods have also been proposed to reduce the metal artifacts in x-ray CT images, such as segmentation and interpolation techniques in sinograms.

5.3.2 Spatial Resolution Limitations and Reconstruction Algorithm Effects

A small object or sharp attenuation edge can be blurred into surrounding pixels. For a small attenuating object, such as a small bone or implanted fiducial marker, the pixels containing the object will have a reduced value, and the pixels surrounding the object will have an increased value. Similarly, those pixels on the high-attenuation side of an edge will have a reduced value, while the pixels on the low-attenuation side of the edge will have an increased value. There is always some blurring in every x-ray CT image, but lower-spatial-resolution algorithms increase the blurring effect (with associated lower noise) while higher-spatial-resolution algorithms produce less of a blurring effect. There are a number of factors that affect blurring of objects in the image:

1. alignment and stability of the source, detector, and gantry
2. focal distribution function (FDF)
3. geometric magnification
4. detection function
5. spatial sampling (views, channels, slices)
6. detector primary speed response time
7. integration interval
8. image reconstruction
9. location in images

The focal distribution function (FDF) of the x-ray source, the detection function (DF), and the geometric magnification, which is dependent on the distance from the source along the ray sample in the SFOV, comprise the optical transfer function (OTF), which determines the inherent spatial resolution of the system (Yester and Barnes, 1977). The amount of blurring is dependent on the size of the x-ray tube FDF and the DF. The DF is the effective active detection width of a detector cell and is somewhat less than the cell pitch. At any given point along a line integral sample, the OTF is a convolution of the effective projected FDF and the effective detection function (DF).

If we assume that the FDF is rectangular, the smallest projected size is generally for the ray sample nearest to the isocenter (see Figure 9). As the ray angle (α) increases, the width of the projected FDF increases due to the orientation on a relatively small target angle (usually between 7 to 12 degrees). This causes an increasing radial blurring with distance from the center of the SFOV. It is also clear from Figure 9 that the effective FDF decreases with increasing distance from the x-ray source due to changing magnification. Although not shown in Figure 9, the effective DF also decreases with distance from the detector; thus, as the distance from the source increases, the effective FDF decreases, while the effective DF increases.

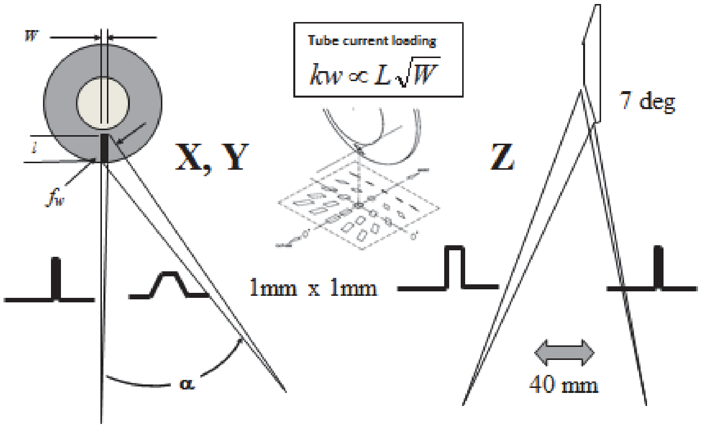

Figure 9. Projected focal distribution function envelope from source-to-detector surface. The projected focal spot size changes with fan angle (x,y) and cone angle (z). Reprinted from Toth (2012) with permission from Springer.

Modern scanners have detectors with fast primary speed response times, typically only a few microseconds or less. Detectors on some earlier systems, however, had slower response times that would cause an azimuthal blurring of the line integral samples. The azimuthal blurring also depends on the sample interval that, in turn, depends on the number of views collected per rotation. Other factors that affect the inherent resolution of the OTF are the stability and alignment of the gantry system to which the x-ray tube and detector are mounted. Mechanical vibrations of the OTF relative to the scan space during the scan acquisition produce blurring or streaking.

The sample spacing between rays is also a factor since the supported resolution cannot exceed the spatial Nyquist frequency. To improve the effective Nyquist sampling, detectors for third-generation scanners are offset by one quarter of the detector pitch. In a 360° scan, this causes rays to be interleaved, thus improving the Nyquist limitations (La Rivière, 2004). For this strategy to work properly, the x-ray tube alignment must be carefully adjusted and be stable to maintain appropriate spatial sampling to avoid reduced resolution and increased aliasing artifacts.

Some scanners employ an in-plane dynamic focal spot shifting where the focal spot is alternately wobbled on the anode to the position of a first projection sample after the gantry has rotated a distance equal to one-half the detector pitch (Flohr et al., 2007). This creates a second set of projection samples that can be interleaved with the first position to double the number of line integrals, thereby increasing the Nyquist frequency of the projection. Dynamic focal spot positioning usually also relies on careful alignments to achieve quarter-offset of the double-sampled projections.

The important point to remember regarding resolution blurring is that the OTF is not isotropic within the SFOV due to the factors discussed above. The peak scatter function will thus vary as a function of position within the SFOV. Generally the resolution is best within a region near the center of the SFOV and degrades as the distance from the center of the SFOV increases due to radial and azimuthal blurring.

Although the focal distribution function (FDF) is considered to be the primary region on the anode that is producing x-rays, off-focus x-rays can also be produced as electrons are accelerated toward the anode, backscattered, and then reaccelerated by the positive potential of the anode. Many modern x-ray tubes have metal frames and electron collectors for backscatter, minimizing much of this off-focus radiation. X-ray tubes with higher levels of off-focus radiation will produce a very broad low-intensity blurring that is generally not apparent, except at object edges with high-attenuation transitions, such as brain tissue near the skull or the tissue around the ribs near the lungs (Figure 10). These

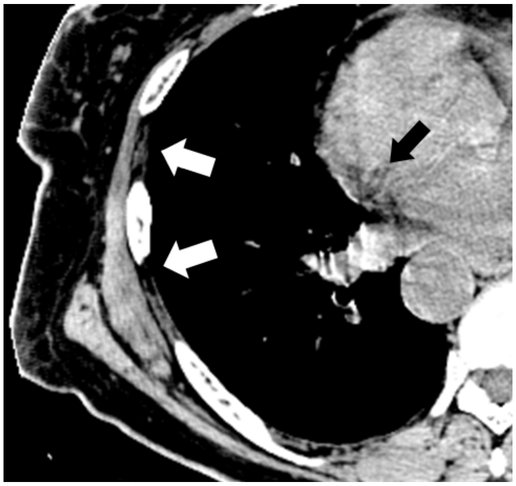

Figure 10. White arrows: example of reduced HU values due to off-focus radiation. Black arrow: example of shading artifact due to cardiac motion. Reprinted from Toth (2012) with permission from Springer.

tissues can experience significant x-ray CT number reductions of up to 100 x-ray CT number units, due to off-focal radiation blurring effects that can extend as much as a centimeter on either side of the transition. Although software corrections are sometimes employed, they are not fully effective in minimizing such effects. In some cases, these corrections can also produce streaking artifacts or edge enhancements, especially when there is a long relatively straight attenuation transition.

In addition to the OTF, the reconstruction algorithm or apodization filter has a significant effect on the spatial resolution of the image; however, it can only modify the inherent limitations of the OTF. These include the effects of both the OTF and the apodization used for the reconstruction algorithms. In general, most MTF (modulation transfer function) curves for general diagnostic protocols have a 50% modulation of about 4 lp/cm to 5 lp/cm. A 50% modulation at 5 lp/cm means that a 1 mm image feature with a spatial frequency of 5 lp/cm will be reproduced at half its real x-ray CT number.

Some of the MTF curves have spatial frequency regions that increase above unity before decreasing to lower values. These are edge-enhancing filters that boost edges. These filters may cause the x-ray CT numbers at the edges to be artificially higher than the true values on the high-attenuation side and artificially low on the low side. These algorithms can also produce ringing effects around high-frequency features.

While many of the factors regarding spatial resolution and blurring discussed above are dependent on the inherent design of the scanner, there are some factors that can be controlled by the user. When accuracies around small features are important, the user should select a protocol that employs:

- the smallest available focal spot,
- a high-resolution reconstruction algorithm, and
- dynamic focal spot positioning when available.

The user should be cautioned, however, that changing some parameters of a protocol will necessitate measuring a new x-ray CT number to RLSTP conversion function. Failure to do so may create errors larger than incorporated into the uncertainty estimates.

Another factor that the user can affect to reduce the magnitude of uncertainties is to ensure that preventive maintenance procedures for the scanner are followed, especially with regard to system alignments. Some scanners may have hidden indirect parameters or settings that affect spatial resolution. For example, the scanner focal spot size may be a function of the tube loading. In an auto-exposure protocol, the large or small focal spot will be determined as a function of patient size since tube loading increases with increasing patient size. In addition, low-signal algorithms may affect the resolution perpendicular to the long axis of the patient if additional filtering is used to minimize the severe streaking artifacts that would otherwise occur in the image. These algorithms, as well as other parameters, can affect the x-ray CT numbers in some regions of the image. It is recommended that the user fully understand how a particular make and model of scanner behaves and ask the manufacturer about any item in question.

5.3.3 Attenuation Measurement Errors

The x-ray CT image is composed of x-ray CT numbers at each pixel location that are related to the x-ray linear attenuation coefficient μ of the material at that location. The measured values of μ in a diagnostic x-ray CT image are usually presented in terms of Hounsfield units (HU), but in some TPSs the older x-ray CT number parameter is used. The HU scale is defined such that measured values ($\mu_{x,y}$) are presented in the x-ray CT image as the ratio of the $\mu_{x,y}$ of the material relative to the μ for water (μ_w) times 1000 minus 1000:

$$HU_{x,y} = \frac{\mu_{x,y}}{\mu_w} \times 1000 - 1000 \qquad \text{(Eq. 12)}$$

Thus, water ideally will have an HU of 0 and air will have an HU of –1000. One inherent problem with this definition is that the μ of all materials, including water, is not a constant, but has a value that is a function of the x-ray energy (keV).

Since HUs are relative to the μ of water, x-ray CT systems are calibrated and corrected for water beam hardening to try to maintain a relatively constant effective μ throughout the SFOV for water over all x-ray energies. If not corrected properly, the HU of water will not be a constant within a water phantom image. With proper calibration and correction, the image of a water phantom will ideally have an HU of zero within a tolerance specified by the manufacturer. However, the μ of other materials can still maintain an energy dependence relative to water. The HU of a pixel for these materials depends on the μ relative to water and the effective energy of that pixel location within the image.

The effective energy, in turn, depends on the kVp, source target angle, source filtration, and the amount and type of patient tissues in the beam paths contributing to that pixel value. Figure 11 shows estimated HUs computed for several materials assumed to be at the center of a range of phantom diameters for various kVp settings, at typical quality equivalent filtrations (QEFs) of 4.6 mm Al and 7.6 mm Al. The QEF is the amount of aluminum required to achieve the same beam quality (Half Value Layer) if the system filtration was replaced by aluminum. The HUs were calculated using Equation 13:

$$HU = \left(\frac{\ln \sum I(S_k)\exp(-\mu_w(S_k)l - \mu_X(S_k)\Delta l)}{\ln \sum I(S_k)\exp(-\mu_w(S_k)l - \mu_w(S_k)\Delta l)} - 1 \right) \times 1000 \qquad \text{(Eq. 13)}$$

where I is the incident x-ray intensity, S_k is the x-ray energy, μ_w is the linear attenuation coefficient of water, μ_X is the linear attenuation coefficient of a sample material, l is the length of material, and Δl is a 1-cm length of the sample material.

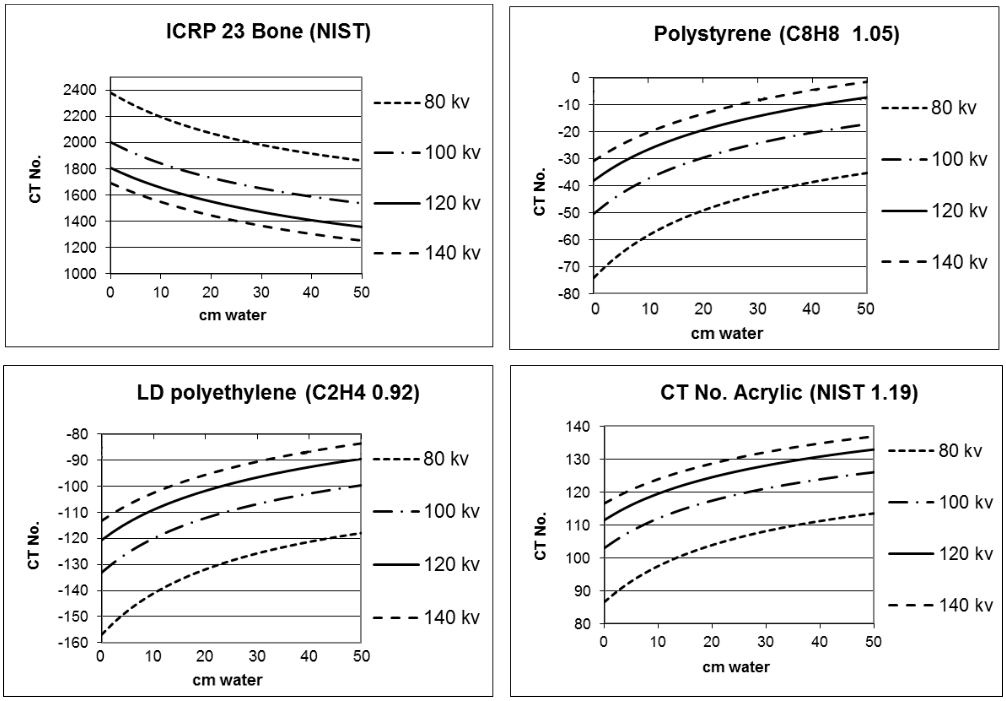

Figure 11. Example x-ray CT numbers for bone, polystyrene, polyethylene, and acrylic versus water phantom diameter (7 degree target angle, H = 4.6 mm Al quality equivalent filtration (QEF), B = 7.6 mm quality equivalent filtration (QEF)). Reprinted from Toth (2012) with permission from Springer.

The range of HUs for high-Z materials such as the calcium in bone can be very large. In the simulation, ICRP 23 bone has a range of HUs from 1200 to 2400. The presence of high-atomic-number materials such as bone or metal prostheses can create beam-hardening artifacts. The shading in the soft tissue region of the head image in Figure 12 is caused by bone beam hardening. Although corrections for beam hardening are generally included for some x-ray CT reconstruction modes, especially for head scanning (Joseph and Spital, 1982: Chen et al., 2001; Kyriakou et al., 2010), these corrections do not completely eliminate such artifacts.

Artifacts due to partial volume effects can be indistinguishable from beam hardening; however, such artifacts were much more common on older single-slice scanners and four-dimensional x-ray CT scanners using cine mode with discrete patient positioner positions. Multi-detector scanners with narrow slices are less prone to partial volume artifacts since larger width slices are summations from individual detector row data after the log correction step. Scattered x-rays can also produce similar shading effects between dense features. Scatter, as well as other artifacts such as cone beam, can be minimized by using narrow collimation.

Other sources of error can occur when an x-ray CT scanner is in need of servicing, as shown in Figure 13. Scanners periodically require recalibration to account for detector response drift that would otherwise create band, ring, or center artifacts.

5.3.4 Correction of Systematic Uncertainties in Treatment Planning

The error in the computed light ion beam range, CR, due to systematic errors in the x-ray CT number can be calculated according to Equation 14. Simpler equations can, however, be based upon Equation 10 using certain simplifying assumptions. For example, assuming that the stopping power is independent of energy, a parameter α with a value between 0 and 1 ($0 \le \alpha \le 1$) may be introduced where α is the fraction of range affected by the systematic uncertainty, u(System). The range uncertainty due to the x-ray CT number can then be obtained by the following equation:

$$\frac{u(CR)}{CR} = \alpha \cdot \frac{u(System)}{XCTN} \qquad \text{(Eq. 14)}$$

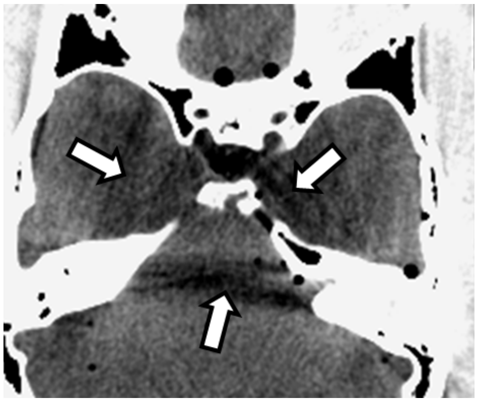

Figure 12. Example of bone beam hardening, partial volume, or scatter artifacts. Reproduced from Toth (2012) with permission from Springer.

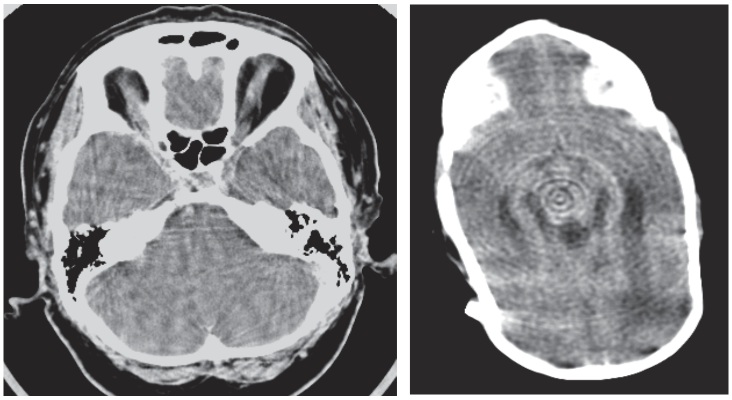

Figure 13. Artifacts that require x-ray CT scanner servicing. Left: vibrations of OTF relative to patient. Right: ring and band artifacts due to detector channel response drift. Reprinted from Toth (2012) with permission from Springer.

Using Equation 14 we obtain that a relative systematic uncertainty in x-ray CT number of 2% affecting the entire ion range (α=1) will produce a 2% error in the ion range. The range uncertainty can, however, be small for larger systematic uncertainties in x-ray CT number if the parameter α is small. For example, a relative systematic uncertainty in x-ray CT number of 10% will produce a 1% error in ion range if the uncertainty affects only 10% of the ion path length (α=0.1).

In practical treatment planning, some artifacts seen as visible streak artifacts are commonly mitigated by the following techniques (Newhauser et al., (2008); see also section 5.6.2):

- selection of gantry angles such that the beam path avoids artifacts (see Figures 17A and 17B)
- manual overrides or automatic tools for x-ray CT numbers available in TPSs (see Figures 17C and 17D)

Dual-energy x-ray CT can, in theory, virtually eliminate beam-hardening artifacts. However, similar-looking artifacts can still be present due to scatter contamination of the measurements or partial volume errors (see section 5.6.3).

5.4 Factors Affecting Uncertainties in X-ray CT Numbers

5.4.1 Scan Field-of-View (SFOV) and Reconstructed Field-of-View (RFOV) Fill Factors

The SFOV must encompass the entire patient as well as any significant external devices in the path of the x-ray beam. In some cases, the manufacturer may provide an extended view reconstruction algorithm. Such algorithms estimate the missing portions of truncated projections (Lewitt, 1979; Herman and Lewitt, 1981). These algorithms are generally reasonably effective, but the user should examine the images for evidence of discontinuous x-ray CT numbers in the regions reconstructed beyond the SFOV and perform formal testing. Figure 14 shows the effect of an object being not centered for both typical and extended SFOVs. Careful studies and analysis should be performed before using an extended SFOV for light ion beam planning.

The reconstructed field-of-view (RFOV) generally will not lead to significant x-ray CT number inaccuracies if targeted smaller than the patient as long as the SFOV includes the patient (or truncated

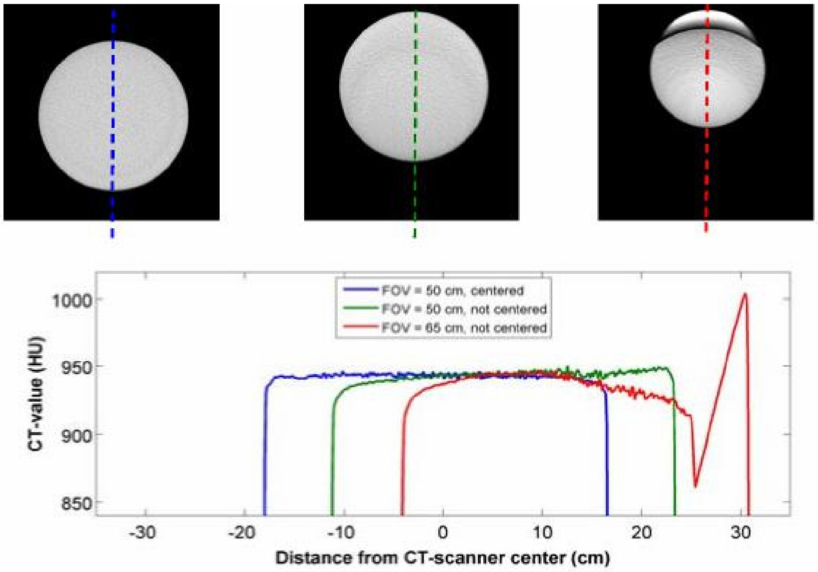

Figure 14. Effect of object not being centered within the SFOV for typical and extended SFOVs.

views are estimated reasonably well). A very large SFOV, however, can reduce spatial resolution and blur small features if the reconstruction filter cutoff is decreased to avoid image aliasing for the larger pixel size.

5.4.2 Patient Size, Positioning and Presence of Different Materials

Patient size and positioning within the SFOV can also influence x-ray CT number accuracy. Generally, tissues with attenuation characteristics similar to water are minimally affected, but other tissues, such as bone or contrast-enhanced tissue, can change significantly depending on the effective energy. Larger-size patients increase the effective energy of the x-rays incident on the detectors, but the effective energy is also dependent on kVp selection. Figure 15 shows the change in HUs calculated at various kVp settings and water path lengths for some tissue type models as defined in ICRU Report 44 (ICRU, 1996).

Patient positioning within the SFOV interacting with the bowtie filter can also change the effective energy and, hence, the HUs in image regions. Bowtie filters shape the beam intensity to better conform to the patient (Toth et al., 2005) and can reduce patient dose, especially peripherally, as well as reduce scattered x-rays and associated shading artifacts. If the patient is miscentered in the SFOV, however, the increased attenuation of the bowtie away from the isocenter can add to the patient attenuation (Toth et al., 2007), increasing the effective energy and the probability of intense noise streaking in the image. Miscentering is common, but it is easily addressed if the technologist is made aware of the adverse effects and exercises care in patient positioning. Proper centering in the x-ray CT scanner SFOV will improve the consistency of x-ray CT numbers and reduce the noise variance due to patient size. Registering the patient to the patient positioner using hemicylindrical pods can also improve consistency of x-ray CT numbers because it forces the patient's shape closer to a circle and maintains all patient tissues within the scanning volume and out of the view of the calibration channel paths.

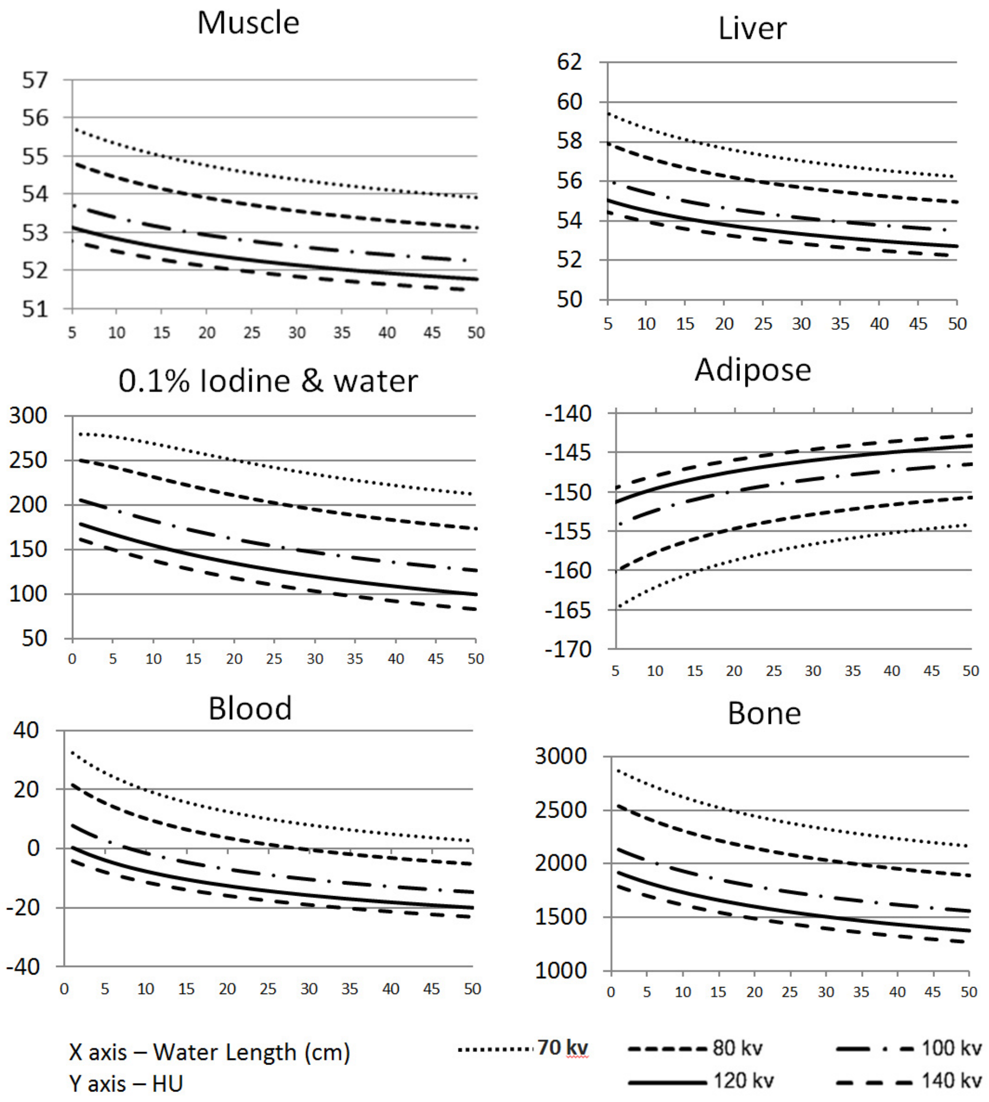

Figure 15. HU values for various ICRU tissue models and kVp settings for an x-ray beam with a quality equivalent filtration of 7.6 mm Al for a 7-degree tungsten anode. The incident spectrum was obtained from a program utilizing CASINO from Sherbrooke University (http://www.gel.usherbrooke.ca/casino/What.html). Reprinted from Toth (2012) with permission from Springer.

5.4.3 Helical Scanning Versus Slice-by-Slice Scanning

Helical or spiral scanning with continuous table motion is very common for body and chest procedures. Helical scans can produce artifacts near dense features that change rapidly within the slice plane, such as the ribs in a chest scan (Figure 16). These artifacts are intensified at high pitch rates. The pitch is the table travel per gantry revolution divided by the total length of the active detector rows. These artifacts do not exist in axial scan modes; however, cone-beam artifacts can still be present near such features. Reducing the pitch or scanning in axial mode can reduce these helical artifacts.

Another way to reduce helical artifacts is by dynamically moving the focal spot in the Z axis (Flohr et al., 2007). A helical artifact is essentially a form of Z axis aliasing. Dynamically moving the

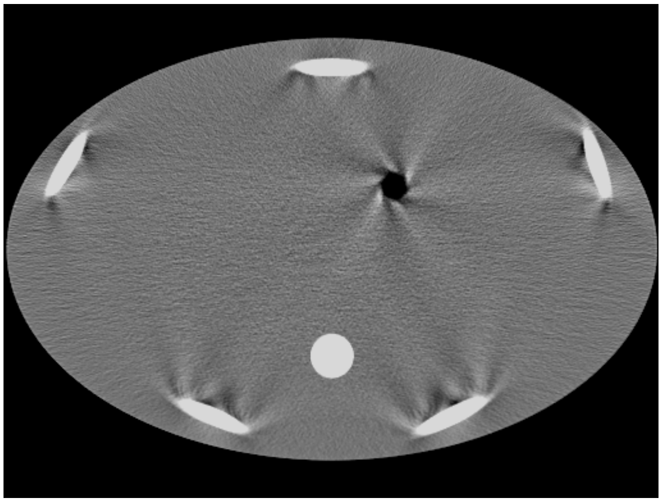

Figure 16. Example body phantom showing helical artifacts near the angled rib rods and domed air cavity. Reprinted from Toth (2012) with permission from Springer.

focal spot in Z on the anode creates a second set of samples at intermediate detector row positions, which minimizes helical artifact. This approach requires that the Z axis source collimation be opened sufficiently to accommodate both focal spot positions, increasing x-ray scatter as well as patient dose. It is not possible to track the rapid focal spot movements required by this technique with a dynamic collimator, as it is in conventional helical scanning (Toth et al., 2000). Sometimes these artifact reduction techniques can not be explicitly controlled by the user, but the user should be aware of the consequences. If an artifact is not satisfactorily reduced by the reconstruction algorithm, then the planner may need to contour the artifact regions and manually reassign the x-ray CT numbers or RLSTPs.

5.4.4 Multi-slice Multi-detector X-ray Computed Tomography Scanners

Multi-slice multi-detector x-ray CT scanners have largely replaced single-slice models. These multi-slice multi-detector x-ray CT scanners have the advantage of covering more anatomy using narrower slices and shorter total exam times. These multi-slice multi-detector x-ray CT scanners are thus less likely to encounter patient movement and associated artifacts during the exam and generally produce less intense helical artifacts. The use of a wider collimator to accommodate the multiple detectors, however, generally produces more helical and cone-beam artifacts. When the patient's water-equivalent diameter varies quickly along the Z axis (patient's long axis)—such as at the top of the head, in the transition zone from the neck to the shoulders, or the transition zone from the lungs to the liver—the user may wish to use narrow collimation to reduce errors in the x-ray CT numbers within the transition volume.

5.5 Uncertainty Measurement and Scanner Calibration

Scanner calibration, QA, and periodic preventive maintenance are critical for minimizing image quality issues. Detector channel response can drift for a variety of reasons, leading to ring, band, or center artifacts if periodic calibrations and servicing is ignored. Although modern scanners are designed to minimize these drifts, following the QA program indicated by the manufacturer is essential. Changes in detector channel gain of as little as 0.02% relative to the calibrated value can create a visible center artifact.

Since x-ray CT scanners employ a variety of design concepts and features, it is not possible to provide specific scanner uncertainty ranges for x-ray CT numbers. The stability of x-ray CT numbers and associated uncertainty ranges will depend on the specific make and model of the scanner and how well it is maintained.

In this report, the authors have tried to provide a basic understanding of the factors that create x-ray CT number variations and, where possible, to give some understanding of the potential uncertainty ranges. To understand the penetration uncertainty associated with a particular scanner, one would need to scan a set of anthropomorphic phantoms with realistic tissue-equivalent materials using the set of operating conditions at the facility for scanning patients.

5.6 Image Quality Improvements for Light Ion Beam Treatments

5.6.1 Mitigation by Patient-specific Scaling of X-ray CT Numbers

The effects of patient-specific scanning conditions on the scanner-generated x-ray CT numbers can be partially mitigated by scaling the x-ray CT numbers to approximately match the values of materials when the x-ray CT-number-to-ion RLSTP conversion function was determined. One such scaling scheme, provided by Wrightstone et al. (1989) and reproduced in Moyers et al. (2010), is given by Equation 15. This scheme results in air always having a scaled x-ray CT number (SXCTN) value of 0 and water always a value of 1000:

$$SXCTN = \left(\frac{XCTN_{mat} - XCTN_{wat}}{XCTN_{wat} - XCTN_{air}} \right) + 1 \times 1000 \qquad \text{(Eq. 15)}$$

Practical considerations for acquiring the data from which to scale have been previously given (Wrightstone et al., 1989; Moyers et al., 2010; Moyers and Vatnitsky, 2012). Basically, the process involves sampling x-ray CT numbers from the patient images and comparing them with standard values; for instance, water can be found in rectal immobilization balloons, the aqueous and vitreous humors of the eye, and cerebro-spinal fluid. One can also scale numbers to an externally placed water bottle or the common values of different tissues such as brain and muscle.

At the time of the writing of this report, not all TPSs supported patient-specific x-ray CT number scaling. If scaling is not performed by a particular TPS, then the penetration uncertainty associated with x-ray CT numbers would need to increase compared to that used with TPSs that do provide scaling.

An alternative method to scaling x-ray CT numbers is to apply different scaled x-ray CT-number-to-RLSTP conversion functions. In this scheme, the selection of the appropriate conversion function would require sampling x-ray CT numbers for the patient images similar to that done for the scaling scheme.

5.6.2 Megavoltage X-ray Computed Tomography

Although not used much in the clinic, several investigators have shown that it is possible to substantially reduce image artifacts due to the presence of metallic objects by performing x-ray CT with megavoltage x-rays. The reason for this is that kV photons are severely attenuated by high-density, high-atomic-number materials, whereas MV photons are less attenuated (Brahme et al., 1987; Langen et al., 2005; Newhauser et al., 2008; De Marzi et al., 2013). The severe attenuation at kV energies causes a starvation of transmission data needed to properly reconstruct an x-ray CT image. For example, the megavoltage x-ray CT approach provides a method to accurately image a patient with a titanium hip prostheses, whereas the corresponding kilovoltage x-ray CT images exhibit a region of missing information in and or near the prosthesis. As with kV imaging, megavoltage x-ray CT numbers must be converted to RLSTPs for light ion planning. A function for converting megavoltage x-ray CT numbers to RLSTPs has been provided by Moyers et al. (2010) and is given in section 7.5.

Soft tissue contrast and spatial resolution in megavoltage x-ray CT scanning is, however, inferior to kilovoltage x-ray CT. An optimal approach for light ion beam planning might use a hybrid approach using both kilovoltage x-ray CT and megavoltage x-ray CT, as investigated by Newhauser et al. (2008). In their study, a megavoltage x-ray CT scan was performed for a phantom and a test patient with a metal prosthesis using a TomoTherapy HI-ART II unit (TomoTherapy Incorporated, Madison, Wisconsin). Both the kilovoltage x-ray CT number and megavoltage x-ray CT-number-to-RLSTP conversion functions were determined using a stoichiometric method (Schneider et al., 1996). Deviations between individual x-ray CT numbers and the fitted conversion function values were smaller for the MV scanner than the kV scanner, particularly in the important soft-tissue interval from 800 to 1200 x-ray CT number values. This finding suggests that megavoltage x-ray CT imaging may be more accurate than kilovoltage x-ray CT imaging for determining light ion penetration (see Figure 17). For the hybrid kilovoltage/megavoltage CT planning approach, images were first registered to one another with the kilovoltage x-ray CT images being used for delineating soft tissues and the megavoltage x-ray CT images being used for delineating the prostheses and proton dose calculations. The results of the hybrid kilovoltage/megavoltage planning were compared to planning with manual corrections of artifact streaks on the kilovoltage x-ray CT images. The findings of the comparison suggested that the hybrid planning approach using registered kilovoltage and megavoltage CT images yielded a better overall result. Using megavoltage x-ray CT images for light ion treatment planning may provide a feasible alternative to manually correcting artifacts on kilovoltage x-ray CT images (see section 7.6).

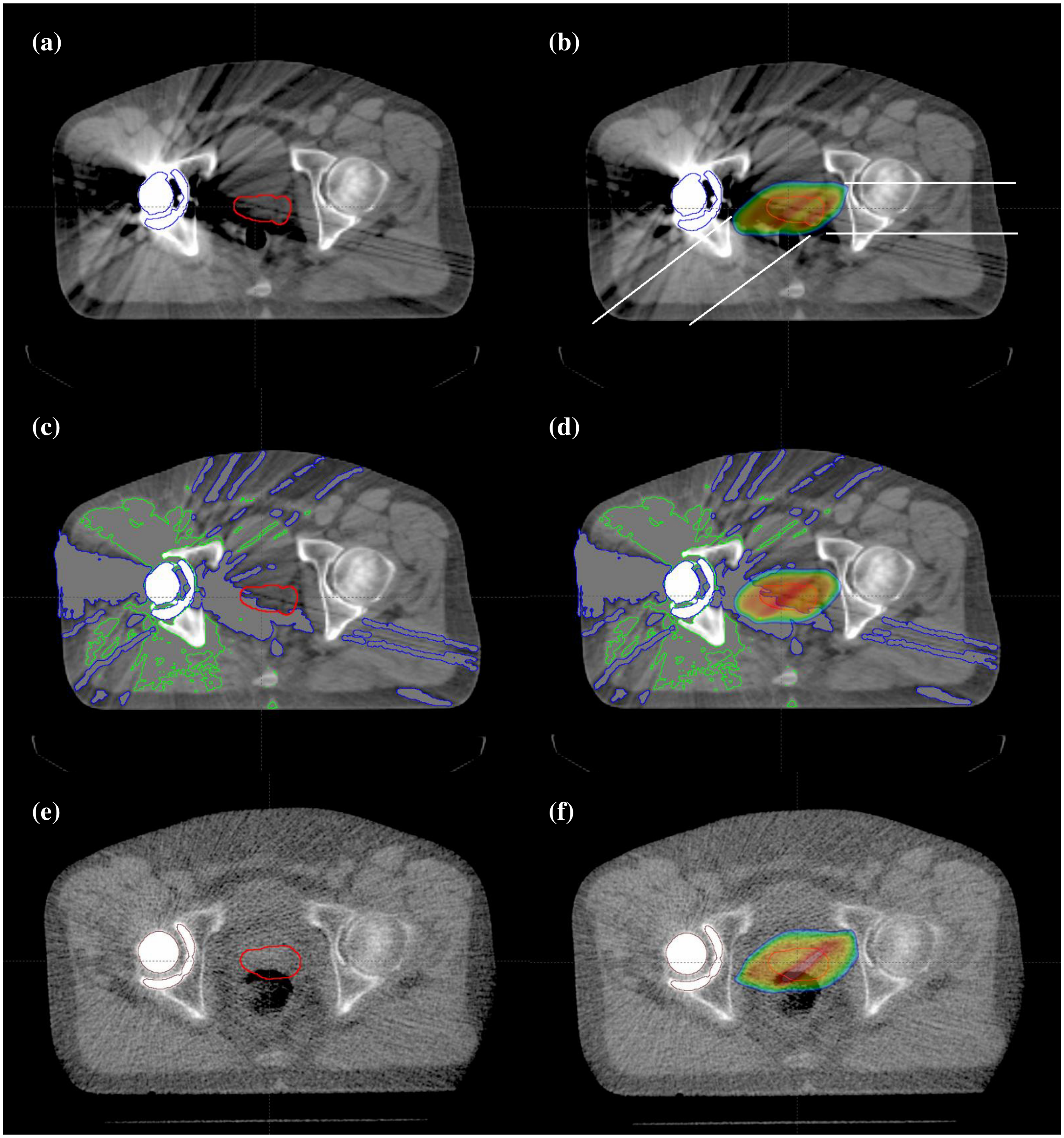

Figure 17. Kilovoltage x-ray CT and megavoltage x-ray CT images of a prostate cancer radiotherapy patient with a metal hip prosthesis. (a) The kilovoltage x-ray CT image reveals image saturation within and adjacent to the prosthesis, as well as streaking artifacts emanating from the prosthesis and extending to the contralateral skin. (b) Calculated dose distribution using uncorrected kilovoltage x-ray CT images. White lines show the lateral edges of treatment fields. (c) An example kilovoltage x-ray CT image after substituting estimated x-ray CT numbers for voxels exhibiting saturation and streaking artifacts. (d) Calculated dose distribution using corrected kilovoltage x-ray CT images. (e) Megavoltage x-ray CT image exhibiting poor soft tissue contrast resolution but free of saturation and streaking artifacts. (f) Calculated dose distribution using megavoltage x-ray CT images Reprinted from (Newhauser et al., 2008) with permission from *Physics and Medicine in Biology.*

5.6.3 Dual-energy X-ray Computed Tomography

Dual-energy x-ray computed tomography (DECT) was first proposed in 1976 by Rutherford et al. (1976). It fell out of favor, however, due to practical difficulties, such as patient motion between the scan acquisitions at the two energies. Recent technological advancements—such as helical scanning, dual x-ray tubes on a single gantry, and fast energy switching—have made dual-energy scanning practical in the clinic. There are three major implementations of DECT: one involves using dual tubes mounted orthogonal to each other, one involves discriminating the energy at the detector level (using layered detectors or photon counters), and the other uses fast kVp-switching of a single tube. The DECT data from the dual-energy scan can either be reconstructed individually and then an energy analysis performed on the reconstructed data or an energy-dependent analysis can be performed prior to reconstruction. The latter method is complicated, but provides additional benefits such as beam hardening effect correction.

DECT has a variety of diagnostic values, such as cardiac studies, contrast-enhanced abdominal studies, bone removal in x-ray CT angiography of base of skull, lung perfusion and ventilation studies, and material differentiation of calcium, iodine, soft tissue, ligaments, tendons, etc. (Johnson and Kalendar, 2010). Compared to single-energy x-ray CT, DECT offers both high contrast (due to the low-energy x-ray beam) and a high signal-to-noise ratio (due to the high-energy x-ray beam). A major advantage of DECT for treatment planning is that it can provide both an estimate of the effective atomic number of materials and the relative electron density. This is significant because having both values can reduce the ambiguity in the determination of the light ion RLSTP for a given x-ray CT number. Another advantage may be the ability to correct for beam hardening artifacts, thereby increasing the accuracy of the x-ray CT numbers for different sizes and shapes of patients.

An accuracy of 1% in the estimated electron density has been claimed when using dual-energy monochromatic x-ray sources (Tsunoo et al., 2008). Yang et al. (2010) showed that the DECT is theoretically accurate and robust compared to the stoichiometric method described by Schneider et al. (1996) which is widely used in clinics. The RLSTP calculated using DECT was robust when the tissue density in a voxel varied and partial volume averaging was present. They showed that the RLSTP is both a function of the relative electron density and the mean excitation energy I_m, the latter being fit to two linear equations—one for soft tissue and another for bone. Though their work was constrained to an ideal x-ray CT—which ignored beam hardening, noise, and other potential DECT artifacts—these artifacts can be minimized by increasing filtration, dose, and smoothing algorithms. According to Yang et al. (2010), the optimal separation of energies for DECT seems to be about 200 keV.

5.6.4 Ion Computed Tomography Scanning

Ion computed tomography has the potential to improve the accuracy of the dose calculations by measuring the ion RLSTPs directly. It eliminates the need for measuring x-ray CT numbers and then converting them to estimated RLSTPs. The conversion of x-ray CT numbers to RLSTPs is not exact because the x-ray attenuation on the Z and Z/A of the material may differ significantly from the dependence of RLSTP on these parameters. Zygmanski et al. (2000) and Schneider and Pedroni (1994, 1996) measured the inaccuracy of proton treatments based on kilovoltage x-ray CT. This inaccuracy was partially attributed to the inaccuracy in x-ray CT number up to a few percent, incomplete modeling of MCS effects, and range differences of up to 1.5 cm for their 219 MeV proton beam. These x-ray CT and conversion inaccuracies make ion computed tomography desirable, as it provides a map of RLSTP as opposed to a map of x-ray attenuation, as in the case of x-ray CT.

The possibility of using light ions for computed tomography was first suggested by Cormack (1963), and the first application was reported in 1972 by Goitein et al. (1972). Immediately it was clear that ion computed tomography has superior density resolution compared to x-ray CT for a given dose level (Hansen et al., 1981). Ion computed tomography acquisition, however, is not as straightforward as x-ray CT due to multiple Coulomb scattering and energy straggling. Various prototype scanners have been reported, with investigators measuring different physical quantities and using different algorithms for reconstruction. For example, Fabrikant et al. (1982) reported scanning a metastatic melanoma in the cerebral cortex of a patient with a 670 MeV/n neon ion beam. Schulte et al. (2004) and Petterson et al. (2006) measured the tracks of individual protons using both entrance and exit Si detectors and energy loss using scintillator-based calorimeters. Later, Schulte et al. (2005) and Li (2006) gave specifications for a proton CT scanner both for imaging for treatment planning (optimized for accuracy) and for treatment verification (optimized for speed). An iterative algorithm was used to trace the nonlinear paths of the protons that traverse a simulated patient. The most important parameter in ion CT is the relative electron density resolution, which is fundamentally limited by energy resolution. This resolution is higher for protons than for x-rays for a given dose level, especially for smaller anatomical cross sections. The spatial resolution is, however, limited by MCS. Zygmanski et al. (2000) showed that the relative electron density for PMMA, bone, and oil (fat), were significantly better with cone-beam proton CT than with fan-beam x-ray CT and compared well with measurements with Faraday cup, ICRU values, and Schneider's stoichiometric method. The system used the method of linearly decreasing signal with linearly increasing thickness and employed a camera coupled to a CCD detector. At the time of writing this task group report, the image reconstruction times were quite long, but the advent of GPU processors bodes well for accurate but computationally intensive algorithms, such as iterative algebraic methods. Currently the first scanner to go into routine clinical service is not expected until 2019.

5.7 Recommendations

- Users should carefully study the details of their specific scanners and any nuances that could affect the CTN, including anticipated artifacts. If artifacts are present in an image, the impact of these artifacts should be evaluated and mitigations applied, if possible.
- A CTN scaling method should be implemented to improve the CTN consistency for different size and shape patients.
- Regularly scheduled maintenance and quality assurance testing is required to keep errors within the stated uncertainties for treatment planning given at the time of commissioning. Special attention should be paid to CT image parameters, such as uniformity of CTN and CT image noise, which can affect the computed penetration of light ion beams.

6. Absolute and Relative Linear Stopping Powers (RLSTPs)

6.1 Usage and Accuracy of Stopping Powers

Uncertainties in the absolute value of ion stopping powers can be of concern in several different situations. The first concern is when the beam data entered into the TPS database, such as a pencil-beam distribution, had been calculated analytically or by Monte Carlo simulation instead of by measurements. The second concern is when the entire dose distribution is calculated by Monte Carlo, including the simulation of the radiation head and the patient. The third concern is when calibrating the ion energy extracted from the accelerator and transported to the patient (see, for example, Moyers et al., 2007).

Currently, the absolute stopping power of water for protons is only known to about ±1%, and there is disagreement between different tabulations. As an example, the range tables given by Janni (1982) and ICRU 49 (1993), both of which were determined by integrating energy loss calculated from stopping powers, differ by 3.6 mm at 250 MeV. A similar problem exists for ions heavier than protons (ICRU 73, 2005). A number of publications over the years have shown that the I-value used in calculation of the stopping powers is probably closer to the value used by Janni (1982) rather than that used by ICRU (Bischel and Hiraoka, 1992; Bischel et al., 2000; Dingfelder et al., 1999; Kramer et al., 2000; Moyers et al., 2007; Schardt et al., 2008). Andreo (2009) has shown the effect on depth dose using the different tabulations. Sigmund et al. (2009) released an errata for the ICRU 73 report in which the I-value for liquid water for light ions was increased to 78.0 eV, a value midway between the ICRU 49 (1993) and Janni (1982) values. An ICRU report on key data is expected to be published in the near future containing new tables of agreed-upon I-values; this data should lead to reduced uncertainties.

The values of RLSTPs are more commonly considered than the absolute stopping powers because most TPSs, as of 2014, still use dose calculation algorithms based upon measurements in water. Most materials for which RLSTPs are needed are included in the patient's x-ray CT scan and are converted to RLSTPs using a conversion function (see next section) generated for tissue materials. For soft tissues and bone, the 2 SD uncertainty of the RLSTP varies from 0.4% to 3.3%, with most tissues being less than 1.6% (see, for example, Schaffner and Pedroni, 1998). For other non-tissue-like materials through which light ions pass, the situation may be different. Implanted devices are often made of high-density and high-atomic-number materials and may result in non-sensical x-ray CT numbers. For these objects, their spatial region within the x-ray CT scan may need to be contoured and the real RLSTPs assigned to those contoured regions. Although registration and immobilization equipment, such as table tops, facemasks, and pods are usually included in the x-ray CT scan, use of a conversion function generated for tissue may not correctly convert the x-ray CT number to the correct RLSTP and, again, the devices may need to be contoured and the real RLSTP values assigned. For measurements of basic data and verification of patient plans, dosimetry phantoms are often used. Although these phantoms are designed to mimic real tissues, their RLSTPs are not identical, and usually measured RLSTPs are used for these phantoms.

6.2 Energy and Ion Species Dependence

The energy dependence of the RLSTP is generally small for low-atomic-number materials such as tissue (Moyers et al., 1992; Moyers et al., 2010; Zhang and Newhauser, 2009) and most planning systems ignore this dependency. Most of the path length of a light ion beam through a patient occurs within the plateau region where the light ions have medium to high energies, and the RLSTP value changes little with penetration (≤1.5% for tissues, ≤8.5% for high-Z materials). The fraction of the total path length that occurs when the energy is low and the RLSTP is changing more dramatically (≤5.6% for tissues, ≤35% for high-Z materials) is relatively small. Using standard RLSTPs determined for an intermediate energy (130 to 180 MeV protons, for example) thus incurs only a small error on the range. The energy dependence is not, however, zero, and there may be instances—such as when the beam passes through high-density, high-atomic-number implants—when ignoring this dependence can introduce an error.

Usually the same RLSTP for the same materials can be used by a TPS for different incident ion species. Moyers et al. (2010) has shown that the ion species dependence of RLSTP is less than 2% for proton, carbon, and iron ions.

6.3 Scattering Powers

Another parameter that influences accurate dose simulations is the relative lateral scattering power (RLSCP). This parameter usually goes hand-in-hand with the RLSTP in that it is material- and energy-dependent. Unlike RLSTPs, however, it is very dependent upon the ion species. Unfortunately, there is little published literature on scattering power and its uncertainties. For discussions of ion scattering powers, see Kanematsu (2009) and Gottschalk (2010). For both pencil beam and Monte Carlo treatment planning dose calculation methods, standard practice relies on iterative fitting of scattering parameters to measured distributions.

6.4 Recommendations

- The user should become intimately familiar with how all applications and methods of their TPS use absolute and relative linear stopping powers and the effects of uncertainties on plan optimization and dose calculations.
- Measurements of RLSP over a range of energies should be performed as part of the commissioning process for various devices that might intercept the beam placed either external to the patient or internally.

7. Conversion of X-ray CT Numbers to RLSTPs

7.1 Models

In addition to the uncertainties associated with the x-ray CT numbers and the RLSTPs, there are also uncertainties associated with the functions for converting the x-ray CT numbers to RLSTPs. Over the years there have been a number of measured and calculated experiments performed to relate x-ray CT number to the RLSTP of light ions. After the data is acquired, a model is fit to the data, and then the model tested for how well it predicts the measured data. These models include formulas, table look-ups, and groupings of materials for Monte Carlo simulations. Most experiments have shown that the models result in relatively small residual errors for soft tissues of about 3.2% at the 2 SD level (Battista et al., 1980; Mustaffa and Jackson, 1983; Schaffner and Pedroni, 1998; Schneider et al., 1996; Hünenmohr et al., 2012). Larger residual errors exist for bones, registration and immobilization equipment, and implanted materials (Moyers et al, 1992; Moyers et al., 2010).

In most TPSs, the conversion model is a simple one-step process where an RLSTP is directly assigned to an x-ray CT number via a look-up table with interpolation between the assigned values. In some TPSs, a two-step process is used where the first step links the x-ray CT number to a material definition, and the second step assigns an RLSTP to the defined material. Figure 18 shows a typical conversion function used with a one-step process and a table look-up procedure. At a given facility, a

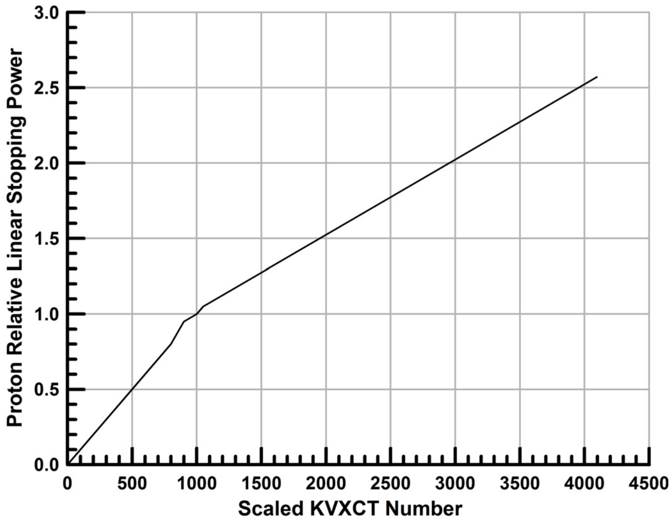

Figure 18. Typical function for converting kilovoltage x-ray computed tomography numbers (kVXCT numbers) to RLSTPs. kVXCT number data for 120 kVp and RLSTP data for protons taken from Moyers et al. (2010). The abscissa is plotted in terms of scaled kVXCT numbers according to the procedure given in section 5.6.1. Figure reproduced from Moyers and Vatnitsky (2012).

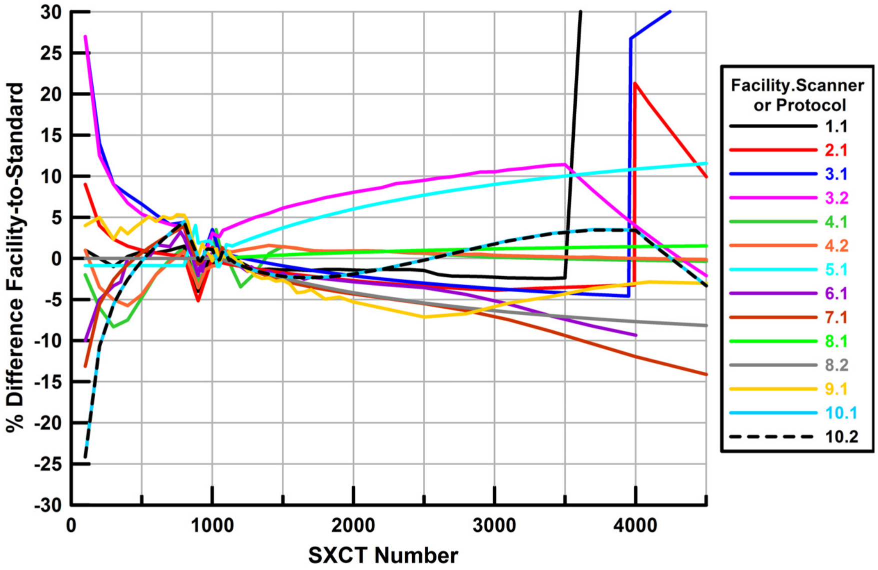

Figure 19. Differences between RLSTPs determined using facility conversion functions and an RPC conversion function as a function of x-ray computed tomography (XCT) number. Reprinted from Moyers (2014) with permission from *Medical Physics*.

separate conversion function should be generated for each scanner protocol (combination of SFOV, kVp, slice width, and reconstruction kernel). A commissioning procedure for obtaining these conversion functions has been given by Moyers and Vatnitsky (2012).

Between 2010 and 2012 the Radiological Physics Center (RPC) performed site visits at operating proton treatment facilities in the United States to evaluate dosimetry and treatment planning practices. Part of this evaluation included acquisition of x-ray CT-number-to-RLSTP conversion functions for the scanners and protocols at each facility and comparison with the facility's conversion functions (Moyers, 2011; Moyers, 2014). The same phantom was scanned at each facility, so the conversion of the x-ray CT numbers using each facility's conversion function should have yielded the same RLSTPs. Figure 19 plots the difference between the RLSTPs determined using the RPC conversion functions and the facility's conversion function. It can be seen that there are quite large differences in the determined RLSTPs between the various facilities, indicating that the uncertainty in converting x-ray CT numbers to RLSTPs is significantly larger than indicated by the single facility experiments. It is readily apparent that different facilities convert x-ray CT numbers around 900 differently; some consider those x-ray CT numbers to be representative of fat, while others consider them to be a mix of air cavities and muscle-type tissue. The biggest region of concern is for lung tissue, because some of the largest conversion discrepancies are demonstrated for tissues within this x-ray CT number range, and large WETs of this material are often traversed by beams before entering the intended targets.

7.2 Contrast

For tumor localization, x-ray CT scans are often performed with contrast injected into the body. The presence of the contrast material alters the x-ray CT numbers and, subsequently, the values of the RLSTPs used to design the portals and calculate the dose distributions. If the x-ray CT numbers remain uncorrected, the altered x-ray CT numbers would result in portal designs with the wrong ion penetration depths in the patient. The most accurate method is to perform two x-ray CT scans, the first one without contrast and the second one—performed immediately after the first one to minimize motion—performed with contrast. Unfortunately, this increases the whole body radiation dose to the patient. As an alternative, if the RLTSPs of the tissues are well known, then the volumes containing the contrast can be contoured and RLSTP values assigned to those volumes. The x-ray CT number for brain tissue is generally well known, and thus the added uncertainty due to assigning an RLSTP should be fairly small. This may not be the case for lymph nodes, however, so for these areas the use of only non-contrast scans is recommended. Sometimes contrast is permanently infused into implanted materials—such as drainage tubes, artificial bones, or embolization glue—for the purpose of visualization. In these cases, an x-ray CT scan without contrast is not possible, so only the RLSTP substitution method is possible.

7.3 Dual-energy Kilovoltage X-ray Computed Tomography

As stated in section 5.6.3, the use of x-ray CT scans at two or more energies to better characterize the tissue was first performed in the 1970s but seldom used (Hounsfield, 1973; Rutherford, 1976; Gennant and Boyd, 1977; Millner et al., 1979). As of 2015, this was still not being done clinically for light ion teletherapy, but recent studies have indicated that dual-energy kilovoltage x-ray CT can enable quantitative material decomposition (i.e., determine the elemental composition and mass density) which, when combined with Monte Carlo calculations, could lead to a reduction in RLSTP uncertainty in some (but not all) situations. A study by Hünemohr et al. (2014) concluded that the component of uncertainty for converting x-ray CT numbers to RLSTPs could be reduced using dual-energy kilovoltage x-ray CT to 0.6% for soft tissue surrogates, 2% for polymers, and 10.8% for titanium. When high-atomic-number implants like prostheses are present, however, the strong attenuation of high- and low-energy photons used in dual-energy kilovoltage x-ray CT can still lead to artifacts in reconstructed images. The uncertainty of RLSTP from dual-energy kilovoltage x-ray CT in the presence of metal artifacts is currently not known. There is limited experience using dual-energy kilovoltage x-ray CT for light ion beam planning, so there are no conclusive uncertainty values associated with the conversion from scaled dual-energy kilovoltage x-ray CT numbers to RLSTP.

7.4 Ion Computed Tomography

As of 2015, ion computed tomography was not being performed clinically, so the uncertainty associated with this method has not yet been evaluated.

7.5 Megavoltage X-ray Computed Tomography

Compared to kilovoltage x-ray computed tomography, megavoltage x-ray computed tomography can improve the accuracy of RLSTP determination not only for bone and implanted materials with high density and high atomic number, but also for other materials commonly encountered in radiation therapy, such as certain adipose tissues and plastics having densities near to that of water (Newhauser et al., 2008). Figure 20 shows an x-ray CT-number-to-RLSTP conversion curve determined using a megavoltage beam from three Tomotherapy® treatment units (Moyers et al., 2010). Currently, the principal disadvantage of megavoltage x-ray CT is its inferior spatial resolution and contrast resolution in soft tissues compared to kilovoltage x-ray CT. As of 2015, there was limited research and clinical experience using megavoltage x-ray CT images for light ion beam planning. Generally applicable estimates of the penetration uncertainties associated with megavoltage x-ray CT and hybrid kilovoltage/megavoltage x-ray CT imaging (see section 5.6.2) are, therefore, not available.

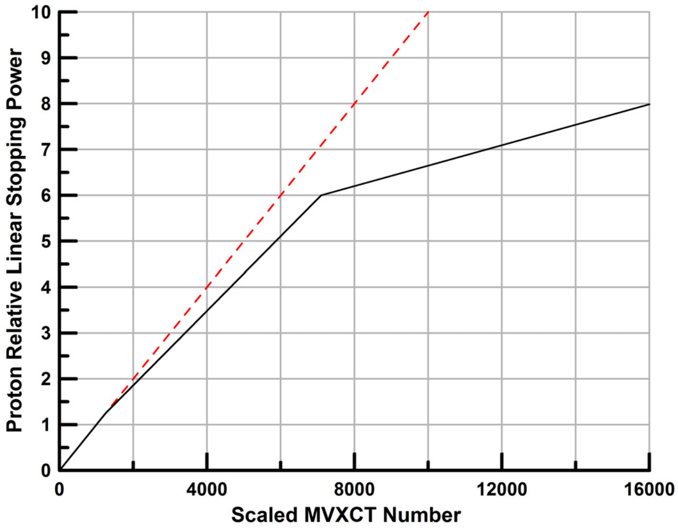

Figure 20. Conversion function for scaled megavoltage x-ray computed tomography (MVXCT) number to RLSTP. Solid tri-linear curve is optimized conversion function devised by Moyers et al. (2010). Dashed line represents a linear correlation between RLSTP and scaled MVXCT number to show deviation of conversion function from linearity. The abscissa is plotted in terms of scaled MVXCT numbers according to the procedure given in section 5.6.1.

7.6 Substituting RLSTPs

The use of bulk assignment of RLSTPs to regions of the patient or patient alignment devices for treatment planning has a long tradition, even after the advent of x-ray CT scanning. Its use in modern light ion radiotherapy is usually limited to those cases where there is large uncertainty in the x-ray CT numbers of the pixels within an x-ray CT image due to artifacts, injected contrast media, implanted materials, or alignment devices such as tabletops. In such cases, the overall uncertainty may be reduced by assigning measured or calculated RLSTPs—and relative linear scattering powers (RLSCPs)—to those regions where the x-ray CT numbers are questionable. Moyers et al. (2010) provided a list of expected x-ray CT numbers and RLSTPs for various implanted and alignment materials. This list may be used as a starting point for judging whether the assigned RLSTPs are reasonable, but each user should try to obtain the best values possible for their situation. Larger margins may need to be used when optimizing these types of plans due to the larger uncertainties.

Another use for substituting RLSTPs—and relative linear scattering powers (RLSCPs)—is for ensuring tumor coverage or OAR avoidance for time-varying penetration depths. Examples of this use include air in a water-filled rectal balloon, a patient gown pressing the patient's skin, gas in the intestines or other cavities, and the diaphragm moving in and out of the beam path. By substituting the highest RLSTP for any material that may be present before plan optimization, the uncertainty of covering the distal edge of the target may be reduced. Conversely, by substituting the lowest RLSTP for any material that may be present before plan optimization, the uncertainty for avoiding a distal OAR may be reduced. It can also uncover under-dosing of the proximal edge of the target.

7.7 Recommendations

- A separate conversion function should be generated for each set of CT scanner parameters (protocols) with different kVp, scan field-of-view size, and reconstruction kernel.

- Differences exist between plastic phantoms and real tissues. If a plastic phantom must be used to generate the conversion function, apply offsets to construct a real tissue function and evaluate the uncertainties accordingly.
- When regions of the CT image contain artifacts or contrast that must be contoured and assigned best-estimate RLSPs, the penetration uncertainty for beams passing through those regions should be increased.

8. Lateral Alignment Uncertainties (LAUs)

8.1 Introduction

Lateral alignment uncertainty (LAU) is defined as the combination of all factors that can result in transverse misalignment of the delivered beam relative to the intended target. A major difference between light ion beams and megavoltage x-ray beams is, however, that LAUs can have profound influences on the uncertainties of penetration of the ions. It is thus vitally important to understand the LAUs, not just with respect to lateral margins, but also with respect to penetration.

8.2 Targeting

8.2.1 X-ray CT Image Reconstruction Accuracy

The geometric accuracy of x-ray CT image acquisition and image reconstruction is critical to the accuracy of the treatment plan geometry as it affects the isocenter placement, beam angle selection, field-shaping device design, and beam range selection. The x-ray CT geometric accuracy should be thoroughly evaluated during the x-ray CT scanner acceptance testing, as well as being verified by periodic QA procedures. The AAPM TG-66 report (Mutic, et al., 2003) provides a detailed discussion of the QA requirements for x-ray CT scanners. The spatial accuracy of x-ray CT scan images is of heightened importance for light ion beam treatments, as any uncertainties in the patient geometry reconstructed from the x-ray CT images may translate linearly into beam penetration uncertainties (see section 5, Equation 14). For example, the geometry accuracy near the outer edge of the image reconstruction field of view (RFOV), especially for large-bore x-ray CT scanners having a bore diameter greater than 100 cm, must be carefully validated to ensure that it meets the ±1 mm tolerance given in the TG 66 report. Alternative mitigation measures—including limiting the maximum SFOV used for clinical applications or additional corrections in the beam lateral and distal margin selections—may be necessary in the event that the scanner is not able to meet this tolerance. When fiducial markers are used for target identification, the x-ray CT slice thickness should be minimized to reduce potential volume averaging errors in marker localization.

8.2.2 Target and Critical Organ Segmentation

Although this task group report is limited to physical uncertainties, it is worth mentioning that target and critical organ segmentation constitutes a significant component of the uncertainties encountered in radiation treatment planning. Weiss and Hess (2003) performed a review of publications concerning inter-observer variations in defining gross target volumes (GTVs) and clinical target volumes (CTVs) and concluded that inter-observer variability in GTV and CTV definitions is a major, and potentially the largest, contributor to geometric inaccuracy in radiotherapy. Such variability may be due to improper selection of imaging modality for target contouring, such as between x-ray CT and MRI images (up to 40% volume difference for prostate); use of contrast-enhanced images versus non-contrast-enhanced images (up to 8% volume difference for prostate), as well as observer training and experiences (up to 30% volume difference). Intra-observer variability was found to introduce approximately 5% variations in target volume definition. Li et al. (2009) reviewed target and normal structure delineation variations for three breast cancer patients drawn by nine physicians of a multi-institutional and multi-observer clinical trial on breast cancer radiotherapy. They found that some structure volumes intersected (overlapped) by as little as 10% and that the standard deviation for the volume of some structures was as high as 60%. Cooperative clinical trial groups, such as the Radiation Therapy Oncology Group (RTOG), has since published target and organ-contouring guidelines in the form of atlases in an attempt to minimize such inter- and intra-observer variations (Goodman et al., 2012; Gay et al., 2012; Ng et al., 2012; Fuller et al., 2011; Toita et al., 2010; Myerson et al., 2009). Yi et al. (2012) evaluated the reproducibility of the RTOG-endorsed brachial plexus contouring atlas for x-ray IMRT treatment of head and neck cancers in five patients and found that the atlas was successful in providing consistent guidelines for minimizing inter-observer variations in the volumes of brachial plexus contoured by three radiation oncologists.

8.2.3 TPS Contouring Model

The three-dimensional volumes of targets and organs at risk (OARs) of radiation therapy patients are generally calculated from contours manually drawn on two-dimensional planes by radiation therapy staff members. Occasionally, atlas-based tools are used to generate contours. Typically, the contours consist of a series of discrete points drawn on multiple parallel planes, but sometimes the contours are drawn on orthogonal or oblique planes. The reconstruction of 3D volumes from the 2D contours requires mathematical manipulations such as triangulation, interpolation, or extrapolation across all planes. Sparsely located contour points—either within a single plane or due to the use of larger image slice thicknesses or slice spacing—can be a source of additional uncertainty relative to the intended target. Such imaging and contouring methods should be optimized with consideration toward reducing this uncertainty, especially when organs of small, even minuscule volumes are to be segmented, such as the optic chiasm.

8.3 Planning

8.3.1 Accuracy of Non-dosimetric Parameters and Patient Reconstruction

A number of non-dosimetric parameters of a TPS may significantly impact the geometric accuracy of treatment beam alignment. These include the selection and display of the beam isocenter; calculation and display of digitally reconstructed radiographs (DRRs); calculation and display of field-defining apertures; and accuracy of the gantry and patient positioner model within the TPS, including coordinate systems and coordinate system origins, among others. Each of these parameters needs to be carefully validated as recommended by the AAPM TG 53 report (Fraass et al., 1998) as uncertainties in their values may translate linearly into errors of beam placement. In particular, DRRs are commonly used for light ion beam treatment patient alignment and target localization. Bony landmarks, contours of bony structures and organs visible on planar x-ray or x-ray CT images, or implanted fiducial markers are often used for calculating translational and rotational correction values of patient/target localization in comparison to orthogonal x-ray images of the patient. The accuracy of patient alignment is, therefore, limited by DRR reconstruction accuracy. The AAPM TG-53 report (Fraass et al., 1998) details the steps and parameters for verification of DRR reconstruction accuracy and should be reviewed during the acceptance testing of a TPS. The x-ray CT slice thickness used for scanning patients for light ion beam treatments will limit the spatial resolution of DRRs calculated from these images and should be selected to optimize DRR resolution while minimizing patient imaging exposures, as well as staying within the limits of the permitted number of x-ray CT slices in the treatment planning and patient localization systems.

8.3.2 Lateral Penumbra Estimation

Pencil-beam-based calculation algorithms are commonly used for simulations of light ion beam treatment dose distributions (Hong et al., 1996; Bortfeld et al., 1993; Szymanowski and Oelfke, 2002).

Newhauser et al. (2007) compared Monte Carlo calculations and a pencil-beam dose calculation and found that the 80% to 20% lateral penumbra agreed to within 1 mm in homogeneous water. In heterogeneous media, however, the pencil-beam algorithm tended to underestimate the lateral penumbra in several clinical scenarios by up to 1.5 mm compared to Monte Carlo calculations (Paganetti et al., 2008). The dose calculation grid size/resolution used for proton therapy dose calculation can introduce additional uncertainties, especially in the lateral penumbra region. Li et al. (2006) developed an analytical method for determining the maximum acceptable grid size for discrete dose calculations in proton therapy treatment plans. They found that maximum grid sizes from 0.4 mm to 6.8 mm were required for beam ranges of 20 mm to 300 mm to maintain dose calculation errors due to dose grid size effects to within 2%.

In clinical light ion beam treatment planning, aperture margins should be explicitly selected for each portal to accommodate the increase in lateral penumbra width with increasing penetration depth. In addition, inter- and intra-fraction setup errors and organ movements, as well as patient anatomical changes that occur throughout the course of treatment, may introduce significant variations of the WET near the field borders, for example in the treatment of lung cancer wherein a beam may pass through the heart tangentially before reaching the target. Heart motion, combined with breathing and patient setup rotational errors, may introduce WET variations of several centimeters near field borders, thereby affecting the penumbra width. Failure to take these penumbra width changes into consideration during treatment planning may lead to dose under-coverage of the target. Calculating the dose distribution on multiple breathing phases, as mentioned in chapter 10, can also help in estimating an effective lateral penumbra to be used for margins.

8.3.3 Isocenter Definition/Selection Relative to X-ray CT Images

The location of the isocenter relative to the x-ray CT image is defined using a TPS. Modern 3D TPSs typically allow input of the isocenter coordinate location at a resolution finer than a single x-ray CT image voxel; therefore they are able to achieve a theoretical resolution of the isocenter location coordinates to within 0.1 mm or better (Fraass et al., 1998). Although not strictly an uncertainty, if the TPS does not allow selection of the coordinates for the isocenter with sub-voxel resolution, the TPS user would be required to select a non-optimal isocenter location, i.e., the center of the voxel or one of the voxel vertices as defined by the TPS. This would introduce a systematic non-ideal offset in the location of the isocenter throughout the course of treatment.

8.3.4 Apertures and Collimators

8.3.4.1 Patient-specific

<u>Manufacturing Technique</u>

Patient-specific apertures are typically machined from brass or other suitable materials that can efficiently stop protons and are readily machinable. An alternative method is to cast the device into the desired shape from a suitable reusable material such as Lipowitz metal. Yet another method is to cut the material using an electrical discharge machine (EDM) wire cutter. For machined apertures, potential uncertainties that can affect the lateral field shape include tooling size and machine/milling accuracy if the TPS does not fully account for and model the properties of the physical tools that will be used to fabricate the aperture, in particular if the aperture shape is manually edited by the TPS user. Another potential uncertainty can be introduced if the machined aperture does not account for the beam divergence (e.g., is manufactured with parallel edges). The magnitude of this effect worsens for large off-axis distances. For cast apertures, a potential uncertainty is the accuracy of the formation of the aperture edge from the mold, as compared to the intended shape defined in the TPS. It is noted that the effect of beam divergence can be more readily included in the electrical discharge machine (EDM) or cast aperture manufacturing processes compared to machined apertures.

For milled apertures, corners cannot generally be sharper than the milling tool radius, which might be as large as 5 mm. A hot wire for cutting the foam mold for a cast Lipowitz metal aperture or an electrical discharge machine (EDM) wire for directly cutting a brass or Lipowitz metal aperture provides the ability to achieve smaller-radius corners compared to a CNC drilling tool. Regardless of the manufacturing process, limitations in the ability to recreate the planned aperture contour can be properly addressed as long as the corresponding TPS accounts for the aperture manufacturing tool size in the treatment plan model. As manually edited aperture contours defined during the planning process could have sharper corners than can be physically realized, the TPS should include tooling size information to prevent this from happening. Apertures milled on a CNC machine typically have better than 0.5 mm accuracy, although each patient aperture should be verified for accuracy to identify potential errors due to drilling tool wear or data transfer errors.

Divergence

Unlike the aperture edges produced by a wire foam cutter or electrical discharge machine (EDM), the beam divergence is typically not included in the edges of most machined apertures. Compared to when the beam divergence is taken into account, the lateral penumbra width may be different than when parallel cutting of the aperture edges is performed; therefore, the uncertainty associated with divergent or non-divergent apertures should be determined during the commissioning of the aperture system. Uncertainty of the penumbra width for different off-axis edge locations and finite aperture thickness has been reported by Slopsema et al. (2006).

Weight (See Also Beam Delivery Section 8.5 on Deflection)

The total weight of patient-specific apertures, with a typical density of about 9 g/cm^3, can be significant depending on the size of the treatment field and the required thickness needed to block the highest-energy ion beam. Depending on the design of the device supporting the aperture, the weight of the aperture can potentially produce small but varying amounts of deflection in the beam delivery system that can affect the accuracy of the beam delivery aiming point. The amount of deflection, although expected to be a fraction of a millimeter, could be a non-negligible factor for high-precision stereotactic treatments. The aperture mounting and locking mechanism within the applicator and the applicator mounting on the applicator carriage may also introduce aperture-positioning offsets. A method to reduce the uncertainty associated with deflections of apertures with different weights is to compare a radiographic image through the aperture with an outline of the aperture produced by the TPS. Depending on the design of the devices and the QA procedures, the uncertainties described above that are associated with the aperture may introduce an offset from the intended location of approximately 1 mm as projected to the isocenter.

8.3.4.2 Multi-leaf Collimators

Introduction

The first multi-leaf collimator (MLC) for photon teletherapy was described by Takahashi (1960), and later MLCs were developed for fast neutron and electron beams (Leavitt et al., 1989). There have also been several different designs of MLCs for ion beams (Kanai et al., 1983; Ludewigt et al., 1995). The most obvious purpose of an MLC is to form patient-specific aperture shapes, eliminating the need for machined or cast apertures. For radiosurgery, the leaf widths must be very narrow (Dartz et al., 2009). Another purpose of an MLC for ion beams is to perform energy and fluence modulation (EFM) by combining different MLC shapes with different beam energies. The Lawrence Berkeley Laboratory developed a fast-moving MLC for such a purpose which was applicable to both laterally scattered and scanned beams (Chu et al., 1993). Others have also proposed this method of EFM using MLCs (Kanai et al., 1983; Torikoshi et al., 2007). (Note that the number of energy steps required to cover a target using this method can be reduced by using a so-called *miniature* range modulator of 5 to 10 mm nominal range modulation width.) Yet a third purpose of an MLC is to reduce the size of a scanned beam spot, effectively increasing the degree of lateral fluence modulation, decreasing the lateral field penumbra width, or both (Bues et al., 2005; Moignier et al., 2015; Kang et al., 2018).

Although an MLC facilitates efficiency in patient treatment delivery through elimination of handling and storage of patient-specific apertures, the use of an MLC potentially introduces additional uncertainties that should be considered. For example, any physical parameter of the leaf edge or leaf divergence that is not accurately modeled in the TPS can introduce an uncertainty in the delivered dose distribution compared to the TPS plan. For instance, if the leaf collimators had a gap of 20 µm, then the leakage transmission might be less than 1% and the overall uncertainty in dose relatively low (Grusell and Montelius, 1994). In addition, the absolute accuracy of the positioning of the leaf or the rotation of the MLC will introduce an uncertainty in the boundary of the delivered treatment field. Whereas the uncertainties associated with a physical aperture may be more likely to be systematic, the dynamic nature of multiple moving leaves of an MLC increases the possibility of uncertainties that are both random and systematic. The magnitude of these uncertainties is a function of both the MLC design and the TPS model and should be evaluated together as a system.

Leaf Design Influence on Lateral Penumbra Model

MLC leaves should be thick enough to not only stop the primary light ion beam, but also reduce the neutron dose to an acceptable level. To minimize leakage, the University of Pennsylvania (UPenn) uses 9-cm-thick tungsten leaves with discrete steps on the sides of each leaf (see Figure 21). The MLC consists of 50 leaf pairs with a lateral width perpendicular to the light ion beam axis of 5 mm (Diffenderfer et al., 2011). The leaf sides are designed to match the beam divergence for the nominal virtual source-to-axis distance (VSAD). For practical reasons, the end of the leaf may not have a profile that changes with leaf position to match the beam divergence. As such, the lateral penumbra width associated with the end profile shape of the leaf may be different from the lateral penumbra width associated with the side of the leaf. In the UPenn MLC design, a difference in lateral penumbra width of approximately 1 mm has been observed between the leaf edges and sides. The design of the TPS algorithms should be evaluated to determine if possible differences in beam divergence (and the associated uncertainty) are accurately accounted for in the TPS penumbra calculation. If they are not, then either the dose calculation model must be improved or the applied margin may need to be altered.

Arguably, an MLC should rotate around the light ion beam central axis. If an MLC has this capability, then the lateral penumbra could be a function of the MLC rotation angle, and the TPS should

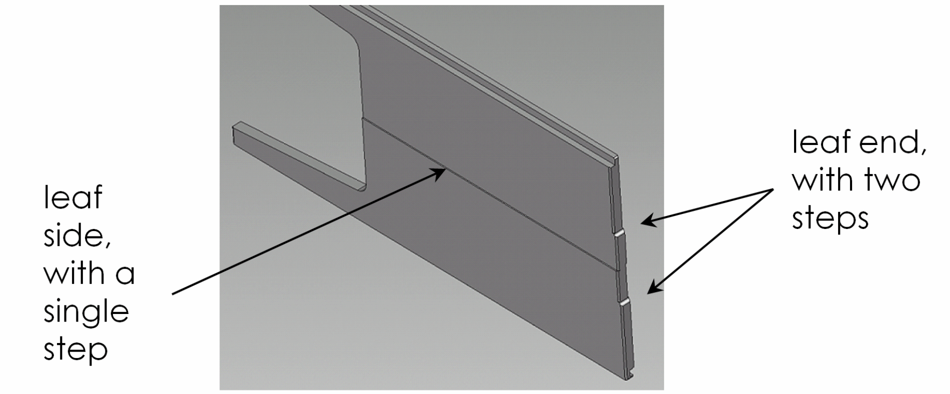

Figure 21. The leaf design of Proton MLC used at the University of Pennsylvania. Figure courtesy of Varian Medical Systems.

have the capability to take this dependence into account. If the TPS does not account for this dependence, a larger uncertainty value may need to be applied.

The discrete leaf width of a proton MLC system introduces a "stair-stepping" effect of the produced field shape and, subsequently, the isodose curves, particularly at shallow depths, which may not be modeled by the TPS. Furthermore, when the projected leaf width is greater than 5 mm, the discreteness of the TPS conversion of the field shape into MLC leaf positions may affect the agreement between the delivered and the TPS dose distributions. Thinner MLC leaves would reduce such uncertainties; the dosimetric effect of such uncertainties should be investigated for any new MLC system.

Leaf Position Accuracy

Since the position of the MLC leaves depends on the shape of the patient's fields, the accuracy and associated uncertainty of the leaf position should be considered in the analysis of the system's ability to define the accuracy of a treatment edge location. In addition, where the leaves are intended to be closed, the tolerance of leaf positioning should be at least smaller than the steps in the leaf end. Leaf ends have finer sub-millimeter positioning resolution than the 5-mm resolution of the leaf sides and, therefore, the leaf positioning accuracy should be considered within the context of penumbra uncertainty from the leaf design. For different leaf-to-patient gaps and phantom depths, the field size and penumbra should agree within approximately 1 mm to treatment planning values for all four MLC edges.

For the purpose of shaping a scanning beam spot, the MLC must move rapidly and achieve its prescribed position before the spot arrives. Non-repeatable dampening of the rapid motion of the MLC can lead to uncertainties of the beam spot shape and size and, therefore, the resultant dose distribution. Preliminary investigations suggest that by limiting the minimum offset distance between the trimmer blade and the projection of the spot aiming point to 1.5 mm, a robust plan can be created that suffers less than a 2% change in the prescribed target coverage (95% level of prescribed dose) when subjected to spot positioning, trimmer positioning, and mounting alignment errors of 1.0 mm, 0.5 mm, and 0.5 mm, respectively at the 2 SD level (Gelover et al., 2015).

Interaction with Gantry

In contrast to radiation heads with multiple applicators for different clinical applications, MLCs typically have only one large size and, therefore, require larger air gaps for some situations. In the UPenn MLC design, the outer shape of the MLC was designed so as to achieve air gaps similar to a 100-mm-radius beam applicator. This design incorporates an asymmetric outer contour so as to minimize the gap for head and neck applications. Translation of the MLC along the beam direction might cause a variation in the patient field if the translation is not parallel to the central axis. This movement should be controlled to within 1 mm and checked periodically. As with other beam applicators, the deflection and accuracy of the MLC should be determined at both the minimum and maximum extension locations, as well as at typical locations for different gantry angles. The distal edge of the UPenn MLC can be placed anywhere from 100 mm to 500 mm from the isocenter, with 300 mm being a typical extension. Gantry-angle and MLC extension-specific corrections to be used in the image guidance system can be defined to compensate for known beam deflections relative to the isocenter (Moyers, 2004). For example, at UPenn, eight gantry angles and three MLC extensions are used for interpolating the defining gantry angle, and MLC extension-specific corrections to the isocenter are used as part of image guidance. Although the total gantry isocenter diameter may be up to 5 mm, less than 1 mm of this was due to deflections of the beam applicator during extension.

8.4 Alignment

8.4.1 Inter- and Intra-fraction Patient Translation and Rotation

Light ion beam treatments have traditionally been performed using daily image guidance with orthogonal x-ray imaging. Inter-fraction errors, be they based on bony landmarks or implanted fiducials, can be estimated based on the landmark type, expected motion of the target, as well as the inherent accuracy of the image guidance algorithms. For example, a tolerance between the planned and imaged position (e.g., physical or virtual cross-wire) of 1 mm in translational daily setup errors may be used for nonmobile targets, while for a mobile target, such as the prostate localized using implanted fiducial markers, a tolerance of 2 mm may be appropriate. The determination of aperture margins from clinical target volumes (CTVs) or organs at risk (OARs) should, therefore, include consideration of these uncertainties.

Intra-fraction patient translation and rotation errors, herein defined as such errors that apply to the entire patient (instead of the target), may occur due to either patient motion or patient positioner motion between two or more portals of a single fraction. The accuracy of the patient positioner isocentric rotation and translation may introduce additional alignment errors if the patient is imaged and aligned at a combination of gantry and patient positioner locations that are different from the treatment position (without re-imaging). Note that the intra-fraction errors, as defined here, are limited to light ion beam treatment system mechanical tolerances, including gantry isocentricity and patient positioner translation and rotation accuracy, as well as the tolerance of the initial patient setup position using image guidance. Since light ion beam treatments are usually considered high-precision treatments, recommendations for SRS/SBRT can be applied. The AAPM report TG-142 (Klein et al., 2009) recommended that imaging accuracy be maintained to within 1 mm for SRS/SBRT-type treatments using either planar kV or cone-beam x-ray computed tomography imaging techniques, and that gantry and patient positioner motion accuracies be maintained to within 1 mm and 0.5 deg of their respective baseline values. Localization imaging performed between each treatment portal has the potential of reducing the required margins.

Rotational intra-fraction errors may be present due to gantry and patient positioner residual angle errors. Determination of the effect of intra-fractional errors is significantly dependent on the geometry of the treatment field and target shape: a target elongated in the direction of the beam axis will be more sensitive to rotational errors compared to a more spherical target due to potential under-coverage of portions of the target proximal/distal to the isocenter, therefore potentially requiring an additional lateral margin to accommodate. For example, for a portal with 100 mm of range modulation, a field diameter of 100 mm, and a VSAD of 2300 mm, a 1° gantry angle error would require slightly less than 1 mm additional lateral margin.

8.4.2 Non-rigid Body Deformation and Organ Filling

Targets that are in close vicinity to organs with potentially variable filling volumes are well known to move and deform. A prime example of this phenomenon is in the treatment of prostate, which can both move and deform due to changes in bladder filling and rectum contents, including rectal gases and fecal matter (Mak et al., 2012; Liu et al., 2012; and Velec et al., 2012). Such movements and target deformations can be especially severe for post-prostatectomy radiotherapy, as the bladder is at risk for tumor involvement and is thus included in the target (Fiorino et al., 2005). The location and geometry of other abdominal tumors may similarly be affected by varying stomach and bowel filling, especially if the x-ray CT scan and treatment delivery occur at different times of the day (Mahmood et al., 2012). While no general algorithms are available for estimating the magnitude of such motion and deformation, clinically they are managed by attempts to reproduce a certain organ filling, such as treatment of prostate tumors with rectal balloons filled to a constant volume and by having patients drink water immediately prior to their x-ray CT scan and treatments in order to achieve a full bladder.

For treatments of abdominal tumors, the patient may be requested to fast before each scan or treatment (Mahmood et al., 2012). Daily use of ultrasound scanners may also be used to verify a given bladder volume (Hynds et al., 2011). Periodic rescanning with x-ray CT or MRI may reveal if the applied uncertainties are sufficient or if replanning is necessary to achieve the desired prescription aims. The effect of organ filling and organ deformation needs to be carefully considered in light ion beam treatment planning, as it perturbs not only the target geometry, but also the beam range and range modulation. For example, beams that pass through organs with variable filling or large deformation should be avoided if possible. If avoidance is not possible, then larger distal and proximal margins should be used and plans recalculated with the organ content overridden with air and water to check the robustness of the plan.

8.4.3 Imaging Systems

Radiographic imaging is usually used to align the patient with light ion beam treatment equipment and, as such, the imaging equipment must be well-aligned with the light ion beam delivery axis to minimize uncertainty in patient alignment. Imaging may be performed using either pairs of 2D planar imaging (usually orthogonal) or 3D volumetric imaging.

8.4.3.1 kV Planar X-ray Imaging

Imaging X-ray Source Axis Congruency with Light Ion Beam Axis

An x-ray source is often used as a surrogate for the light ion beam through temporarily placing an x-ray source directly onto the beam delivery axis to create a "beams-eye-view" (BEV) projection. Alternatively, radiographic sources can be located off-axis to define a fixed geometry relative to the beam delivery axis. Regardless of the locations of the x-ray sources, any uncertainty in the location of the radiographic axis relative to the beam delivery axis will likely result in a systematic error in the location in the patient image and, therefore, in the patient alignment relative to the beam delivery axis. Uncertainty in the transverse location of the radiographic source relative to the central axis of the beam generates an uncertainty in the projection of the object, typically the patient's anatomy to be treated onto the imaging plane. The amount of uncertainty in patient alignment is related to the beamline geometry, including the radiographic source-to-axis distance (SAD), source-to-imager distance (SID), and source transverse location uncertainty. In general, the amount of allowable x-ray source transverse uncertainty is greater than the uncertainty it produces in patient alignment at isocenter due to demagnification associated with typical geometries used in light ion treatments (see Figure 22).

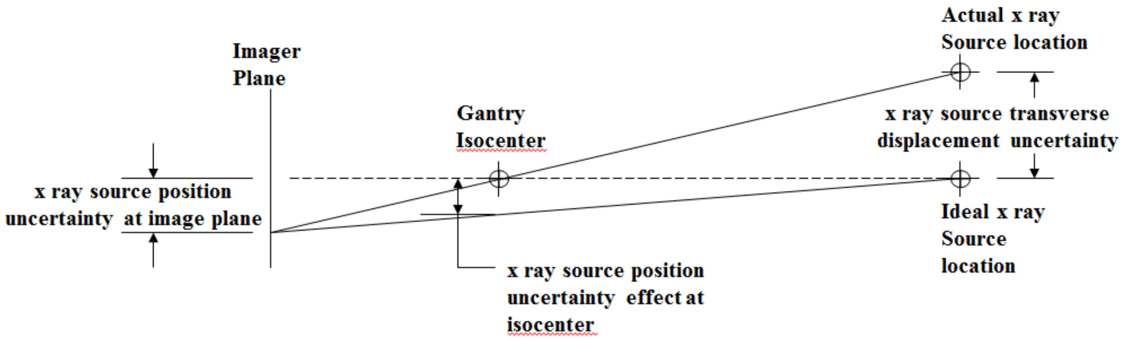

Figure 22. Effect of radiographic source transverse displacement uncertainty.

Imager Reference Axes (e.g., Cross-wire) Congruency with Light Ion Beam Axis

Imagers (both digital and film) are located behind the patient to capture the patient's position. In addition to capturing a projected image of the patient's anatomy, reference axes must be established to relate the image geometry to the beam delivery geometry. This may be achieved by mounting a radioopaque "cross-wire" in front of the imager (typically on the imager or on the beam applicator) such that a reference axis is established in the image along with the patient's image data. The cross-wire is typically aligned during installation, and periodic QA is performed to verify that the cross-wire is aligned to the central axis of the beam delivery system. Alternatively, a virtual cross-wire can be synthetically displayed based on a predetermined reference axis in the image data.

Depending on the system configuration, imagers can be mounted on movable or retractable mechanisms that are subject to variations in position of the imager and the reference physical or virtual cross-wire. Variations in the imager location (and the imager's reference axis) can occur, especially under the influence of gravity during gantry rotation. Variations in imager location can also occur depending on the mechanism for positioning the device, including settling into mechanical detents for manual motion, or electro-mechanical shifts if positioned by motor-driven mechanisms. Assuming the patient is aligned at a position using an imager that has an error in its reference axis (e.g., cross-wire), the amount of error or uncertainty in the reference image axes usually results in a direct error in patient alignment (after accounting for radiographic demagnification back to the isocenter).

It should be noted that systems that use a virtual cross-wire require additional considerations and care to understand their uncertainties, since these systems rely on *a priori* knowledge of the consistency and stability of the imaging equipment and, hence, the implied image reference axis. Furthermore, systems employing virtual cross-wires (or physical cross-wires) can potentially characterize deflections and errors associated with the imaging system and show the (virtual) cross-wire in a "corrected" location on the image. Systems employing such characterization methods to reduce uncertainty must be carefully analyzed to ensure that the assumptions applied for correcting the image reference axis are valid. Furthermore, these assumptions must be verified on a periodic basis to ensure the assumptions are valid between verification tests. Implicit in the above description of the congruency of the imager reference axis and light ion beam axis is that the imaging and treatment isocenters are congruent (see section 8.4.10).

Imaging System Magnification Factor

Digitally reconstructed radiographs (DRRs) are typically created during planning to establish the desired patient setup position to be replicated during treatment. To create these DRRs, the TPS uses a mathematical model of the imaging geometry of the treatment equipment, typically the imaging SAD and SID. Deviations or uncertainty in the actual position of the imaging source or the imaging panel location relative to the isocenter along the beam delivery axis will result in a different image magnification compared to what was used to generate the DRR. If anatomical features used for registration are distributed uniformly throughout the four quadrants of the radiographic image, this uncertainty effect at isocenter tends to be canceled. However, if anatomy in a particular quadrant of the image is predominantly used for image registration, magnification errors (either variations in the radiographic source location or in the imager) can result in a lateral alignment error (lateral uncertainty) at the isocenter, as shown in Figure 23.

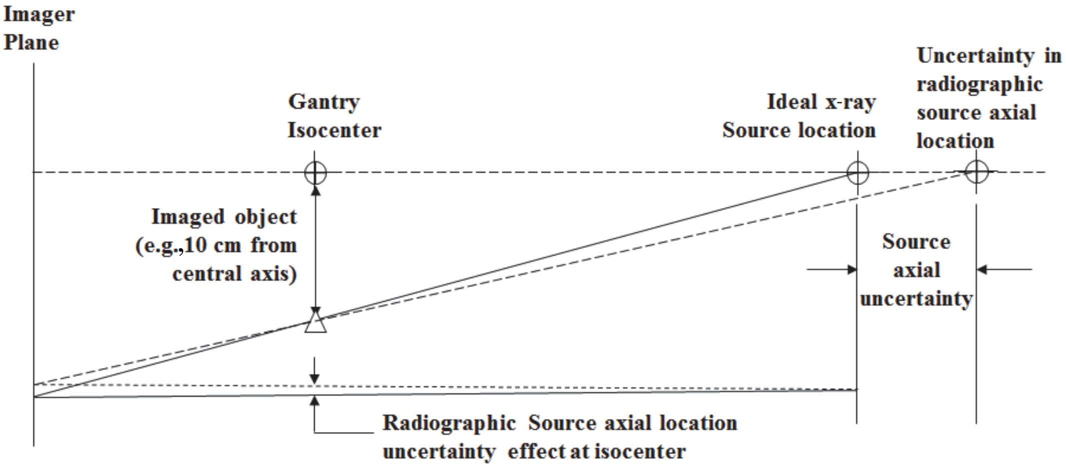

Figure 23. Effect of radiographic source longitudinal (axial) displacement uncertainty.

8.4.3.2 Integrated 3D Volumetric Imaging

While 3D volumetric imaging systems have been widely used in megavoltage x-ray beam delivery systems, they remain under development for light ion beam systems. AAPM TG-179 report (Bissonnette et al., 2012) provides detailed discussions of x-ray CT-based image guidance systems available for megavoltage x-ray beam delivery systems, including x-ray CT-on-rail, cone-beam x-ray computed tomography, and megavoltage x-ray CT. The report noted that agreement between the XCT isocenter and the treatment beam isocenter was typically better than 1 mm and recommended that a 2 mm tolerance be used for daily system QA tests. When volumetric imaging systems are implemented for light ion beam treatment delivery, careful attention must be given to such tolerance values and their application to lateral margins during treatment planning.

8.4.4 Delineation/Selection of Fiducials, Chamfers, Overlays, Etc. (on Reference DRRs and Setup Image)

Accuracy of patient alignment using orthogonal kV images is highly dependent on the accurate reproduction of alignment landmarks on reference images and daily kV x-ray images. The slice thickness of x-ray CT images used to create reference DRR images will generally limit the delineation accuracy of such landmark points to no better than one-half of the image slice thickness. Field margin calculations for light ion beam treatments should, therefore, make allowances for such uncertainties.

8.4.5 Patient Immobilization Variations

Daily patient immobilization reproducibility is generally considered in inter-fraction uncertainties. Its effect on lateral field margins for light ion treatments is, therefore, no different from image-guided x-ray-based radiotherapy procedures, although potential effects of such immobilization variations on beam ranges need to be carefully investigated.

8.4.6 Alignment Algorithm Accuracy

Calculation of patient setup or target localization corrections, from orthogonal kV x-ray images, may be based on 2D-2D matching of landmark points or chamfer (surface) features, or 2D-3D registration methods (Markelj et al., 2012). For calculation of translational corrections, Ploquin et al. (2008) compared three different imaging modalities (MV planar, kV planar, and cone-beam x-ray-computed tomography available with a linear accelerator and found agreement within 1 mm between 2D-2D and 3D-3D image registration algorithms. The general use of robotic patient positioning systems has allowed the application of 6 degrees-of-freedom corrections for patient treatments, thereby justifying the application of 2D-3D and 3D-3D image registration methods. In controlled phantom studies, these algorithms have been able to provide translational and rotational correction values with better than 1 mm and 1 degree accuracy for 2D-3D techniques (Fu and Kuduvalli, 2008) and better than 0.1 mm and 0.1° for 3D-3D techniques (Li et al., 2008). Note that these values are theoretical "best case" tests, with no influence of imaging technique variations, patient organ motion, or other factors that can degrade image quality and introduce imaging artifacts. The presence of these other factors in clinical patient images will introduce additional uncertainties in the accuracy of image registration and subsequent patient alignment and must, therefore, be considered carefully for each disease site.

8.4.7 Congruency of Light Field with Treatment Beam Field Edge

Some light ion beam equipment includes a light field to illuminate the intended light ion field. In cases where a light field is used for field matching—for example, in cranio-spinal treatments with the patient in a prone position—agreement of the optical light field and light ion beam field must be verified, similar to the QA expectations for megavoltage x-ray and electron beam therapy (Klein et al., 2009). For systems that have multiple beam applicators with a telescoping applicator carriage, this agreement should be verified for each beam applicator and for the entire range of travel of the applicator carriage. The divergence of the light field should be verified to agree with that of the light ion beam, especially when there are potentially significant differences between the virtual source-to-axis distances of the light field and the light ion beam. Tests should also be performed to determine at what applicator carriage extensions the light field is valid, as it has been reported that for some extensions part of the light field may be blocked. (Note that the summary of hypothetical lateral alignment uncertainties (LAUs) given in Table 2 below assumes patients are aligned with x-rays; it does not include uncertainties for light field and radiation field congruency.)

8.4.8 Patient Repositioning (Positioner Accuracy) to Implement Computed Correction

As a result of the image registration process, a correction is typically required to move the patient into proper alignment to match the setup DRR. Typically the amount of position correction is relatively small, e.g., less than 15 mm and less than 3° of rotation. The correction move is typically implemented by a patient positioner. Unless verification radiographic images are acquired immediately after the correction move, any error in the positioner's ability to implement the correction move can be a source of additional patient setup error. For the small translation distances described above, this error or uncertainty is on the order of a few tenths of a millimeter.

8.4.9 Imaging Versus Treatment Position Versus Secondary Targets

The uncertainties identified above relate to reestablishing the patient's position relative to a setup position typically defined by DRRs. Additional uncertainties, however, are introduced when the patient or gantry is moved from this imaging position to an alternate position used for the actual light ion beam delivery. For example, to achieve high-quality image registration, a patient may be aligned and registered at cardinal angles with a zero positioner yaw (patient axis aligned with the gantry rotation axis), however the actual light ion beam could be delivered at a different gantry angle or different positioner yaw angle or translational position. Similarly, additional uncertainty is introduced when moving to secondary treatment isocenters with a relative distance based on the DRR registration. Depending upon the specific treatment plan, imaging position, treatment position, and secondary imaging and registration, the additional uncertainties in the following sections may apply.

8.4.10 Gantry Isocenter

The gantry isocenter can be defined as a sphere of a specified radius that encloses all beam delivery aiming points as the gantry is rotated through its range of motion. The fact that the isocenter has a finite radius is indicative that the aiming point changes as a function of gantry angle and, therefore, represents a source of lateral alignment uncertainty (LAU) depending on the sequence of motions performed after the patient has been initially aligned. Factors that influence the size and shape of the isocenter include the physical type and design of the gantry structure, the amount of "walk" the gantry is allowed to move (also referred to as "corkscrew" motion along the axis of rotation) relative to the supporting building or structure, the type and design of the beam applicators and applicator carriage extension, and the influence of gravity. The diameter of an isocentric rotating gantry isocenter can range from 0.5 to 4 mm in diameter without software correction. The lateral uncertainty introduced by a non-zero (finite-sized) gantry isocenter may be an error that has both random and systematic components. Radiation head sag due to gravity may contribute a systematic error in the plane swept by the beam delivery axis during gantry rotation, whereas gantry corkscrewing and building interface points may result in a random or pseudo-random uncertainty in the direction along the axis of rotation that could include positional hysteresis based on the sequence of rotations leading up to a current gantry angle (Moyers and Lesyna, 2004). Such systematic beam pointing deviations due to the gantry characteristics can be measured and entered into a look-up table for corrections to be applied to the patient positioner at corresponding gantry angles (Moyers, 2004). The integrity of such a table should be verified each time repairs are performed on the gantry structure or attached components that may change the weight distribution of the gantry assembly.

8.4.11 Patient Positioner Isocenter

Patient positioners used in light ion beam therapy typically have the ability to perform motions, including the ability to mimic an isocentric rotation about a point (i.e., a yaw rotation about the vertical axis). Many patient positioners used in light ion teletherapy, especially those with rotating gantry-based systems, do not have a physical isocentric circular thrust bearing (as is often used in conventional radiotherapy) about which to rotate. Pseudo isocentric motions with these positioners are typically accomplished through a mathematical computation and subsequent movement of six or more degrees of freedom. The combination of uncertainties in each axis of the positioner will result in some error from the ideal isocentric motion. Similar to the gantry isocenter, a patient positioner isocenter sphere with a unique size and shape will be produced. Unless otherwise corrected by an external measurement system or other method, the non-zero patient positioner isocenter is a source of additional lateral uncertainty. The lateral uncertainty introduced by a non-zero positioner isocenter may be an error that has both random and systematic components. Patient positioner sag due to gravity may contribute a systematic uncertainty, whereas the positioning motors and sensors could introduce uncertainty that includes hysteresis based on the previous motion paths.

8.4.12 Patient Positioner Motion Absolute Accuracy

Similar to uncertainties associated with isocentric rotations, non-isocentric patient positioner motions, such as movements to secondary targets or patch portals, can introduce uncertainty based on the positioner's ability to implement relatively long distance movements. The type and magnitude of uncertainty in each axis (translation and rotation) is highly dependent on the design and architecture of the patient positioner. The uncertainty in position introduced by "long distance" motions within the positioner's workspace (absolute accuracy) should typically be less than ±1 mm for a well-designed positioner.

8.4.13 Congruence of Gantry and Positioner Isocenters

As described above, both the gantry and the patient positioner have non-zero-diameter isocenters that can result in lateral alignment uncertainty (LAU) during treatment. Another source of uncertainty is associated with the congruence of the gantry and positioner isocenters. Any misalignment of the centers of the two isocenter spheres will further exaggerate LAU during treatment. Typically, the radiographic imaging equipment (used as a surrogate for the beam delivery axis) is attached to the gantry. As such, any error in the patient positioner's isocenter alignment relative to the gantry isocenter will result in rotating the patient's anatomy around the wrong point and, therefore, create a possible lateral alignment error during beam delivery.

8.4.14 Coordinate System Alignment

For rotating gantries, the light ion beam axis sweeps through a vertical plane as the radiation head rotates around the gantry axis. This vertical plane is typically perpendicular to the gantry rotation axis. A second vertical plane can be defined as being perpendicular to the beam axis rotation plane and coincident with the gantry rotation axis, i.e., passing through the gantry isocenter sphere. The longitudinal axis of the positioner is generally defined as lying in this second vertical plane that passes through the center of the gantry isocenter "sphere." Additional LAU will be introduced due to misalignment of the patient positioner's coordinate system to the gantry coordinate system. This uncertainty and error is typically proportional to the movement distance, with the greatest errors for translations over long distances. This error can be minimized through careful design, alignment, and calibration during equipment installation. As discussed above, this type of error will only be realized under certain positioning movements. A misalignment of the coordinate systems between the positioner and gantry will likely result in a less-than-optimal gantry and positioner isocenter congruence.

8.5 Delivery

8.5.1 Beam Position Entering Radiation Head Relative to Beam Monitor

The position of the beam entering the radiation head for light ion beam treatments can have varying effects on the resulting treatment field, depending on the type of beam delivery system. For a beam delivery system that uses a contoured second scatterer, an error or uncertainty in the beam position will typically result in the beam impinging on the contoured scatterer in a manner that yields a non-uniform lateral dose distribution at the isocenter (see section 4.3.1). Typically, this type of error will be detected by downstream beam monitors and either be corrected or result in the beam delivery being terminated. The specific design of the scattering system will typically dictate the required beam entrance positioning accuracy to achieve reliable operation of the therapy equipment. In addition, a QA program should be designed to be in accordance with the capabilities of the beam monitoring system.

For beam delivery systems that use magnetically scanned beams (both uniform and modulated delivery modes), beam deflection is typically performed upstream of a more downstream beam position detector system. The observed beam position on the downstream detector can be used to adjust the amount of magnetic deflection needed to achieve some prescribed aiming point for the treatment field. A transverse error or uncertainty in the beam position at the entrance of the scanning system can, however, result in a position error at the isocenter plane, even with downstream position correction (see Figure 24 with an exaggerated geometry). This uncertainty applies when the scanned light ion beam is used to define the lateral edge of the field (e.g., when an aperture/block is not used). A downstream detector and position correction system can reduce some, but not all, of the effect of upstream beam position entrance errors. For scanning systems with downstream position correction systems, errors in beam position at the entrance to the scanning system should typically be kept small, on the order of 1 to 2 mm, such that with downstream position correction, the error in beam position at the patient plane can be reduced by a factor of typically 2 to 3, based on the geometry of the beam delivery system.

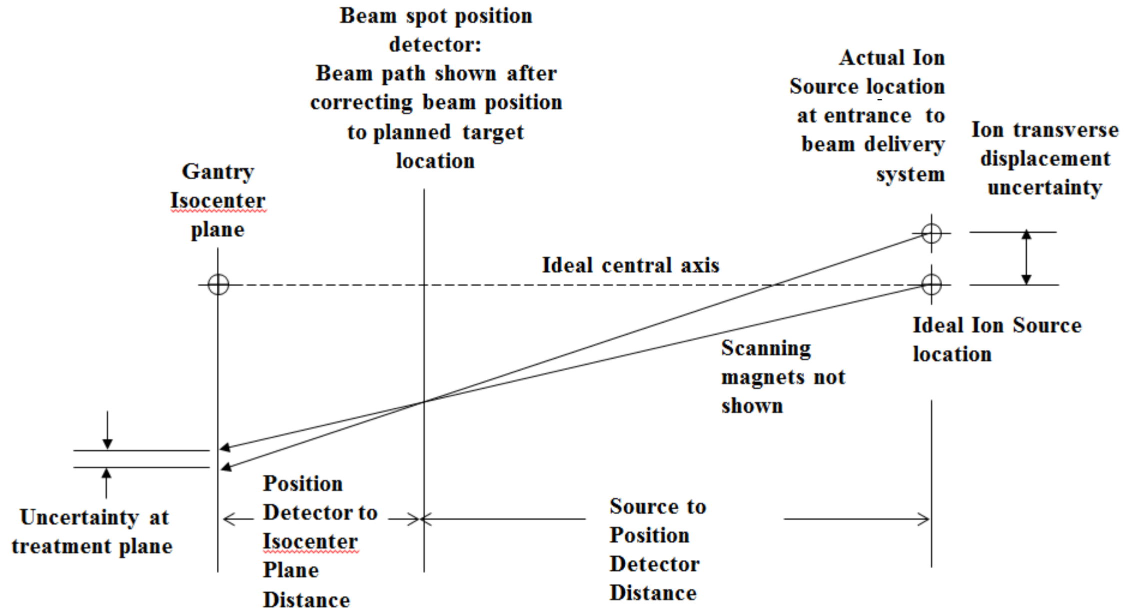

Figure 24. Effect of light ion source transverse displacement uncertainty (at upstream entrance to scanning magnets) on beam position accuracy at isocenter, assuming position feedback correction. Note that a similar diagram can be created showing the effect of ion beam entrance angle error and the resulting effect at isocenter. Typical scanning magnet and position detector locations will result in a geometry that will better suppress the downstream position error induced by an upstream angular error, as compared to the suppression of errors associated with upstream transverse beam displacements.

8.5.2 Beam Monitor Location Relative to Radiation Head Axis

For beam delivery systems that perform upstream beam position corrections, the measurement accuracy needs to be several times better than the required accuracy in order to make effective beam-steering corrections. The required accuracy of the device relative to the radiation head axis is highly dependent on the system design, and the effect should be included in the total uncertainty analysis for the specific design.

8.5.3 Virtual Source-to-axis Distance

Uncertainties in the light ion beam virtual source-to-axis distance (VSAD) can introduce an uncertainty in the projected treatment field size, in particular for treatments with beams with relatively large field sizes. The TPS will have a geometric model of the beam delivery system, including an estimate for the light ion beam VSAD. In addition, the TPS will specify an intended location of the physical aperture (if used) and, hence, the applicator carriage extension distance to achieve the required size and shape at the isocenter plane. An uncertainty of either the VSAD (actual compared to the VSAD modeled in the TPS) or a variation in the applicator carriage position (actual during treatment versus the value modeled in the TPS) along the beam delivery axis (when using an aperture) will result in a non-ideal magnification of the treatment field size. The uncertainty in the treatment field size due to an uncertainty in the VSAD (TPS vs. actual) increases as the treatment field size increases. An additional increase in the uncertainty in the projected treatment field size will occur with systems using movable applicator carriages due to the uncertainty (or allowed tolerance) in location of the applicator carriage (see also section 8.5.8). An example description of how to measure the VSAD can be found in Moyers and Vatnitsky (2012).

8.5.4 Gantry Angle

Variations or uncertainties in the gantry angle compared to the prescribed value will result in potential unintended dose to entrance tissue. This effect is largest for deep-seated targets in which the skin-to-isocenter distance is large. For a 300-mm-deep target with a goal of including no more than 0.5 mm of unintended tissue lateral to the beam, the uncertainty in gantry angle should be kept within 0.1 degrees relative to the prescribed value. A larger gantry angle uncertainty could be tolerated for isocenters placed at shallower depths. Equation 16 could be used to estimate the required gantry angle accuracy based on an assumed allowable lateral skin dose margin uncertainty allocation and skin-to-isocenter distance:

$$\text{gantry angle accuracy} = \arctan\,(\text{lateral dose margin} / \text{skin-to-isocenter distance}) \qquad \text{(Eq. 16)}$$

8.5.5 Gantry and Radiation Head Sag and Twisting Effects on Aperture Alignment

Unless the precise position of the field-defining aperture is known independently of the position as determined by the gantry angle and applicator carriage position, sag due to gravity will tend to displace the intended treatment field defined by the beam passing through the aperture. Depending upon the system design, this uncertainty may already be accounted for in the determination of the gantry isocenter specification. It should be noted, however, that patient-specific apertures may be of different masses and therefore produce different amounts of deflection than when measured by the tool used to determine the gantry isocenter size and shape. Uncertainty in the installed aperture lateral position due to sag or twisting of the radiation head for various size apertures should typically be kept to under ±0.5 mm. See "Interaction with Gantry" on p. 61 for a similar discussion regarding the effect of MLC weight and interaction with the gantry.

8.5.6 Applicator Carriage Skewness Effect on Aperture Location

An applicator carriage that extends toward and retracts away from the isocenter can be used to position patient-specific beam-shaping devices at distances to match the prescribed values from the TPS, typically to minimize the gap between the devices and the patient's skin. Depending upon the system design, this applicator carriage may have guides and drive motors that could produce slight relative shifts in position (skew) that result in deflecting the patient-specific devices from their ideal positions. The effect of motion skew, if present, should ideally be corrected to minimize its effect. Any residual skew and the impact it has on the locations of the devices should be included in the uncertainty analysis. This uncertainty effect may also apply to MLCs, depending on the particular design.

8.5.7 Applicator Carriage Sag Effect on Aperture Location

This uncertainty is similar to that described in section 8.5.5, except this uncertainty is a possible addition to the effect from the radiation head sag/twist that arises from the weight of the applicator carriage. This uncertainty may add linearly instead of quadratically to the uncertainty in the radiation head sag because gravity acts in the same direction.

8.5.8 Applicator Carriage Extension (Distance Along Beam Axis) Effect on Aperture Location

An uncertainty in the projected field size will occur when the aperture position defined in the treatment plan is different from the position used for treatment. See also section 8.5.3 above for a discussion of how an uncertainty or error in the applicator carriage extension distance can contribute to a treatment field size error compared to a planned field size. An acceptable applicator carriage position tolerance should be specified in the treatment planning prescription tolerance table. For large fields, with typical VSADs and typical aperture locations relative to the isocenter, the change in field size at the isocenter plane can be larger than 15% of the difference in distance of the aperture location compared to the prescribed location. For example, a 10 mm change in aperture location along the beam delivery axis for a typical light ion beam therapy configuration can result in a 1 mm change in field diameter for a 200-mm-diameter field size. Similarly, this uncertainty will apply to systems with MLCs capable of motion along the beam delivery axis.

8.5.9 Beam Applicator Installation onto the Applicator Carriage

A beam applicator containing an aperture, 2DRS, uniform range shifter (URS), or range modulator is typically mounted to an applicator carriage that is itself mounted to the radiation head. Depending on the system design, the mechanical tolerances and clearances that allow interchanging of these beam applicators may result in non-reproducible positioning after the beam applicator is installed. This non-reproducible positioning is another source of lateral alignment uncertainty (LAU), especially under the influence of gantry rotation and gravity. This uncertainty should be minimized and, if not fully eliminated by system design, the uncertainty should typically be designed to be less than 0.25 mm.

8.5.10 Aperture Position and Installation into Beam Applicator

The patient-specific aperture is generally installed into a beam applicator that is mounted to an applicator carriage. Another potential source of position uncertainty is with respect to the alignment of the patient-specific device relative to the beam applicator. This uncertainty includes both translational and rotational effects. Although this uncertainty should be small by good system design (e.g., ±0.25 mm, $\pm 0.25^{\circ}$), the residual uncertainty should be included in the overall uncertainty assessment.

8.6 Total Lateral Alignment Uncertainty (LAU)

Each facility, and sometimes different equipment and different techniques at one facility, may have different lateral alignment uncertainties (LAUs). As an example, Table 2 summarizes estimated LAUs for two anatomical sites. Each facility should determine the uncertainties for their specific equipment and procedures, either by component analysis or end-to-end testing, and enter the total values into the TPS for margining purposes (see section 9).

8.7 Recommendations

- The user should attempt to identify for their installed equipment, software, and processes as many individual LAUs as possible and quantify the magnitude of each.
- The individual component uncertainties should be added together in the appropriate manner and compared with an uncertainty value obtained from end-to-end testing.
- Different LAU values are often required for different situations.

Table 2: Estimated lateral alignment uncertainties (2 SD) for a hypothetical beam delivery system using scatterers and collimators. Examples are provided for tumors in the head and neck region and the abdominal region. The table assumes that the localization (setup) position and the treatment position are identical. Performing the localization at a position other than the treatment position would result in a slightly larger total uncertainty. The total uncertainty was calculated by adding all type A and B uncertainties, as identified by type in the second column, in quadrature although, as described in the text, some uncertainties in some situations should actually be added linearly (see section 2 and its references for a discussion about propagation of uncertainties). Table modified from Moyers and Vatnitsky (2012).

#	U	Item	H & N Uncertainty (mm)	Abdominal Uncertainty (mm)
T1	B	x-ray CT image reconstruction accuracy	0.45	0.45
T2	B	target and critical organ segmentation (physician drawing)	variable*	variable*
T3	B	TPS contouring model	1.0	1.0
P1	B	penumbra model	0.5	0.5
P2	B	isocenter relative to x-ray CT image	0.5	0.5
P3	B	aperture design	0.5	0.5
P4	B	DRR generation accuracy	0.5	0.5
A1	A	intra-fraction patient translation (breath hold plus gating)	0.5	1.5
A2	A	intra-fraction patient rotation (breath hold plus gating)	0.2	0.6
A3	A	non-rigid deformation and organ filling	0.5	2.0
A4	A	x-ray source axis congruency with ion beam axis	0.26	0.26
A5	B	imager cross-wire congruency with ion beam axis	0.75	0.75
A6	B	image magnification factor	0.24	0.24
A7	B	delineation of fiducials, chamfers, overlays, etc.	0.47	0.47
A8	B	alignment algorithm accuracy	0.5	0.5
A9	A	patient repositioning (positioner accuracy)	0.35	0.35
D1	A	beam position entering radiation head relative to beam monitor	0.08	0.08
D2	B	beam monitor location relative to radiation head axis	0.05	0.05
D3	B	virtual source-to-axis distance (field size)	0.4	0.4
D4	A	gantry angle	0.14	0.43
D5	B	gantry/radiation head sag/twist effect on aperture location	0.7	0.7
D6	B	applicator carriage skewness effect on aperture location	0.1	0.1
D7	B	applicator carriage sag effect on aperture location	0.18	0.24
D8	B	applicator carriage extension effect on aperture location	0.45	0.90
D9	A	beam applicator installation onto applicator carriage	0.18	0.18
D10	B	beam applicator sag effect on aperture location	0.28	0.38
D11	B	aperture manufacturing	0.6	0.6
D12	A	aperture installation into beam applicator	0.25	0.25
		TOTAL (quadrature sum)	2.3	3.5

* ≡ not included in total; T ≡ targeting; P ≡ planning A ≡ alignment; D ≡ delivery; U ≡ uncertainty type

9. Uncertainties Due to Anatomical Variations

9.1 Introduction

In x-ray and neutron teletherapy, anatomical variations of the patient throughout the planning and treatment of a patient mainly pose a problem in aligning the target and organs at risk; changes in depth dose are minimal. Although alignment is also a concern with charged particle teletherapy (electrons or light ions), a bigger problem with anatomical variations is often a geometric miss due to changes in penetration. For some delivery techniques, dose differences due to interplay of the anatomical variation with a moving beam position can also be of concern. Interplay effects are particularly critical for hypofractionated treatments with energy-stacked beams where penetration differences are not blurred over many fractions (Li et al., 2014). Anatomical variations can present in several different manners. Several of these manners are presented in the following sub-sections, along with typical uncertainties.

9.2 Trending Inter-fractional Variations

The first type of anatomical variation is an inter-fractional change that shows a trend with time. A prominent example is tumor shrinkage or growth over a course of fractionated radiotherapy. The radiation oncologist should be cognizant of the expected rate of growth for different types of tumors and schedule repeat imaging procedures at appropriate intervals.

The patient's overall weight may increase or decrease over time due to physiological or emotional conditions. It is quite easy and quick for the therapist team to weigh the patient weekly to check for such changes and signal a need for replanning.

Yet another example is fluid buildup after surgery. Although shunts may be implanted to minimize pressure buildup due to this fluid, changes in the WED between the skin surface and the distal edge of the target may still occur quite rapidly, possibly at a rate as great as 2 mm per day. In such cases, the source-to-skin distance (SSD) should be monitored daily. Proper fitting of face masks should also be checked.

In all of the above examples, these changes may lead to changes in penetration depth and thus in the delivered dose distribution. If changes do occur, the validity of the plan can be checked by recalculating the dose distribution after applying appropriate changes. If the recalculated dose distribution is significantly different than the original, then the plan should be re-optimized or adapted using the new conditions.

9.3 Random Inter-fractional Variations

The second type of anatomical variation is also inter-fractional, but more random in nature. Assuming that the registration and immobilization devices are adequate to set up the patient reproducibly every day, this type of variation mostly represents variations in organ filling, organ location, or both.

In the head, the most common example is filling of the sinuses with mucus. Another example is the position of the tongue. When beams pass through the mouth, a method should be provided to immobilize the tongue and jaw.

For prostate treatments, the largest variation in the delivered dose distribution may be a result of different filling of the rectum and bladder from day to day. Many facilities, therefore, provide specific instructions to the patient for fluid intake and bowel preparation prior to each treatment session. A balloon is often also inserted into the rectum and filled with a specified volume of fluid each day to make both the alignment and WET match the plan (Moyers and Miller, 2003).

For other abdominal treatments—such as stomach, pancreas, and para-aortic lymph nodes—the position of the intestines and bowels and their contents can be quite variable. Movement of food, gas, and feces is difficult to control and, therefore, large margins are often used for targets and organs at risk (OARs). Abdominal compression and belly boards are sometimes used to control the position of the internal anatomy.

9.4 Random Intra-fractional Variations

Despite the use of the techniques described above, random variations can still occur while the patient is set up on the positioner for treatment. For example, one aspect of a fluid-filled balloon inserted into the rectal cavity is that it can restrict passage of gases that may cause a pressure buildup and discomfort to the patient during treatment. A very small diameter tube may be inserted with the balloon to allow such gas to pass. Peristalsis of the intestines is another movement that can occur during treatment.

9.5 Periodic Intra-fractional Variations

The most common intra-fractional changes that are periodic in nature are due to respiratory and cardiac motion. The largest-amplitude motions are near the diaphragm, and thus they affect the treatment of lung and liver tumors the most, but respiratory motion can affect tissue locations even at long distances away, such as at the prostate. Moyers and Vatnitsky (2012) have summarized various types of tissue motion and provided mitigation and planning techniques for respiratory motion. The most commonly used techniques to mitigate the effects of motion due to breathing are breath holding and beam gating, but apneic oxygenation is sometimes used. Motion tracking techniques have been proposed, but they have not yet been implemented with light ion beam treatments. Compression has been used for a few ion beam teletherapy cases, but users have often found that the devices used to do the compression interfere with the preferred ion beam path, and sometimes the device simply results in changing the motion from one location to another, but still within a beam path. Regardless of what mitigation technique is used, there will always be some residual motion that must be accounted for in the planning and delivery of the treatment. Generally, this residual motion is accounted for by expansion of the aperture hole and 2DRS cavity, or by rescanning the beam spot over the target. The uncertainties related to patient motion are thus the unknown deviations from the predicted motion.

9.5.1 Residual Motion during Breath-hold Procedures

The uncertainty in the reproducibility of the targets and normal tissues during breath-hold procedures can be considered to be the residual motion, and thus the margins to be applied are dependent upon how well the residual motion can be predicted.

In a study of deep inspiration breath-holding (DIBH) with megavoltage x-rays, Hanley et al. (1999) and Mah et al. (2000) found an intra-breath-hold variability of the position of the diaphragm and chest wall with mean sigma values of 1.0 and 0.6 mm, respectively, and an inter-breath-hold variability of 2.5 and 0.9 mm, respectively. Using both x-ray imaging of the diaphragm and coils implanted inside the liver, a study by Dawson et al. (2001) showed that the average intra-fraction motion was restricted to 2.5 mm and 2.3 mm. Remouchamps et al. (2003) used active breathing control (ABC) for left-sided breast cancer at moderate deep inspiration and portal imaging for studying the motion. They found that intra-fractional motion was generally less than 2 mm (1 SD). Another study using ABC was performed by Zhao et al. (2008), with the results showing an average intra-fraction position of the diaphragm of 1.6 mm. Breath-hold treatments at full inspiration combined with breathing of oxygen can increase the fractional time that the beam is on, thereby increasing the delivery efficiency (Bush unpublished, 2003; Romano et al., 2013; Parkes et al., 2016) and, possibly, reducing intra-fraction motion.

9.5.2 Residual Motion during Gating Procedures

The uncertainty in the reproducibility of the targets and normal tissues during gating procedures can be considered to be the residual motion, and thus the margins to be applied are dependent upon how well the residual motion can be predicted.

A main determinant of the residual motion during gating is the applied gating window. Results from a study by Tsunashima et al. (2004) demonstrated that if a 20% gating window was used at expiration, then the residual motion was less than 4 mm (1 SD) in one direction in the lower lobe of the lung, but less than 2 mm (1 SD) in all other directions and locations. Better separation of tumor and normal structures is, however, usually obtained by setting the gating window near full inspiration.

9.5.3 Residual Motion during Combined Breath-hold and Gating Procedures

It is also possible to combine multiple motion mitigation techniques. Wong et al. (2010) used an optical sensor to monitor the patient's surface and provide a gating signal to the accelerator in tandem with the use of an ABC device to control DIBH. For 14 lung cancer patients, they found intra-fractional movements of 0.2 ±0.2 mm, 0.3 ±0.1 mm, and 0.7 ±0.4 mm in the left/right, anterior/posterior, and cranial/caudal directions.

9.5.4 Residual Motion during Apneic Oxygenation Procedures

The procedure for performing apneic oxygenation has been briefly described by Moyers and Vatnitsky (2012). Residual motion using this technique has been investigated by Eckerman and colleagues in Munich using implanted fiducials. For patients with targets in the liver, the mean vector displacement of the fiducials was 0.9 mm, and for patients with targets in the lung, the displacement was less than 2 mm.

9.5.5 Interplay between Beam and Tissue Motion during Rescanning

Much research has been performed on the use of rescanning to mitigate the effects of motion relative to a scanning beam. There are several different forms of rescanning including, but not limited to: fast uniform scanning energy-by-energy; fast uniform scanning over the entire scan volume; scaled repainting with synchronized delay; and scaled repainting with a maximum dose per point. Few patients have actually been treated with these techniques, so there is little data to indicate the magnitude of the associated uncertainties.

9.6 Recommendations

- There are many methods available to mitigate the effects of anatomical variations. The residual variation after mitigation of the variation is quite variable; likewise the associated uncertainties are quite variable. These uncertainties must be individually assessed and the mitigation or planning process modified, if necessary, to minimize the uncertainties.

10. Optimizing Plans to Mitigate Uncertainties

10.1 Introduction

Due primarily to the known large dose gradients around light ion portals, but probably also because of the comfort with which nuclear physicists routinely deal with propagation of uncertainties, those involved in the early light ion treatment programs quickly developed methods for explicitly accounting for lateral alignment and penetration uncertainties in treatment planning. These methods were developed before the ICRU proposed the methods and nomenclature that have since become standard in megavoltage x-ray therapy that account only for lateral alignment uncertainties (LAUs) (ICRU, 1993b). Practitioners recently transitioning from x-ray to light ion beam treatments have typically found that an adjustment and learning process has been required. This section attempts to describe how to apply the uncertainties described in the previous sections to treatment planning.

A common mitigation technique for lateral and penetration uncertainties is to place margins around targets and normal tissues. Whereas in photon therapy a margin around the CTV to define a planning target volume (PTV) is often used to account for uncertainties, the techniques in light ion therapy are more diverse and include 2DRS expansion or contraction, careful choice of beam directions, alternating patch portal combinations, and robust optimization techniques.

10.2 Target and Organ-at-risk Considerations

The ICRU (1993) defined the gross tumor volume (GTV) as "the gross palpable or visible demonstrable extent and location of malignant growth. The GTV may consist of primary tumor, metastatic lymphadenopathy, or other metastases." Brahme (1984) concluded that the mean dose delivered to a tumor is most predictive of its response to radiation, with the caveats that any underdosed regions not have a large volume and that the dose within the underdosed regions not deviate significantly from the mean dose. Niemerko (1987) verified this conclusion using the equivalent uniform dose (EUD) model. According to these studies, a treatment plan should be designed such that (1) the prescribed dose equals the mean dose (approximated by the median dose (D_{50})) to the GTV, (2) the percentage of the GTV receiving greater than 95% of the prescribed dose, $V_{95\%}$, should be larger than 90% to ensure tumor cure, and (3) the percentage of the GTV receiving larger than 105% of the prescribed dose, $V_{105\%}$, should remain small to avoid treating intermixed normal tissues. Generally, the physician chooses to meet these dose-volume constraints each fraction of the treatment.

The ICRU (1993) also defined the clinical target volume (CTV) as "a tissue volume that contains a demonstrable GTV and/or subclinical microscopic malignant disease." Unlike the GTV, for which clinicians typically assume a constant tumor cell concentration at all locations within the volume, the concentration of tumor cells within a CTV can be quite variable. Most often, a CTV surrounds a GTV with a large tumor cell burden; however, between the outside border of the GTV and the periphery of the CTV, only sub-clinical disease exists. By definition, at the periphery of the CTV the concentration of tumor cells should be zero (ICRU, 1993). A long-held radiobiological principle is that less dose is required to sterilize tumor regions with smaller concentrations of tumor cells. With the concentration of tumor cells at the periphery being zero, the dose required to sterilize the tumor cells at the periphery of the CTV should also be zero. The dose constraints required for a GTV, for example the entire volume receiving a dose within ±5% of the prescribed dose/average dose, thus do not apply to a CTV. Unfortunately, the gradient of the concentration of tumor cells between the border of the GTV and the periphery of the CTV is rarely known, so an exact dose distribution is difficult to prescribe, but the dose required at the periphery of the CTV will certainly be less than near the center of the CTV or at the edge of the GTV (Brahme and Ågren, 1987).

The ICRU (1993) has defined an organ at risk (OAR) as normal tissue whose radiation sensitivity may significantly influence treatment planning, prescribed dose, or both. Unlike targets, physicians generally do not require the dose-volume constraints for OARs to be met each fraction of the treatment, but instead usually only for the entire course of treatment. Different portal arrangements may thus be used for different fractions.

One of the characteristics of light ion beams is that a portal from a single direction can usually provide good dose uniformity throughout a target, provided sufficient margins between the target and the lateral, distal, and proximal edges of the portal are provided. Multiple portal directions are sometimes used, however, to reduce the dose to OARs outside the target (or sometimes intermixed with the target). Unfortunately, the dose profiles are not step functions near the lateral, distal, and proximal edges of the portal designed to cover the target and to obtain the dose constraints described above; therefore, the edges of the portal, as defined by the 50% dose level, must be positioned at some distances outside the target or OAR, depending upon the prescribed priority. In traditional single scattered, double scattered, and uniform scanning proton beams, the lateral penumbra width between the 80% and 20% dose values (LP_{80-20}) and the distal penumbra width between the 80% and 20% dose values (DP_{80-20}) of a proton beam have large dose gradients, while the transition from 80% to 100% of

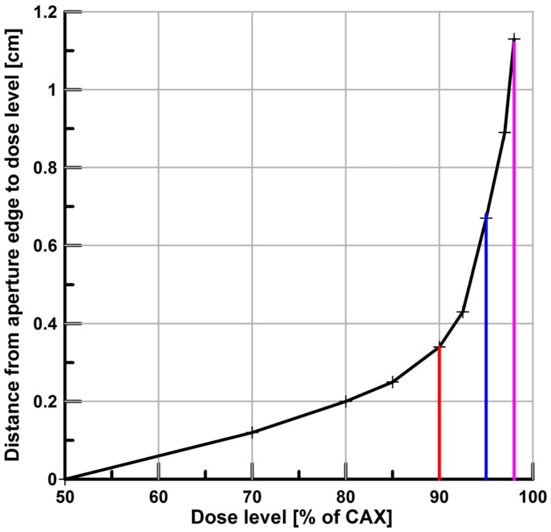

Figure 25. Example of lateral penumbra margin required for different target dose coverage levels. Vertical lines are used to aid the eye in discerning the distance from the field edge to the 90%, 95%, and 98% dose levels. Data from a double-scattered and collimated beam.

the dose is much more gradual. Figure 25 plots, for a typical proton beam, the distance from the projection of the aperture edge as a function of the delivered dose level normalized to the dose at the central axis where the dose per monitor unit is typically calibrated. The margin required around a target to obtain 90% of the prescribed dose at its edge is seen to be fairly small, but to obtain 95% of the prescribed dose requires double the 90–50% distance, and to obtain 98% of the prescribed dose requires three times the 90–50% distance. The amount of normal tissue irradiated outside of the target is thus a strong function of the minimum dose to be delivered to the target edge. To protect OARs and other normal tissues, the margin around the target should be kept as small as possible, consistent with the dose constraints given above.

10.3 Lateral Margins

In order to adequately cover the lateral extents of a target or protect OARs under most conditions, not just the nominal conditions, the uncertainties and residual motions described in the previous sections must be added to the lateral penumbral margin described in section 10.2. For placing margins by hand, the residual motion and lateral alignment uncertainties (LAUs) are often added in quadrature, and then this sum is added linearly to the lateral penumbra width. Some TPSs, however, may, in effect, add all three linearly due to the expansion algorithms used. Moyers and Vatnitsky (2012) have detailed some of these manual and computerized algorithms. Margins must be applied to both targets and OARs and, when they overlap, the clinician must decide which is more important. Another issue to be decided by the clinician is what level of uncertainty should be applied. Goitein (1982, 1985) advocated a k_p level of 1.5 SD for most cases. Other investigators in megavoltage x-ray therapy have advocated other k_p levels, and some have suggested that different k_p levels be applied to the random and systematic uncertainties for determining the margins (see, for example, van Herk et al., 2000). Although in light ion beam treatments it has generally been accepted that the systematic uncertainties are more important than random uncertainties, it has been most common for all uncertainties to be added together in quadrature and used as a single value.

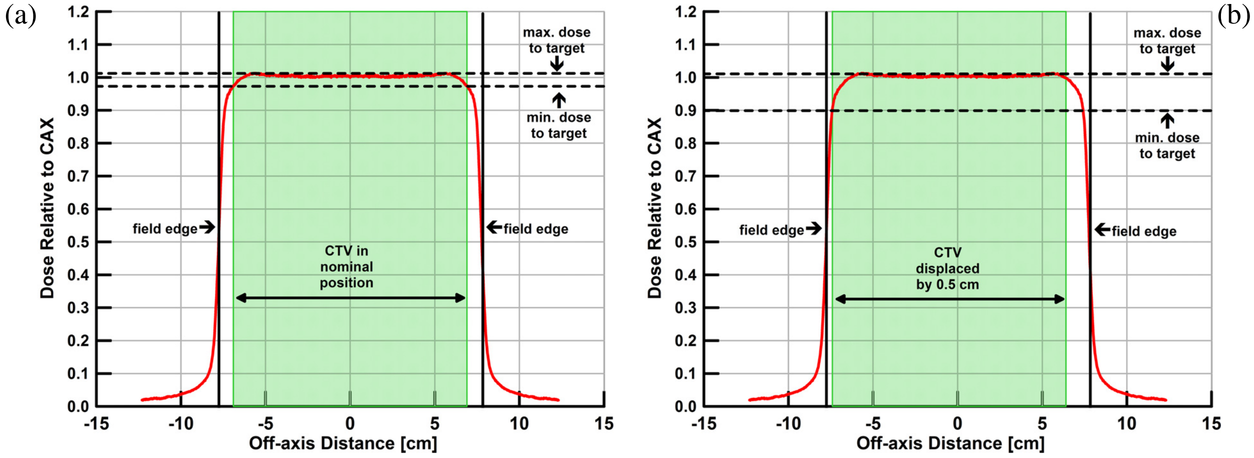

Figure 26. (a) Target in nominal position with respect to field. (b) Target displaced by 0.5 cm with respect to field. The average dose across the target is the same for both cases. Figure from Moyers and Vatnitsky (2012) and used with permission from Medical Physics Publishing.

Historically, the practical standard for light ion beams was to design the portal margins such that 100% of the volume of each CTV received greater than 90% of the dose prescribed to the CTV (and contained GTV) while accounting for uncertainties at the prescribed k_p level, assuming there were no OARs that impinged into the CTV. Figure 26(a) shows a CTV in its nominal position, centered with respect to a typical lateral dose distribution produced by a proton beam. Figure 26(b) shows the CTV displaced by 0.5 cm. When the CTV is at its nominal position, the minimum dose to the CTV is 97% of the prescribed dose, the maximum dose is 102% of the prescribed dose, and the average dose across the CTV is 100%. When the CTV is displaced by 0.5 cm, the minimum dose to the CTV at a point drops to 90% of the prescribed dose, the maximum dose remains at 102% of the prescribed dose, and the average dose across the CTV remains at 100%. The average dose is essentially unchanged by the displacement because, although the extreme left side of the CTV moves into a region of the beam with lower dose, the extreme right side of the CTV moves into a region of the beam with higher dose. The fraction of CTV that moves to a lower dose is very small, and it remains at a dose level greater than or equal to 90% of the prescribed dose. Due to the shape of the lateral penumbra and GTV-to-CTV margin, the minimum dose to a displaced GTV contained within the displaced CTV typically receives greater than 97% of the prescribed dose, thereby satisfying the dose constraints given above for a GTV. One might consider that for a CTV, where the dose required at the edge can be much less than at the center of the contained GTV due to decreased tumor cell concentration, the required dose at the edge of the displaced volume could be reduced to less than 90%, thereby decreasing the required portal margin. On the other hand, decreasing the minimum dose value to less than 80% would provide little gain in decreased normal tissue volume due to the steep gradient in dose with distance (see curve in Figure 25). For consistency in planning, the 90% value has typically been used for CTVs.

Figure 27 shows an alternate two-dimensional method for looking at the dose coverage of targets. In the drawing at the left, a GTV shown in yellow and a surrounding CTV shown in red are aligned nominally in the center of the field for a portal. The entire CTV is covered by a dose greater than about 97% of the prescription dose. In the drawing at the right, the GTV and CTV are aligned off-nominally such that the left edge of the CTV is receiving only 90% of the prescribed dose and the left edge of the GTV is receiving 95% of the prescribed dose. The top, bottom, and right sides of the CTV, however, are still receiving greater than 95% of the dose, and those same sides of the GTV are receiv-

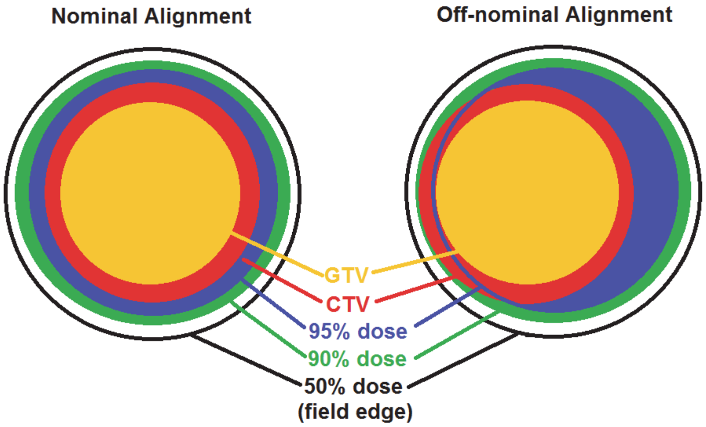

Figure 27. Illustration of target coverage by dose distribution when in nominal alignment (left) and off-nominal alignment (right). See text for description.

ing greater than 97% of the dose. Although targets are generally not rigid objects like the circles in the figures, the equipment involved in miss-alignments of imaging and treatment beams are rigid, and the figure is useful for demonstrating that the average dose delivered to a target does not change much for off-nominal alignments (assuming dose modulation within the target is small). Note that the same arguments can apply for depth dose distribution coverage, particularly near the distal edge.

At least one commercially available TPS allows the input of six residual motion parameters (superior, inferior, anterior, posterior, left, right) for moving structures. For targets, this residual motion is automatically applied in portal design by directionally expanding the apertures, while for OARs the apertures are automatically contracted. This expansion or contraction is added or subtracted linearly according to the input alignment uncertainty and penumbra, so it may over-compensate for the effect of motion. The user is free, however, to input whatever residual motion values they feel are appropriate.

Adoption of 4-D CT scans into TPSs that support light ion beam planning has been slow in the commercial market, so most users have analyzed motion using independent programs and then sent to the TPS a single image set with which to design the portals. In cases where target coverage or OAR avoidance is questionable, other image phase sets have been imported and the dose distribution recalculated based on these image sets.

10.4 Proximal and Distal Margins

The process of applying distal and proximal margins uses the same concept of adding uncertainties as for lateral margins, but instead of spatial distances, it makes use of water-equivalent thicknesses. By strict interpretation, this means that a different margin should be applied to the proximal and distal sides of the target along each ray line emanating from the light ion beam source. This makes it almost impossible for the human planner to draw an appropriate margin. Instead, this task is usually delegated to the computerized TPS that can draw a field target volume (FTV) in a water-equivalent space specific for each portal direction (Moyers and Vatnitsky, 2012). What makes the portal design particularly difficult is that lateral alignment uncertainties (LAUs) and residual motion affect the alignment of the designed penetration distribution with the patient. If the portal delivery technique uses 2DRSs, inclusion of the effects of the LAUs and residual motion can be performed by cavity expansion for target coverage or cavity contraction for protection of OARs distal to the target (Curtin-Savard et al., 1999). If 2DRSs are not used to produce the penetration distribution, but instead narrow scanning beams are used, then an equivalent function can be performed by increasing or decreasing the energy and number of energy levels of beams along adjacent ray lines as described by Moyers and Vatnitsky (2012). The selection of the number of energy levels and weighting factors needs to consider not only the penetration to the distal side of the target, but also the penetration to the proximal side; in other words, the range modulation along each fan line.

At least two commercial TPSs allow the input of two separate margins for both distal and proximal penetration uncertainties. The first is due to the penetration uncertainties due to beam delivery (PUBD) discussed in section 2. This value is typically given in millimeters of water and usually represents the quadrature sum of values, as shown in Table 1. The second is due to the penetration uncertainties due to physical characterization (PUPC), as discussed in sections 5, 6, and 7. Different investigators determine the composite value for the penetration uncertainties due to physical characterization (PUPC) using different analysis schemes, but the value is typically given as a percentage of the water-equivalent depth (WED) into the patient, including the WED of any registration or immobilization devices through which the beam passes. Using one analysis scheme, Table 3 summarizes the component parts of the penetration uncertainties due to physical characterization (PUPC) for a typical facility for three conditions: before mitigation of uncertainties, with typical mitigations, and with mitigations expected in the future. Not included in the table are uncertainties due to ion straggling through heterogeneities. This uncertainty can be quite variable from portal to portal, and the robustness techniques described below are used to mitigate them. In addition to the type of analysis scheme used, values for the PUBD and PUPC can vary from facility to facility based upon equipment design, planning techniques, QA procedures, levels of perceived risk, and other factors. Yang et al. (2012) performed an evaluation of penetration uncertainties for several different treatment sites and found for prostate, lung, and head and neck values of 3.0, 3.4, and 3.0% at the 2 k_p level, respectively. Paganetti (2012) also presented a study of penetration uncertainties, paying particular attention to the effect of heterogeneity straggling and the use of Monte Carlo. He found values of 2.7% without heterogeneities and 4.6% with heterogeneities at the 1 k_p level for standard calculation methods such as water-based pencil-beam algorithms. In these calculations, however, the uncertainty component due to conversion from x-ray CT number to RLSTP was chosen to be only ±0.5% (1.5 k_p) instead of the approximately ±2.9% (2 k_p) value found by Moyers (2014). When using a Monte Carlo calculation method, the uncertainties calculated by Paganetti decreased to 2.4% at the 1 k_p level for both cases; i.e., independent of the presence of heterogeneities.

Table 3: Summary of estimated penetration uncertainties due to the physical characterization (PUPC) of the patient and the alignment devices. Values given at the 2 k_p level. [Adapted from Moyers et al. (2010) but values changed to accommodate the larger water equivalence (WEQ) vs. RLSTP values found during the RPC site visits (Moyers, 2014).]

Cause	Uncertainty before Mitigation	Mitigation	Uncertainty after Mitigation	Possible Future Uncertainty
scanner calibration for standard conditions	±0.3% day-to-day	patient-specific scaling	±0.0%	±0.0%
kVp, filter, and FOV selection	±2.0% PMMA, PC >±2.0% bone	use only calibrated conditions	±0.0%	±0.0%
volume and configuration scanned	±2.5%	patient-specific scaling	±0.0%	±0.0%
position in scan	±1.5% water* ±2.5% tissue >±3.0% bone*	–	±1.5% water* ±2.5% tissue >±3.0% bone*	±0.5% water^{DE}* ±0.8% tissue^{DE} >±1.0% bone^{DE}*
metal implants	100%*	z ≤ 22 - MVXCT z > 22 - substitution	±5.0% metal*	±5.0% metal*
stopping power of water	±1.0%	–	±1.0%	±0.5%
RLSTP of tissues and devices	±0.0 to 3.0%	contour and substitute	±1.0%	±1.0%
WEQ vs RLSTP (soft tissues only)	±2.9%	–	±2.9%	±1.6%
energy dependence of RLSTP for low Z	±1.2%	–	±1.2%	±0.5%^{MC}
TOTAL (soft tissues only)	±5.3%	–	±4.3%	±2.2%

* ≡ not considered in total, DE ≡ dual energy XCT, MVXCT ≡ megavoltage x-ray CT, MC ≡ Monte Carlo calculations, z ≡ atomic number

If a facility does not have a TPS with the capability of allowing entry of the penetration uncertainties due to beam delivery (PUBD) and penetration uncertainties due to physical characterization (PUPC) and automatically generating a field target volume (FTV), then the user will have to draw a PTV around the CTV. Unfortunately, most drawing tools allow this to be done only in physical space rather than water-equivalent space and, therefore, the margins may not be optimized. Preferably a PTV will be drawn specifically for each portal, because the margins can be different for different portal directions and patient heterogeneities. This procedure, however, requires a substantial effort, so if the irradiated volume is fairly homogeneous and the range is similar from different directions, a single PTV is often drawn. Some facilities have exported the plan and patient information to an external program that draws portal-specific PTVs, and then the PTVs are imported back into the TPS for portal design (Park et al., 2012; Lin et al., 2015). This procedure works fairly well for single portal optimization (SPO) techniques, but difficulties are encountered when using multiple portal optimization (MPO) techniques. In MPO treatments using energy and fluence modulation (EFM) (IEC, 2017), particularly with the modulated scanning delivery technique, the aiming point MU weights of all incident portals are optimized simultaneously, and only the superposition of the dose from all portals yields the desired dose distribution. MPO treatments are, therefore, prone to dose uncertainties resulting from the misalignment of dose contributions from individual highly modulated portals (see section 11.1). This problem cannot be fully addressed by a PTV approach in planning and requires mathematical robust optimization techniques, such as described in section 10.7. Use of a PTV can, however, reduce the risk of underdosing at the edge of the CTV. By the nature of MPO planning, all portals are optimized simultaneously based on a single PTV, and thus the planner cannot define portal-specific PTVs like in SPO treatments. Depending upon the TPS, however, the planner may have the opportunity to define portal-specific volumes for the selection of energies and lateral spot positions. For example, the planner can manually avoid beamlets that stop in front of critical structures (Lomax, 2001) and thereby influence the robustness of treatment plans.

As discussed above, at least one TPS allows the input of residual motion parameters. During portal design this residual motion can be automatically applied for expanding the 2DRS cavity (or adding spots with higher energies) and increasing the range modulation for targets or contracting 2DRS cavity (or removing spots with higher energies) and decreasing the range modulation for OARs distal to the target (Curtin-Savard et al., 1999; Moyers and Vatnitsky, 2012). If performing distal blocking (see section 3.7.1) to an OAR, extra margin may need to be applied because the beam range is typically prescribed to the 90% dose level while the dose level allowed to the OAR may be lower. Historically, distal blocking in light ion beam treatments was discouraged, but it can be a powerful tool; when used, the penetration uncertainties were often applied at the $4k_p$ to $8k_p$ level.

The case for patch portals is unique with respect to penetration uncertainties. Patching consists of two or more portals where the distal edge of one portal abuts against the lateral edge of the other portal, each portal treating a separate sub-volume of the target (Moyers and Vatnitsky, 2012). In this case, distal blocking is used not against an OAR, but against a dose distribution inside a target. For patch portal design, it is assumed that the nominal conditions for penetration are perfect. For this reason the 2DRS is expanded only for scatter—this is small and usually accounted for by the unavoidable size of the milling tool without the need to purposely add expansion—but not for uncertainties. It is recommended that the patch surface between the two portals be moved often during the course of treatment to blur any real uncertainties and the dose heterogeneity that often arises because the lateral and distal penumbras of the two portals do not match. Figure 28 shows a typical dose distribution at the junction of a "patch" portal and a "through" portal where the distal penumbra of the patch portal is steeper than the lateral penumbra of the through portal.

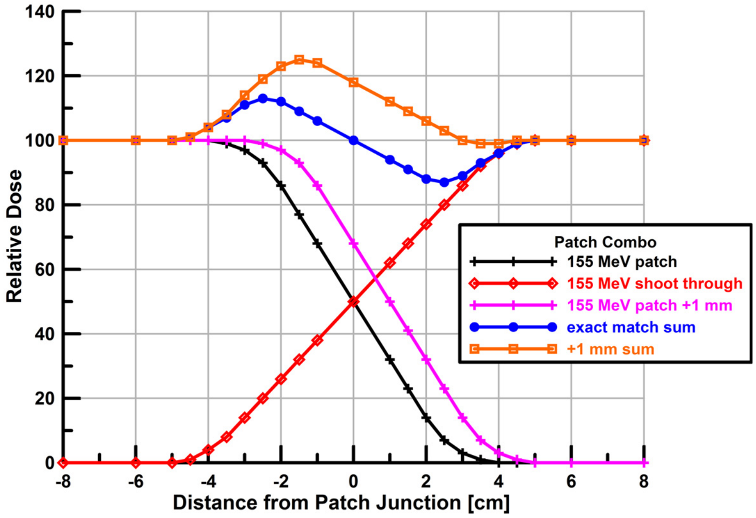

Figure 28. Dose distribution at the junction of a patch combination. The blue curve shows the distribution without uncertainties. The orange curve shows the dose distribution if the patch portal penetrates too deep by 1 mm and the lateral edge of the through portal is at its expected location. Reproduced from Moyers and Vatnitsky (2012) with permission from Medical Physics Publishing.

A technique used for many years to overcome both the uncertainty in the PUPC and PUBD and a shallow gradient of the distal penumbra has been to insert a block distal to the target but proximal to organs at risk. Examples of tissue separation include a block in the mouth, a wax or water-filled balloon in a cavity, and a permanent or temporary implant inside the body.

10.5 Selection of Number of Portals and Portal Directions

The choice of portal angles is usually chosen to avoid organs at risk or to reduce dose to nonspecific tissue, but assuming those goals are met, the choice can also be used to make the plan robust against uncertainties. Two major objectives for portal direction selection are (1) avoiding tissue heterogeneities in the entrance region (including extreme oblique incidence) and (2) avoiding portal directions that lead to light ion beams that stop directly in front of a critical structure.

The avoidance of tissue heterogeneities in the entrance path reduces dose uncertainty due to several factors:

- Reduction of dose calculation uncertainty. Pencil-beam algorithms have principle limitations regarding their accuracy in heterogeneous tissue. This applies in particular to the modeling of MCS along long tissue interfaces parallel to the beam direction.
- Tissue heterogeneities are more sensitive to alignment uncertainties as the component of patient shift lateral to the beam direction may lead to under- or over-penetration of light ions.

The avoidance of heterogeneities in the beam path applies not only to tissue within the patient, but also to materials outside of the patient. For example, light ion beams passing through the edge of the tabletop cause dose uncertainty. Concepts to assist treatment planners in the quantification of tissue heterogeneity have been developed (e.g., the heterogeneity index proposed by Pflugfelder, 2007). It remains to be seen if such measures will be integrated into commercial TPSs.

The avoidance of portal directions that stop in front of critical structures is a way to manually achieve robustness against over-penetration of the beam with respect to the maximum OAR dose. One example is a prostate treatment where the dose-limiting critical structure is the rectal wall. Instead of using an anterior-posterior (AP) portal that would allow for optimal sparing of the rectal wall by utilizing the steep distal dose gradient of the light ion beam, the typical approach uses two laterally opposed portals to avoid treating through a variably filled bladder and placing the distal edge of the beam, with a higher and uncertain RBE, possibly in the rectal wall. Although the laterally opposed portals approach leads to suboptimal sparing of the rectal wall due to the wide lateral penumbra of the beam—and there are additional concerns about penetration uncertainty due to misalignment of the femoral heads in the beam entrance path with the 2DRSs and the target—these concerns are overridden by the absence of critical organs left and right of the prostate.

Another example where concerns about penetration uncertainty impact the choice of portal directions is that of concave tumors surrounding the spinal cord or brain stem. For instance, paraspinal tumors located posterior to the spinal cord could be treated with a posterior-anterior (PA) portal, thus sparing the spinal cord via the steep distal dose gradient near the beam range. To minimize penetration uncertainty concerns, such treatments employ oblique portals that avoid the spinal cord laterally. With these portal directions it is not possible to cover the entire target with a single portal. Consequently, the target is partitioned into parts that are covered by different portals. This technique, described in section 10.4, has been termed patching (Bussiere, 2003). It is thus impossible to simultaneously protect against under-penetration (leading to underdose at the patch surface) and over-penetration (leading to overdose at the patch surface). It is, therefore, assumed that the penetration of the patch portal exactly matches the nominal penetration. In order to reduce the amount of potential dose errors at the patch surface, different patch portal combinations with different directions are often used, placing the patch surfaces at different locations within the tissue.

In light ion beam treatments, the number of portals treated per fraction is often kept to a minimum for practical considerations. Furthermore, the total number of portal directions is often limited by the dose-volume constraints for the normal tissues. In some cases, however, dose uncertainties from one or a few portal direction can be mitigated by increasing the number of portals. For example, if a target is treated with a single portal, the distal edge of the target is at risk of receiving almost zero dose in an under-penetration scenario, which may, in turn, require large distal margins. If instead, multiple portals are used, the risk of severe under-dose is reduced. Another example for increasing the number of portals is the use of different patch/through-portal combinations.

10.6 Mathematical Robust Optimization Techniques

This section discusses the use of mathematical robust optimization methods for treatment planning. It thus applies only to delivery techniques that use mathematical optimization for treatment planning, i.e., SPO and MPO. Robust optimization methods for handling SPO and MPO planning have been researched for many years, but only since 2016 have commercial planning systems provided viable implementations. This planning methodology is now becoming available to practitioners; however, practical experience for implementing it into the clinic is still limited. This section is, therefore, intended to provide the reader with a basic understanding of robust optimization methods and what to expect from them.

The use of robust optimization is partly motivated by the principle limitations of target and OAR expansion methods in energy and fluence modulation (EFM). For instance, an alignment error or a penetration error leads to a misalignment of the dose contributions from different portals. Especially for highly modulated portals, this may lead to localized regions of over- or under-dose within the target, as well as overdosing in normal tissues—a problem that cannot be addressed by expanded margins.

10.6.1 Robust Optimization Methods

The goal of robust optimization is to make energy and fluence modulation (EFM) dose distributions resilient in the face of uncertainties. Robust optimization methods are commonly used in many fields of endeavor to account for the effects of uncertainties. For teletherapy, Unkelbach et al. (2018) have provided an extensive review of robust optimization methods. To provide a basic understanding of the notion of robust optimization in energy and fluence modulation (EFM), three approaches that have been published so far are briefly reviewed. For treatment planning, the assumed goal is to minimize an objective function f(D), which is a function of the dose distribution D(x), which is, in turn, a linear function of the spot weights x. A further assumption is that the uncertainty can be modeled via N discrete uncertainty scenarios k. Each scenario corresponds to a dose distribution D_k.

1. **The probabilistic approach.** In this approach, a probability distribution p_k is assigned to the uncertainty scenarios. For treatment planning, the expected value of the objective function is optimized:

   $$\text{minimize} \quad \sum_{k=1}^{N} p_k f(D_k)$$

   The approach thus aims at finding a treatment plan that is good for every error scenario, but a larger importance weight is assigned to the scenarios that are assumed to be more probable. A demonstration of this approach is discussed in Unkelbach et al. (2007, 2009).

2. **The minimax worst-case approach.** This approach minimizes the maximum value of the objective function that can occur for any error scenario. Formally this can be stated as:

   $$\text{minimize} \quad \max_k \left| f(D_k) \right|$$

The approach aims at finding the treatment plan that is as good as possible for the worst error scenario that can occur from among the assumed scenarios. A discussion of this approach can be found in Fredrikson (2011) and in Chen et al. (2012).

3. **Optimization of the voxel-by-voxel worst-case dose distribution.** In this approach, the objective function is optimized by evaluating the worst-case dose distribution, D_{wc}, which is defined as the minimum dose in target voxels and the maximum dose in normal tissue voxels. The minimum/maximum is taken over all scenarios on a voxel-by-voxel basis (section 11.1.2.).

   minimize $\quad f(D_0)+\alpha f(D_{wc})$

   Here, D_0 denotes the dose distribution for the nominal scenario (no error) and a is a parameter that weights treatment plan quality for the nominal case relative to the robustness term. The approach is described in Pflugfelder et al. (2008) and Liu et al. (2012).

Up to this stage, all of the above approaches have been discussed in the context of systematic penetration and alignment uncertainty only. Systematic comparisons between the approaches have only been performed to a limited degree (Fredriksson, 2014). Preliminary experience indicates that all approaches lead to qualitatively similar treatment plans. There is currently no evidence that one approach or the other generally leads to superior results, although some methods have disadvantages in specific situations.

10.6.2 Features of Robust Optimization Methods

Robust optimization methods are able to automatically generate treatment plans that have certain features that are expected from a robust plan. For penetration uncertainty, this can include the following aspects:

- automatic expansion of the irradiated volume distal to the target to ensure target coverage for under-penetration
- avoidance of beamlets that stop directly in front of critical structures to avoid OAR overdosing for over-penetration (paraspinal cases, sometimes head and neck cases)
- reduction in the steepness of gradients in the dose distributions contributed by individual portals to the total multi-portal dose distribution. As a consequence, the overall dose distribution becomes more resilient to uncertainties.

For alignment uncertainty, this can include:

- automatic expansion of the irradiated volume laterally to ensure target coverage allowing for alignment uncertainty
- avoiding steep dose gradients in the dose contributions of individual beams to mitigate the effect of misalignment of dose contributions

Figures 29 to 31 illustrate the use of robust optimization for the paraspinal case shown in Figure 29(a). The upper panel in Figure 30 shows the dose contributions of three highly modulated portals for an energy and fluence modulation (EFM) plan that does not account for robustness. In the nominal scenario, the sum of the dose from the three portals yields the dose distribution in Figure 29(b). The steep dose gradients in the dose contributions of each portal make the treatment plan sensitive to penetration and alignment errors (Figure 29(c–d)). The lower panel in Figure 30 shows a treatment plan that was optimized accounting for penetration uncertainty using the probabilistic approach. All three features described above are observed. As a consequence, the sensitivity against penetration uncertainty is greatly reduced, as shown in the DVHs in Figure 31. A detailed discussion can be found in the original publications on robust optimization for proton therapy (Pflugfelder et al., 2008;

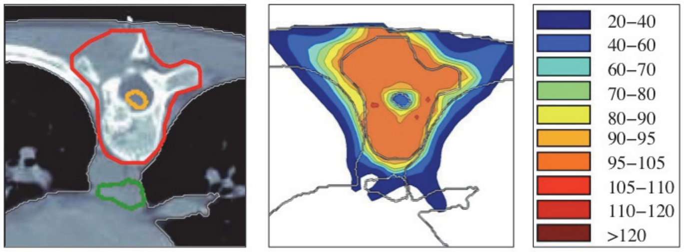

(a) paraspinal tumor

(b) nominal dose

% prescription

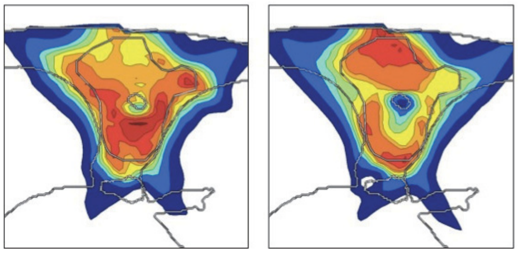

(c) 5 mm range overshoot

(d) 5 mm setup error posteriorly

Figure 29. Illustration of plan robustness evaluation using individual uncertainty scenarios. Panel (a) the geometry of the CTV (red) surrounding the spinal cord (orange); (b) the nominal dose distribution of an energy and fluence modulation (EFM) plan; (c) the dose distribution evaluated for the scenario that the penetration of all pencil beams is increased by 5 mm water equivalence (WEQ); (d) the dose distribution evaluated for a 5 mm alignment error posteriorly.

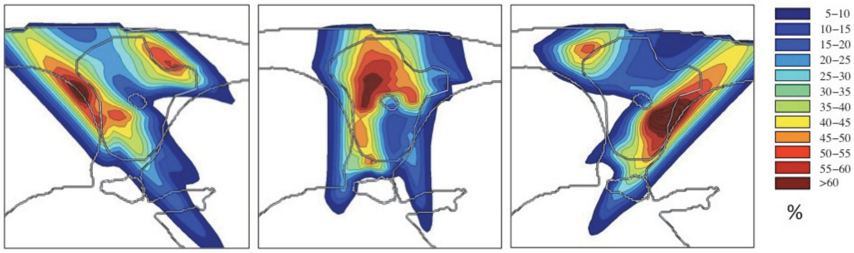

non-robust plan

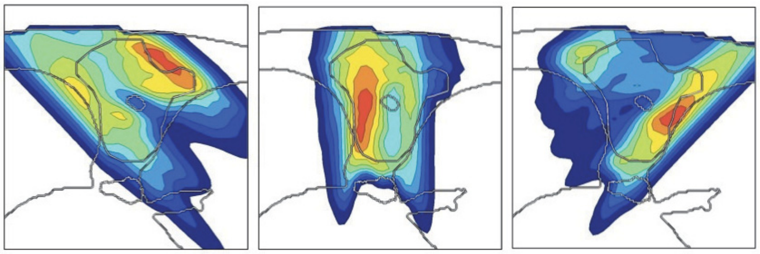

robust plan

Figure 30. Illustration of the cause of sensitivity against penetration and alignment errors. The upper panel shows the dose contribution of three highly modulated portals for the energy and fluence modulation (EFM) plan shown in Figure 29. Penetration and alignment uncertainties are not accounted for in the treatment plan optimization. This leads to steep dose gradients in order to achieve optimal sparing of the spinal cord. The bottom panel shows a robustly optimized treatment plan using the probabilistic methods (see section 10.7) to account for penetration uncertainty. The reduction of dose gradients in beam directions leads to more robust plans.

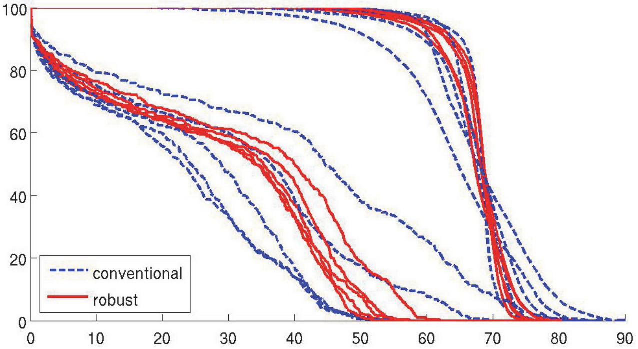

Figure 31. Robustness evaluation using DVHs of individual uncertainty scenarios for the paraspinal tumor example. Displayed are DVHs for the CTV and the spinal cord for the nominal scenario as well as 2.5 mm and 5.0 mm over-penetration and under-penetration scenarios. In this example, DVHs are used to compare two energy and fluence modulation (EFM) treatment plans (Figure 30): an energy and fluence modulation (EFM) plan optimized for the nominal scenario without accounting for robustness (blue lines) and a robust plan (red lines) obtained using the probabilistic method described in section 10.6.1.

Unkelbach et al., 2007, 2009; Frederikson et al., 2011, 2012; Liu et al., 2012, 2013). All of these papers consider systematic penetration and alignment errors as the uncertainty. Most papers use paraspinal cases for illustration because all of the above-mentioned effects can be illustrated. For other, less-challenging tumor sites, only a subset of these effects is relevant.

At the time this report was finalized, at least three major TPS manufacturers had released some robust optimization functionality. Interestingly, one system implemented the minimax, one the probabilistic, and one the worst case method.

10.7 Choice of Delivery Technique

Despite the robustness techniques described above, the delivery technique with the best target dose coverage and best OAR avoidance may not be the most robust. One may choose to use a technique that is less conformal to targets or less protective to OARs for the purpose of delivering a more certain dose distribution. The list below ranks, for most situations, the most robust to least robust delivery techniques.

1. Scattered beams with ridge filters, collimators, and 2DRS. These are the most robust because the whole dose distribution is nearly continuously delivered.
2. Scattered beams with rapidly rotating modulator propellers, collimators, and 2DRSs. These are the next most robust because the whole distribution is delivered multiple times per second. Generally, motion is not much of a problem, except when a low dose per portal is prescribed.
3. Uniform scanning with ridge filter, collimators, and 2DRS. The lateral scanning is fairly rapid compared to patient motion and is usually not a problem. All depths are treated simultaneously.
4. Uniform scanning with energy stacking, collimators, and 2DRSs. The slow energy switching time makes this delivery technique sensitive to intra-fractional motion.
5. Modulated scanning with energy stacking, and SPO. Except for large fields, the lateral scanning is fairly rapid compared to patient motion. The slow energy switching time, however, makes this delivery technique sensitive to intra-fractional motion.
6. Modulated scanning with energy stacking, and MPO. This technique can potentially create many steep dose gradients inside the target that must be matched to reciprocal gradients of other portals. Uncertainties in alignment at different gantry or patient positioner angles and intra-fraction motion can cause large deviations in the delivered dose distribution.

The planner should be cautious when using highly modulated plans. MPO is a powerful tool for some cases, but it should be used only when its advantages outweigh its disadvantages. Most centers that have modulated scanning capability try to design plans using SPO instead of MPO whenever possible.

10.8 Biophysical Optimization

The previous subsections dealt only with optimization of the physical dose distribution and delivery. Obviously one could also perform optimization taking into account biophysical factors, such as fractionation, tissue type, tissue volume, and linear energy transfer (LET). In recent years, several approaches have been developed to include a variable RBE into plan optimization (Wilkens and Oelfke, 2005). A major concern in that regard is the uncertainty in RBE. To address that issue, LET-based planning schemes have been developed that aim to avoid high LET in critical structures (Unkelbach et al., 2016) or that increase the LET within the GTV (Fager et al., 2015). A detailed discussion of these biophysical optimization schemes is beyond the scope of this report, but they should also be considered when optimizing plans.

10.9 Recommendations

- The physicist, therapist, and physician must agree upon the k_p value to be applied for each patient treatment. Generally, different classes of patient treatments will be assigned different levels of acceptable uncertainty.
- The user should be aware that the PTV/PRV approach does not work well with charged particle beams. Methods that minimize deviations in delivered dose under different conditions are preferred.
- Different TPSs have different optimization tools available to the user. The user should become intimately familiar with not only the tools available, but also the tools not available, particularly if the user had previous experience using a TPS from a different manufacturer.
- The planner should make use of both manual and automatic optimization techniques. With most current TPSs, the beam entry angle and avoidance of heterogeneities is under manual control, and their effect on the uncertainties must not be ignored.
- If a facility has multiple beam delivery methods, selection of the method to apply to a particular patient treatment should include an evaluation of the associated uncertainties for the conditions of the plan.
- When using EFM portals, the use of more portals per day may increase the uncertainty rather than decrease it, depending upon the delivered dose, target geometry, and other factors. When possible, SPO should be used with as few portals per fraction as possible. Where needed, MPO may be used and the number of portals per fraction may be increased.

11. Dose Distribution Evaluation and Visualization

11.1 Dose Estimates

Historically, TPSs have calculated the best estimate of the dose distribution under the most probable conditions. This best estimate of the delivered dose distribution can be referred to as the “nominal” dose distribution. Due to the uncertainties described in this report—and the greater vulnerability of light ions to them as compared to x-ray beams—it is likely that the delivered dose distribution is quite different from the calculated nominal distribution, more so than it would be for x-ray beams. To provide the patient’s physician more information to evaluate possible outcomes of alternative treatment plans, various methods to evaluate and visualize possible dose distributions have been devised.

In megavoltage x-ray therapy, evaluation of the effect of uncertainties on the dose distribution delivered to the CTV is often based on the dose distribution coverage of the PTV. The underlying assumption for comparing the nominal dose distribution with the PTV is that the dose distribution in space remains essentially unaffected by target position variations and heterogeneities; therefore, the target should be adequately covered as long as it remains within the PTV. In x-ray therapy, robustness of a plan against alignment errors or anatomic changes is thus indirectly assessed through evaluation of the PTV coverage. In contrast with x-ray therapy, this assumption is violated in light ion therapy in general and more seriously when energy and fluence modulation (EFM) techniques are used. In light ion therapy, assessing PTV coverage as a surrogate for robustness is generally insufficient due to several effects:

- For megavoltage x-ray therapy, PTVs are used to assign margins based solely on estimates of uncertainties in the target position; whereas in light ion therapy, uncertainty in beam penetration, which is beam-direction-specific, must also be considered. This means that there is not a unique PTV that can be used for the plan, and the PTV dose distribution loses its meaning.

- In heterogeneous tissue, a lateral alignment error does not simply lead to a shift of the dose distribution in the patient. The misalignment of the beam with tissue heterogeneities may lead to under- or over-penetration and a degraded dose distribution (Lomax, 2008). This problem affects all light ion therapy techniques, including techniques for which all portals aim to deliver a homogeneous dose distribution to the target. The effect is less severe in homogeneous tissue.
- An alignment error or a penetration error leads to a misalignment of the dose contributions from different portals. This may lead to localized regions of over- or under-dose—a problem that cannot be addressed by expanded margins. The effect is primarily problematic for highly modulated portals and less severe for techniques where every portal delivers a homogeneous target dose; however, it also occurs in homogeneous media.

The sensitivity of light ion therapy plans to penetration and alignment uncertainties is illustrated in Figures 29 and 30 for an energy and fluence modulation (EFM) plan for a paraspinal tumor. A representative x-ray CT slice is shown in Figure 29(a). In this case, the target volume (red) surrounds the spinal cord (orange), so that sparing the spinal cord requires highly modulated portals. In addition, the target volume contains soft tissue and bone, and it is located next to lung tissue. Figure 29(b) shows an optimized energy and fluence modulation (EFM) dose distribution for a treatment plan with three incident beam directions. The dose contributions of the three individual portals are shown in Figure 30 (upper panel). The steep dose gradients in the dose distribution of each portal make the plan sensitive to misalignments resulting from penetration or alignment uncertainties. Panel 29(c) shows the dose distribution resulting from a 5 mm over-penetration; panel 29(d) shows the dose for a 5 mm alignment error posteriorly. An alignment error in the posterior direction effectively shifts the dose contributions of the oblique beams apart, leading to localized under doses within the target volume. The case represents a drastic example to demonstrate the general insufficiency of PTV-based approaches. For other treatment sites with less-modulated portals in more homogeneous tissue, the effects will be less pronounced.

Due to the principle limitations of PTV-based plan evaluation, more refined methods to evaluate a treatment plan should be used for light ion therapy. In this section (11.1), methods for evaluating uncertainties associated with ‘static’ patient geometries are described, excluding the difficulty of anatomical changes. In sections 11.2 and 11.3, additional problems related to anatomical changes (including respiratory motion) are outlined. The most common methods to assess uncertainty in static geometries can be broadly classified into one of three categories: (1) evaluation of individual scenarios, (2) maximum and minimum doses (worst-case measures), and (3) statistical measures. These methods are discussed in sections 11.1.1, 11.1.2, and 11.1.3 below.

11.1.1 Individual Scenarios

The first category for evaluating the effects of uncertainties calculates individual error scenarios. In this approach, dose distributions and associated DVHs are calculated for several relevant uncertainty scenarios. Examples of scenarios to define include:

- *Systematic alignment error:* The treatment plan is evaluated for a specified systematic error in the patient position relative to the beam.
- *Over-penetration scenario:* The dose distribution is evaluated for situations where all light ions penetrate further into the patient than anticipated in the nominal scenario. There are different methods to simulate an over-penetration. A common method consists in down-scaling the RLSTPs obtained from the x-ray CT by a specified percentage. Another approach consists of increasing the incident light ion energy.

- *Under-penetration scenario:* In analogy to an over-penetration, the dose distribution is evaluated for the situations where all light ions penetrate less deep into the patient than anticipated in the nominal scenario.

The evaluation of the dose distribution for individual scenarios is illustrated in Figure 29 for a paraspinal tumor. In addition, Figure 31 illustrates a plan comparison using DVHs for the two energy and fluence modulation (EFM) plans (robust and non-robust) shown in Figure 30.

The explicit evaluation of individual uncertainty scenarios is necessarily limited to a small number of scenarios. If a large number of possible error scenarios are to be included into the uncertainty evaluation, it is desirable to consolidate the information contained in multiple dose distributions. Such methods can be based on worst-case measures (section 11.1.2) or statistical measures (11.1.3).

11.1.2 Minimum and Maximum Doses

The goal of methods in this category is to determine the minimum and maximum doses that might be delivered in the execution of a treatment plan, assuming that the uncertainties are within some specified intervals. An early example of a method in this category is the minimum and maximum approach described by Goitein (1985). In this method, three possible doses are calculated for every voxel in the patient according to the maximum and minimum doses that might be delivered. The maximum doses for each voxel are determined for each individual portal by expanding the aperture by the lateral alignment uncertainty (LAU), extending the range and range modulation by the penetration uncertainties due to beam delivery (PUBD) and penetration uncertainties due to physical characterization (PUPC), and by increasing the D/MU due to the expected uncertainties of calibration and dose delivery. Likewise, the minimum doses for each voxel are determined for each individual portal by contracting the aperture by the lateral alignment uncertainty (LAU), reducing the range and range modulation by the penetration uncertainties due to beam delivery (PUBD) and penetration uncertainties due to physical characterization (PUPC), and by decreasing the D/MU due to the expected uncertainties of calibration and dose delivery. The maximum and minimum doses for the plan are obtained by summing the maximum doses from all portals together and summing the minimum doses from all portals together. This approach provides three dose distributions: one containing the maximum dose to each voxel, one containing the minimum dose to each voxel, and one containing the nominal dose to each voxel. The minimum and maximum dose distributions would never be deliverable because the aperture would not be expanded on both sides simultaneously, and the range would not be deeper and shallower simultaneously, but the resulting doses to the individual voxels do bracket what doses could be delivered. The three doses may be queried at any voxel by moving a cursor to any point in the plan, looking at three sets of isodose curves, or looking at three DVH distributions. As of 2012, this method was the only uncertainty evaluation method incorporated into a commercial TPS (Curtin-Savard et al., 1999). With small modifications, the Goitein method can also be used for modulated scanning and energy-stacked beam delivery techniques without apertures and 2DRSs (see Moyers and Vatnitsky, 2012).

A similar worst case scenarios method has been described by Lomax (2008) in the context of energy and fluence modulation (EFM). In this method, different dose distributions are obtained by applying shifts to the isocenter positions of whole beam arrangements and increasing and decreasing the range of protons based on penetration uncertainties, as described in section 11.1.1. Excluding the cases involving respiratory motion, this method results in nine dose distributions, including the nominal one. Each voxel in the tumor is assigned the minimum dose, and each voxel in normal tissues is assigned the maximum dose from the nine individual doses. The resulting dose distribution is termed the “worst case” dose distribution. As in the previous methods, the worst case dose distributions cannot be realized, however, they represent a conservative approach to visualize, on a voxel-by-voxel basis, the worst case doses that might be delivered. In this sense, this method is an analog of the PTV- and PRV-based evaluation approach for photons, which also represents the worst that can happen to the CTV and normal tissues. Incorporation of respiratory motion in this approach is complex and is being investigated.

Trofimov (2012) has used these previous methods to provide a family of DVHs based upon the individual portal shifts of alignment and penetration. In this approach, the various scenarios provide a band of DVHs as a way to visualize the variability of the DVH under the influence of the uncertainties. A narrow DVH band is desirable for the target, indicating that the dose distribution is relatively insensitive to uncertainties.

11.1.3 Statistical Measures

Methods in this category require a probabilistic description of the uncertainty. This means that a probability distribution over the uncertain treatment parameters is assumed, e.g., a Gaussian distribution over a range of alignment errors. The probability distribution of the underlying treatment parameters leads to a probability distribution of the dose distribution that may be delivered. Different measures to characterize aspects of this distribution can be calculated:

- An example of a statistical measure method is to calculate the expected value and the standard deviation of the dose in every voxel. In the case that a homogeneous dose distribution is to be delivered to the target volume, the expected dose value indicates if the prescribed dose is met on average; the standard deviation quantifies by how much the realized dose deviates on average from the expected dose (Unkelbach et al., 2007, 2009).
- Another possibility consists of estimating the probability (on a voxel-by-voxel basis) that the dose is within some interval. For example, for the target volume, the probability that the dose is within 5% of the prescription dose can be displayed. For a critical structure, the probability that the dose is above a tolerance threshold is displayed (Maleike, 2006).

Statistical measures have been published in the literature, but are not known to be applied in practice in any light ion treatment centers.

11.2 Inter-fractional Anatomy Changes

If multiple images of a patient from different days are available, a given treatment plan can be evaluated on each of these image data sets. Such imaging is, however, usually not available at the time of initial treatment planning. In addition, a small number of image data sets may not represent the full range of anatomical variations that a treatment plan should be robust against. To address this problem, robustness evaluation against penetration and alignment errors may serve as a surrogate for robustness evaluation against anatomical changes. This evaluation requires an estimate on the additional variation in penetration that can be caused by changes in the anatomy. Certainly, this estimate will be treatment-site-specific and may depend upon the motion mitigation techniques used at an institution.

If the patient anatomy is expected to change over time (see section 9), this may give rise to repeated imaging during therapy and a replanning strategy. It may be necessary to periodically image the patient and evaluate whether the original treatment plan remains adequate for the new anatomy configuration. To that end, the portal configurations from the previously approved treatment plan are transferred to a new plan using the repeat x-ray CT scan. The dose distribution is then recalculated, and a new set of DVHs are created for all anatomic structures. If the evaluation of the recalculated dose distributions shows that the original constraints are being violated, a new plan is designed. There are indications that the need and frequency for adaptive replanning is greater for light ion therapy than for x-rays.

11.3 Intra-fractional Respiratory Motion

The currently available methods for evaluating treatment plans in the presence of respiratory motion are limited. Motion is typically assessed using 4-dimensional x-ray CT, which provides a snapshot of the patient geometry in different phases of the respiratory cycle. In current practice, a treatment plan is often evaluated based on the dose distribution calculated on the maximum or average intensity projection image derived from the 4-dimensional x-ray CT data. This can be improved by evaluating the dose distribution on each of the phases separately in order to assess whether the target volume is covered in each phase of the respiratory cycle.

Ideally, the cumulative dose delivered to the patient throughout the respiratory cycle is calculated; however, this is complicated by several practical and conceptual difficulties. In particular, adding dose contributions from multiple respiratory phases requires deformable registration of all phases and weighting the dose distributions in each breathing phase according to the monitor units delivered in each phase. Progress has been made in this field of deformable registration, and an increasing number of planning systems may implement such functionality. Nevertheless, deformable registration may remain cumbersome to use, and the calculation of a cumulative dose distribution may be time-consuming and not always practical.

Measurements of the actual dose delivered to individual patients, such as by inserting small radiation detectors through the airway and placing them adjacent to tumors, are extremely limited. Phantom measurements are useful in commissioning, but can only lead to advice for individual patients.

In a research environment, advanced methods for treatment plan evaluation are being developed that, for example, assess the role of interplay effects between the motion of the tumor and the motion of a scanning beam. It is unclear, however, what degree of treatment plan evaluation will be needed on a patient-by-patient basis. In 2016, the DICOM communications standard was modified such that the recorded time of delivery of each spot for a modulated scanning beam could be transmitted back into a treatment planning system along with the patient motion profile, making it possible to calculate the delivered dose distribution. In practice, however, large margins are still added in the treatment planning process for lung tumors in order to have confidence in covering the tumor due to the limited plan evaluation tools. In order to reduce margins and improve light ion plans, it may also be necessary to develop more advanced treatment plan evaluation methods to provide greater confidence in delivering smaller margins.

11.4 Recommendations

The best procedure for evaluating treatment plan robustness in clinical practice will depend on the plan evaluation tools that the TPS provides. Light ion therapy TPSs are currently evolving as more vendors enter the market. It remains to be seen which tools for visualizing and assessing plan robustness will be widely implemented. Some general recommendations include:

- It should be understood that PTV coverage—which in x-ray therapy serves as a surrogate for robustness against alignment errors and anatomic variations—does not necessarily guarantee CTV coverage in light ion therapy. It is, therefore, recommended that the treatment plan is evaluated for individual uncertainty scenarios by explicitly calculating DVHs and dose distributions. CTV and normal tissue DVHs corresponding to the worst case dose distribution, either using the Lomax approach or Fredrickson approach, may be used in light ion therapy similarly to PTV and PRV DVHs for x-rays.
- Special attention to robustness evaluation should be paid when evaluating dose distributions in heterogeneous tissue and for highly modulated portals in energy and fluence modulation (EFM).
- When comparing light ion beam plans to megavoltage x-ray beam plans, the robustness of each type of plan should be evaluated separately. As the tumor response is most closely associated with the average dose to the CTV (see section 10.2), ion and x-ray dose response should be compared using the CTV dose metrics.

12. Summary

There are many physical uncertainties associated with the planning and delivery of light ion beam treatments. Lateral alignment uncertainties (LAUs) are similar to those encountered in x-ray and electron beam treatments, but the unique configurations and large size and weight of the delivery equipment require careful analysis of the sub-components. Penetration uncertainties are similar to those encountered in electron beam treatments, but they are much more important because of the larger dose gradients encountered in light ion beams and the variety of planning, delivery, and delivery monitoring techniques. Of particular importance are penetration differences due to lateral misalignments; therefore, LAUs lead to penetration uncertainties. The large dose gradients produced by light ion beams also exacerbate the effects of patient motion, particularly with beam delivery techniques that treat one part of the patient at a time, such as with scanning beams. Each facility should individually assess the uncertainties to apply in treatment planning. Authors of future studies should report k_p values with all reported uncertainty values so that the light ion community may benefit from the collective experience. Treatment planners should place special emphasis on generating plans that are robust to the effects of uncertainties. To assist with this task, dose distributions calculated under non-nominal conditions should be evaluated.

13. References

American Association of Physicists in Medicine (AAPM). "Specification and Acceptance Testing of Computed Tomography Scanners." AAPM Report No. 39. New York: American Institute of Physics, 1993.

American Association of Physicists in Medicine (AAPM). (2003). "Quality assurance for computed-tomography simulators and the computed-tomography-simulation process: Report of the AAPM Radiation Therapy Committee Task Group No. 66." *Med. Phys.* 30(10):2762–2792.

Andreo, P. (2009). "On the clinical spatial resolution achievable with protons and heavier charged particle radiotherapy beams" *Phys. Med. Biol.* 54(11):N205–N215.

Anferov, V. A. (2009). "Scan pattern optimization for uniform proton beam scanning" *Med. Phys.* 36(8):3560–3567.

Arjomandy, B., N. Sahoo, et al. (2009). "An overview of the comprehensive proton therapy machine quality assurance procedures implemented at The University of Texas M. D. Anderson Cancer Center Proton Therapy Center-Houston" *Med. Phys.* 36(6):2269–2282.

Barrett, J. F. and N. Keat. (2004). "Artifacts in CT: Recognition and Avoidance" *RadioGraphics* 24:1679–1691.

Battista, J. J., W. D. Rider, and J. Van Dyk. (1980). "Computed tomography for radiotherapy planning." *Int. J. Radiat. Oncol. Biol. Phys.* 6:99–107.

Baumer, C. and J. B. Farr. (2011). "Lateral dose profile characterization in scanning particle therapy." *Med. Phys.* 38(6):2904–2913.

Bichsel, H. and T. Hiraoka. (1992). "Energy loss of 70 MeV protons in elements." *Nucl. Instrum. Methods B* 66:345–351.

Bihsel, H., T. Hiraoka, and K. Omata. (2000). "Aspects of fast-ion dosimetry." *Radiat. Res.* 153:208–219.

Bissonnette, J. P., P. A. Balter, L. Dong, K. M. Langen, D. M. Lovelock, M. Miften, et al. (2012). "Quality assurance for image-guided radiation therapy utilizing CT-based technologies: a report of the AAPM TG-179." *Med. Phys.* 39(4):1946–1963.

Blakely, E. A., C. A. Tobias, B. A. Ludewigt, and W. T. Chu. (1986). “Some physical and biological properties of light ions.” In *Proceedings of the Fifth PTCOG Meeting & International Workshop on Biomedical Accelerators,* W. Chu, ed. Lawrence Berkeley Laboratories Report LBL-22962.

Bortfeld, T., W. Schlegel, and B. Rhein, B. (1993). “Decomposition of pencil beam kernels for fast dose calculations in three-dimensional treatment planning.” *Med. Phys.* 20(2):311–318.

Bortfeld, T., S. Jiang, and E. Rietzel. (2004). “Effects of motion on the total dose distribution.” *Semin. Radiat. Oncol.* 14(1):41–51.

Brahme, A. (1984). “Dosimetric precision requirements in radiation therapy.” *Acta Radiol. Oncol.* 23(5):379–391.

Brahme, A. and A. K. Ågren. (1987). “Optimal dose distribution for eradication of heterogeneous tumors.” *Acta Radiol. Oncol.* 26:377–385.

Brahme, A., J. Eenmaa, S. Lindbäck, A. Montelius, and P. Wooton. (1983). “Neutron beam characteristics from 50 MeV protons on beryllium using a continuously variable multi-leaf collimator.” *Radiother. Oncol.* 1(1):65–76.

Brahme, A., B. Lind, and P. Nafstadius. (1987). “Radiotherapeutic computed tomography with scanned photon beams.” *Int. J. Radiat. Oncol. Biol. Phys.* 13:95–101.

Bues, M., W. D. Newhauser, U. Titt, and A. R. Smith. (2005). “Therapeutic step and shoot proton beam spot-scanning with a multi-leaf collimator: A Monte Carlo study.” *Radiat. Prot. Dosim.* 115(1–4):164–169.

Bushberg, T. J., J. A. Seibert, E. M. Leidholdt, and J. M. Boone. *The Essential Physics of Medical Imaging.* Philadelphia: Williams & Wilkins, 2001.

Bussiere, M. and J. Adams. (2003). “Treatment planning for conformal proton radiation therapy.” *Tech. Canc. Res. Treat.* 2(5):389–399.

Chen, C. Y., K. S. Chuang, J. Wu, H. R. Lin, and M. J. Li. (2001). “Beam hardening correction for computed tomography images using a postreconstruction method and equivalent tissue concept.” *J. Digit. Imaging* 14(2):54–56.

Chen, W., J. Unkelbach, A. Trofimov, T. Madden, H. Kooy, T. Bortfeld, and D. Craft. (2012). “Including robustness in multi-criteria optimization for intensity-modulated proton therapy.” *Phys. Med. Biol.* 57:591–608.

Chvetsov, A. V. and S. L. Paige. (2010). “The influence of CT image noise on proton range calculation in radiotherapy planning.” *Phys. Med. Biol.* 55(6):N141–149.

Chu, W. T., B. A. Ludewigt, and T. R. Renner. (1993). “Instrumentation for treatment of cancer using proton and light-ion beams.” Lawrence Berkeley Laboratories Report LBL-33403, UC406.

Cormack, A. M. (1963). “Representation of a function by its line integrals, with some radiological applications.” *J. Appl. Physics* 34(9):2722–2727.

Coutrakon, G., N. D. Wang, D. W. Miller, and Y. Yang. (2010). “Dose error analysis for a scanned proton beam delivery system.” *Phys. Med. Biol.* 55(23):7081–7096.

Curtin-Savard, A. J., D. W. Miller, S. M. Vatnitsky, M. F. Moyers, and B. Patyal. (1999). “New features and commissioning status of the Optirad treatment planning system.” Presented at the Proton Therapy Co-operative Group meeting, Bloomington, Indiana, October 11–13, 1999.

Daartz, J., M. Bangert, M. R. Bussiere, M. Engelsman, and H. M. Kooy. (2009). “Characterization of a mini-multileaf collimator in a proton beamline.” *Med. Phys.* 36(5):1886–1894.

Dawson, L. A., K. K. Brock, S. Kazanjian, D. Fitch, C. J. McGinn, T. S. Lawrence, R. K. Ten Haken, and J. Balter. (2001). “The reproducibility of organ position using active breathing control (ABC) during liver radiotherapy.” *Int. J. Radiat. Oncol. Biol. Phys.* 51(5):1410–1421.

De Marzi, L., C. Lesven, R. Ferrand, J. Sage, T. Boulé, and A. Mazal. (2013). “Calibration of CT Hounsfield units for proton therapy treatment planning: use of kilovoltage and megavoltage images and comparison of parameterized methods.” *Phys. Med. Biol.* 58(12):4255–4276.

DICOM Standards Committee, Working Group 7 Radiotherapy Objects. “Radiotherapy Extensions for Ion Therapy.” *Supplement 102.* Rossyln, Virginia: National Electrical Manufacturers Association, 2006.

Diffenderfer, E. S., C. G. Ainsley, M. L. Kirk, J. E. McDonough, and R. L. Maughan. (2011). “Comparison of secondary neutron dose in proton therapy resulting from the use of a tungsten alloy MLC or a brass collimator system.” *Med. Phys.* 38(11):6248–6256.

Dingfelder, M., D. Hantke, M. Inokuti, and H. G. Partzke. (1999). “Electron inelastic-scattering cross sections in liquid water.” *Radiat. Phys. Chem.* 53(1):1–18.

Engelsman, M., H. M. Lu, D. Herrup, M. Bussiere, and H. M. Kooy. (2009). “Commissioning a passive-scattering proton therapy nozzle for accurate SOBP delivery.” *Med. Phys.* 36(6):2172–2180.

Fabrikant, J. I., W. R. Holley, E. W. McFarland, and C. A. Tobias. (1982). “Heavy-ion radiography and heavy-ion computed tomography.” Presented at the Third International Symposium of Radiation Protection–Advances in Theory and Practice, Inverness, Scotland, June 6–11, 1982.

Fager, M., I. Toma-Dasu, M. Kirk, D. Dolney, E. S. Diffenderfer, N. Vapiwala, and A. Carabe. (2015). “Linear energy transfer painting with proton therapy: a means of reducing radiation doses with equivalent clinical effectiveness.” *Int. J. Radiat. Oncol. Biol. Phys.* 91(5):1057–1064.

Farr, J. B., F. Dessy, O. De Wilde, O. Bietzer, and D. Schonenberg. (2013). “Fundamental radiological and geometric performance of two types of proton beam modulated discrete scanning systems.” *Med. Phys.* 40(7):072101, 1–8.

Farr, J. B., A. E. Mascia, W. C. Hsi, C. E. Allgower, F. Jesseph, A. N. Schreuder, M. Wolanski, D. F. Nichiporov, and V. Anferov. (2008). “Clinical characterization of a proton beam continuous uniform scanning system with dose layer stacking.” *Med. Phys.* 35(11):4945–4954.

Fiorino, C., F. Foppiano, P. Franzone, S. Broggi, P. Castellone, M. Marcenaro, R. Calandrino, and G. Sanguineti. (2005). “Rectal and bladder motion during conformal radiotherapy after radical prostatectomy.” *Radiother. Oncol.* 73(2):187–195.

Flohr, T. G., K. Stierstorfer, C. Süss, B. Schmidt, A. N. Primak, and C. H. McCollough. (2007). “Novel ultrahigh resolution data acquisition and image reconstruction for multi-detector row CT.” *Med. Phys.* 34(5):1712–1723.

Fraass, B., K. Doppke, M. Hunt, G. Kutcher, G. Starkschall, R. Stein, et al. (1998). “American Association of Physicists in Medicine Radiation Therapy Committee Task Group 53: Quality assurance for clinical radiotherapy treatment planning.” *Med. Phys.* 25(10):1773–1829.

Fredriksson, A. and R. Bokrantz. (2014). “A critical evaluation of worst case optimization methods for robust intensity-modulated proton therapy planning.” *Med. Phys.* 41(8):081701.

Fredriksson, A., A. Forsgren, and B. Hardemark. (2011). “Minimax optimization for handling range and setup uncertainties in proton therapy.” *Med. Phys.* 38:1672–1684.

Fu, D. and G. Kuduvalli. (2008). “A fast, accurate, and automatic 2D-3D image registration for image-guided cranial radiosurgery.” *Med. Phys.* 35(5):2180–2194.

Fujitaka, S., T. Takayanagi, et al. (2009). “Reduction of the number of stacking layers in proton uniform scanning.” *Phys. Med. Biol.* 54(10):3101–3111.

Fuller, C. D., J. Nijkamp, J. C. Duppen, C. R. Rasch, C. R. Thomas, S. J. Wang, et al. (2011) “Prospective randomized double-blind pilot study of site-specific consensus atlas implementation for rectal cancer target volume delineation in the cooperative group setting.” *Int. J. Radiat. Oncol. Biol. Phys.* 79(2):481–489.

Furukawa, T., T. Inaniwa, S. Sato, E. Takeshita, K. Mizushima, K. Katagiri, Y. Hara, T. Shirari, and K. Noda. (2012). “Beam Monitors of NIRS Fast Scanning System for Particle Therapy.” Paper read at International Beam Instrumentation Conference, at Tsukuba, Japan.

Gay, H. A., H. J. Barthold, E. O'Meara, W. R. Bosch, I. El Naga, R. Al-Lozi, S. A. Rosenthal, C. Lawton, W. R. Wee, H. Sandler, A. Zeitman, R. Merson, L. A. Dawson, C. Willett, L. A. Kachnic, A. Jhingran, L. Portelanc, J. Ryu, W. Small, D. Gaffney, A. N. Viswanathan, and J. M. Michalski. (2012). "Pelvic normal tissue contouring guidelines for radiation therapy: a Radiation Therapy Oncology Group consensus panel atlas." *Int. J. Radiat. Oncol. Biol. Phys.* 83(3):e353–362.

Gelover, E., D. Wang, P. Hill, R. Flynn, M. Gao, S. Laub, M. Pankuch, and D. Hyer. (2015). "A method for modeling laterally asymmetric proton beamlets resulting from collimation." *Med. Phys.* 42:1321–1334.

Gennat, H. K. and D. Boyd. (1977). "Quantitative bone mineral analysis using dual energy computed tomography." *Invest. Radiol.* 12(6):545–551.

Gillin, M. T., N. Sahoo, M. Bues, G. Ciangaru, G. Sawakuchi, F. Poenisch, B. Arjomandy, C. Martin, U. Titt, K. Suzuki, A. R. Smith, and X. R. Zhu. (2010). "Commissioning of the discrete spot scanning proton beam delivery system at the University of Texas M. D. Anderson Cancer Center, Proton Therapy Center, Houston." *Med. Phys.* 37(1):154–163.

Goitein, M. (1972). "Three-dimensional density reconstruction from a series of two-dimensional projections." *Nucl. Instrum. Methods* 101:509–518.

Goitein, M. (1982). "Limitations of two-dimensional treatment planning programs." *Med. Phys.* 9(4):580–586.

Goitein, M. (1985). "Calculation of the uncertainty in the dose delivered during radiation therapy." *Med. Phys.* 12(5):608–612.

Goodman, K. A., W. F. Regine, L. A. Dawson, E. Ben-Josef, K. Haustermans, W. R. Bosch, et al. (2012). "Radiation Therapy Oncology Group consensus panel guidelines for the delineation of the clinical target volume in the post-operative treatment of pancreatic head cancer." *Int. J. Radiat. Oncol. Biol. Phys.* 83(3):901–908.

Gottschalk, B. (2010). "On the scattering power of protons." *Med. Phys.* 37(1):352–367.

Gottschalk, B., E. W. Cascio, J. Daartz, and M. S. Wagner. (2015). "On the nuclear halo of a proton pencil beam stopping in water." *Phys. Med. Biol.* 60(14):5627–5654.

Grevillot, L., T. Frisson, N. Zahra, D. Bertrand, F. Stichelbaut, N. Freud, and D. Sarrut. (2010). "Optimization of GEANT4 settings for proton pencil beam scanning simulations using GATE." *Nucl. Instrum. Methods Phys. Res. B* 268:3295–3305.

Groell, R., R. Rienmueller, G. J. Schaffler, H. R. Portugaller, E. Graif, and P. Willfurth. (2000). "CT number variations due to different image acquisition and reconstruction parameters: a thorax phantom study." *Comput. Med. Imaging Graph.* 24(2):53–58.

Grusell, E. and A. Montelius. (1994). "The leakage of protons between plane collimator leaves in a multileaf collimator." *Proceedings of NIRS International Seminar on the Application of Heavy ion Accelerator to Radiation Therapy of Cancer in connection with XX1 PTCOG Meeting NIRS-M*-103:116–124.

Haberer, T., W. Becher, D. Schardt, and G. Kraft. (1993). "Magnetic Scanning System for Heavy-Ion Therapy." *Nucl. Instrum. Methods Phys. Res. A*. 330(1–2):296–305.

Hanley, J., M. M. Debois, D. Mah, G. S. Mageras, A. Raben, K. Rosenzweig, B. Mychalczak, L. H. Schwartz, P. J. Gloeggler, W. Lutz, C. C. Ling, S. A. Leibel, Z. Fuks, and G. L. Kutcher. (1999). "Deep inspiration breath-hold technique for lung tumors: the potential value of target immobilization and reduced lung density in dose escalation." *Int. J. Radiat. Oncol. Biol. Phys.* 45(3):603–611.

Hanson, K. M., J. N. Bradbury, T. M. Cannon, R. L. Hutson, D. B. Laubacher, R. J. Macek, M. A. Paciotti, and C. A. Taylor. (1981). "Computed tomography using proton energy loss." *Phys. Med. Biol.* 26(6):965–983.

Hartmann, B., J. Telsemeyer, L. Huber, B. Ackermann, O. Jakel, and M. Martisikova. (2012). "Investigations of a flat-panel detector for quality assurance measurements in ion beam therapy." *Phys. Med. Biol.* 57(1):51–68.

Herman, G. T. and R. M. Lewitt. (1981). "Evaluation of a preprocessing algorithm for truncated CT projections." *J. Comput. Assist. Tomogr.* 5(1):127–135.

Hong, L., M. Goitein, M. Bucciolini, R. Comiskey, B. Gottschalk, S. Rosenthal, et al. (1996). "A pencil beam algorithm for proton dose calculations." *Phys. Med. Biol.* 41(8):1305–1330.

Hounsfield, G. N. (1973). "Computerized transverse axial scanning (tomography): part 1. description of system." *Br. J. Radiol.* 46:1016–1022.

Hsi, W. C., M. F. Moyers, D. Nichiporov, V. Anferov, M. Wolanski, C. E. Allgower, J. B. Farr, A. E. Mascia, and A. N. Schreuder. (2009). "Energy spectrum control for modulated proton beams." *Med. Phys.* 36(6):2297–2308.

Hsi, W. C., A. N. Schreuder, M. F. Moyers, C. E. Allgower, J. B. Farr, and A. E. Mascia. (2009). "Range and modulation dependencies for proton beam dose per monitor unit calculations." *Med. Phys.* 36(2):634–641.

Hsieh, J. *Computed Tomography Principles, Design, Artifacts, and Recent Advances.* Society of Photo-Optical Instrumentation Engineers, 2003.

Hünemohr, N., B. Krauss, C. Tremmel, B. Ackermann, O. Jäkel, and S. Greilich, S. (2014). "Experimental verification of ion stopping power prediction from dual energy CT data in tissue surrogates." *Phys. Med. Biol.* 59(1):83–96.

Hynds, S., C. K. McGarry, D. M. Mitchell, S. Early, L. Shum, D. P. Stewart, et al. (2011). "Assessing the daily consistency of bladder filling using an ultrasonic Bladderscan device in men receiving radical conformal radiotherapy for prostate cancer." *Br. J. Radiol.* 84(1005):813–818.

International Atomic Energy Agency. "Relative Biological Effectiveness in Ion Beam Therapy." *Technical Reports Series No. 461.* Vienna: International Atomic Energy Agency, 2008.

International Commission on Radiation Units and Measurements (ICRU). "Tissue Substitutes in Radiation Dosimetry and Measurement." *ICRU Report* 44. Bethesda, Maryland: ICRU Publications, 1989.

International Commission on Radiation Units and Measurements (ICRU). "Stopping Powers and Ranges for Protons and Alpha Particles." *ICRU Report* 49. Bethesda, Maryland: ICRU Publications, 1993.

International Commission on Radiation Units and Measurements (ICRU). "Prescribing, Recording, and Reporting Photon Beam Therapy." *ICRU Report* 50. Bethesda, Maryland: ICRU Publications, 1993.

International Commission on Radiation Units and Measurements (ICRU). "Medical Imaging–The assessment of image quality." *ICRU Report 54.* Bethesda, Maryland: ICRU Publications, 1996.

International Commission on Radiation Units and Measurements (ICRU). (2005). "Stopping of ions heavier than helium." *ICRU Report 73. Journal of ICRU 5(1).*

International Electro-technical Commission (IEC). "Particular requirements for the basic safety and essential performance of light ion beam ME equipment." *IEC 60601-2-64.* Geneva: IEC, 2014.

International Electro-technical Commission (IEC). "Medical electrical equipment–Light ion beam ME equipment–performance characteristics." *IEC 62667.* Geneva: IEC, 2017.

International Organization for Standardization. "Quality management and quality assurance standards–Part 1: Guidelines for selection and use." *ISO 9000-1.* Geneva: ISO, 1994.

Joint Committee for Guides in Metrology. *Evaluation of measurement data–Guide to the expression of uncertainty in measurement.* JGCM, 2008.

Janni, J. F. (1982). "Proton range-energy tables, 1 keV-10 GeV." *Atomic Data and Nuclear Data Tables* 27(2–5):147–529.

Johnson, T. R. C. and W. A. Kalender. “Physical background in Dual energy CT.” In *Clinical Practice*, T. R. C. Johnson, C. Fink, S. O. Schönberg, and M. F. Reiser, eds. Heidelberg: Springer, 2010.

Joseph, P. M. and R. D. Spital. (1982). “The effects of scatter in x-ray computed tomography.” *Med. Phys.* 9(4):464–472.

Kanai, T., K. Kawachi, and H. Matsuzawa. (1983). “Broad beam three-dimensional irradiation for proton radiotherapy.” *Med. Phys.* 10(3):344–346.

Kanematsu, N. (2009). “Semi-empirical formulation of multiple scattering for the Gaussian beam model of heavy charged particles.” *Phys. Med. Biol.* 54(5):N67–N73.

Kang, M., H. Chen, R. Cessac, and D. Pang. (2018). “Commissioning of a unique penumbra sharpening adaptive aperture for the first HYPERSCAN system.” Presented at the American Association of Physicists in Medicine meeting, MO-I345-GePD-F3-2.

Kijewski, M. F. and P. F. Judy. (1987). “The noise power spectrum of CT images.” *Phys. Med. Biol.* 32:565–575.

Klein, E. E., J. Hanley, J. Bayouth, F. F. Yin, W. Simon, S. Dresser, C. Serago, F. Aquirre, L. Ma, B. Arjomandy, C. Liu, C. Sandin, and T. Holmes. (2009). “Task Group 142 report: Quality assurance of medical accelerators.” *Med. Phys.* 36(9):4197–4212.

Klein, S. B. *Clinical Performance Requirements.* Internal Report Document 100041. Bloomington, Indiana: Indiana University Cyclotron Facility, 2003.

Kooy, H. M., S. J. Rosenthal, M. Engelsman, A. Mazal, R. L. Slopsema, H. Paganetti, and J. B. Flanz. (2005). “The prediction of output factors for spread-out proton Bragg peak fields in clinical practice.” *Phys. Med. Biol.* 50(24):5847–5856.

Krämer, M., O. Jäkel, T. Haberer, G. Kraft, D. Schardt, and U. Weber. (2000). “Treatment planning for heavy-ion radiotherapy: physical beam model and dose optimization.” *Phys. Med. Biol.* 45(11):3299–3317.

Kyriakou, Y., E. Meyer, D. Prell, and M. Kachelrieß. (2010). “Empirical beam hardening correction (EBHC) for CT.” *Med. Phys.* 37:5179–5187.

Langen, K. M., S. L. Meeks, D. O. Poole, T. H. Wagner, T. R. Willoughby, P. A. Kupelian, K. J. Ruchala, J. Haimerl, and G. H. Olivera. (2005). “The use of megavoltage CT (MVCT) images for dose recomputations.” *Phys. Med. Biol.* 50:4259–4276.

La Rivière, P. J. and X. Pan. (2004). “Sampling and aliasing consequences of quarter-detector offset use in helical CT.” *IEEE Trans. Med. Imaging* 23(6):738–749.

Leavitt, D. D., J. R. Stewart, J. H. Moeller, W. L. Lee, and G. A. Takach. (1989). “Electron arc therapy: Design implementation and evaluation of a dynamic multi-vane collimator system.” *Int. J. Radiat. Oncol. Biol. Phys.* 17(5):1080–1094.

Lewitt, R. M. (1979). “Processing of incomplete measurement data in computed tomography.” *Med. Phys.* 6(5):414–417.

Li, H. S., H. E. Romeijn, and J. F. Dempsey. (2006). “A fourier analysis on the maximum acceptable grid size for discrete proton beam dose calculation.” *Med. Phys.* 33(9):3508–3518.

Li, X. A., A. Tai, D. W. Arthur, T. A. Buchholz, S. MacDonald, L. B. Marks, et al. (2009). “Variability of target and normal structure delineation for breast cancer radiotherapy: an RTOG multi-institutional and multiobserver study.” *Int. J. Radiat. Oncol. Biol. Phys.* 73(3):944–951.

Li, G., H. Xie, H. Ning, D. Citrin, J. Capala, R. Maass-Moreno, et al. (2008). “Accuracy of 3D volumetric image registration based on CT, MR and PET/CT phantom experiments.” *J. Appl. Clin. Med. Phys.* 9(4):2781.

Li, H. (2010). “A CT-based software tool for evaluating compensator quality in passively scattered proton therapy.” *Phys. Med. Biol.* 55(22):6759–6771.

Li, H., N. Sahoo, F. Poenisch, K. Suzuki, Y. Li, X. Li, X. Zhang, A. K. Lee, M. T. Gillin, and X. R. Zhu. (2013). "Use of treatment log files in spot scanning proton therapy as part of patient-specific quality assurance." *Med. Phys.* 40(2):021703.

Li, T., Z. Liang, J. V. Singanallur, T. J. Satogata, D. C. Williams, and R. W. Schulte. (2006). "Reconstruction for proton computed tomography by tracing proton trajectories: A Monte Carlo Study." *Med. Phys*. 33(3):699–706.

Li, Y., L. Kardar, X. Li, H. Li, W. Cao, J. Y. Chang, L. Liao, R. X. Zhu, N. Sahoo, M. Gillin, Z. Liao, R. Komaki, J. D. Cox, G. Lim, and X. Zhang. (2014). "On the interplay effects with proton scanning beams in stage III lung cancer." *Med. Phys.* 41(2):021721.

Lin, L., C. G. Ainsley, and J. E. McDonough. (2013). "Experimental characterization of two-dimensional pencil beam scanning proton spot profiles." *Phys. Med. Biol.* 58(17):6193–6204.

Lin, L., M. Kang, S. Huang, R. Mayer, A. Thomas, T. D. Solberg, J. E. McDonough, and C. B. Simone. (2015). "Beam-specific planning target volumes incorporating 4D CT for pencil beam scanning proton therapy of thoracic tumors." *J. Appl. Clin. Med. Phys.* 16:281–292.

Linz, U. *Ion Beam Therapy Fundamentals, Technology, Clinical Applications.* Berlin: Springer-Verlag, 2012.

Liu, F., B. Erickson, C. Peng, and X. A. Li. (2012). "Characterization and management of interfractional anatomic changes for pancreatic cancer radiotherapy." *Int. J. Radiat. Oncol. Biol. Phys.* 83(3):e423–429.

Liu, W., X. Zhang, Y. Li, and R. Mohan. (2012). "Robust optimization of intensity modulated proton therapy." *Med. Phys.* 39:1079–1091. Can be found at: http://www.ncbi.nlm.nih.gov/pubmed/22320818.

Liu, W., S. J. Frank, X. Li, Y. Li, P. C. Park, L. Dong, X. R. Zhu, and R. Mohan. (2013). "Effectiveness of robust optimization in intensity-modulated proton therapy planning for head and neck cancers." *Med. Phys.* 40:051711. Can be found at: http://www.ncbi.nlm.nih.gov/pubmed/23635259.

Liu, W., S. J. Frank, X. Li, Y. Li, X. R. Zhu, and R. Mohan. (2013). "PTV-based IMPT optimization incorporating planning risk volumes vs robust optimization." *Med. Phys.* 40(2):021709. Can be found at: http://www.ncbi.nlm.nih.gov/pubmed/23387732.

Lomax, A. J. (2008). "Intensity modulated proton therapy and its sensitivity to treatment uncertainties 2: the potential effects of inter-fraction and inter-field motions." *Phys. Med. Biol.* 53(4):1043–1056.

Low, D. A., W. B. Harms, S. Mutic, and J. A. Purdy. (1998). "A technique for the quantitative evaluation of dose distributions." *Med. Phys.* 25(5):656–661.

Lu, H.-M. and H. Kooy. (2006). "Optimization of current modulation function for proton spread-out Bragg peak fields." *Med. Phys.* 33(5):1281–1287.

Lu, H. M., B. Brett, M. Engelsman, R. Slopsema, H. Kooy, and J. Flanz. (2007). "Sensitivities in the production of spread-out Bragg peak dose distributions by passive scattering with beam current modulation." *Med. Phys.* 34(10):3844–3853.

Ludewigt, B., J. Bercovitz, M. Nyman, and W. Chu. "Method for selecting minimum width of leaf in multileaf adjustable collimator while inhibiting passage of particle beams of radiation through sawtooth joints between collimator leaves." *US Letters Patent No. 5,438,454.* Issued: August 01, 1995.

Mahmood, U., M. Errens, A. Zimrin, N. Hanna, P. Amin, and N. Sharma. (2012). "The remarkably distensible stomach: Case report highlighting the implications of gastric filling on radiation treatment planning for gastric lymphoma." *Pract. Radiat. Oncol. 2*(4):265–269.

Mah, D., H. Hanley, K. E. Rozenweig, E. Yorke, L. Braban, C. C. Ling, S. A. Leibel, and G. Mageras. (2000). "Technical aspects of the deep inspiration breath-hold technique in the treatment of thoracic cancer." *Int. J. Radiat. Oncol. Biol. Phys.* 48(4):1175–1185.

Mak, D., S. Gill, R. Paul, A. Stillie, A. Haworth, T. Kron, J. Cramb, K. Knight, J. Thomas, G. Duchesne, and F. Foroudi. (2012). "Seminal vesicle interfraction displacement and margins in image guided radiotherapy for prostate cancer." *Radiat. Oncol.* 7:139–147.

Maleike. D., J. Unkelbach, and U. Oelfke. (2006). "Simulation and visualization of dose uncertainties due to interfractional organ motion." *Phys. Med. Biol.* 51(9):2237–2252.

Markelj, P., D. Tomazevic, B. Likar, and F. Pernus. (2012). "A review of 3D/2D registration methods for image-guided interventions." *Med. Image Anal.* 16(3):642–661.

Mesoloras, G., G. Sandison, R. D. Stewart, J. G. Farr, and W. C. Hsi. (2006). "Neutron scattered dose equivalent to a fetus from proton radiotherapy of the mother." *Med. Phys.* 33(7):2479–2490.

Millner, M. R., W. D. McDavid, R. G. Waggener, M. J. Dennis, W. H. Payne, and V. J. Sank. (1979). "Extraction of information from CT scans at different energies." *Med. Phys.* 6(1):70–71.

Moignier, A., E. Gelover, D. Wang, B. Smith, R. Flynn, M. Kirk, L. Lin, T. Solberg, A. Lin, and D. Hyer. (2015). "Theoretical benefits of dynamic collimation in pencil beam scanning proton therapy for brain tumors: dosimetric and radiobiological metrics." *Int. J. Radiat. Oncol. Biol. Phys.* 95(1):171–180.

Moyers, M. F. "Proton Therapy." In *The Modern Technology of Radiation Oncology: A Compendium for Medical Physicists and Radiation Oncologists,* J. Van Dyk, ed. Madison, WI: Medical Physics Publishing, 1999.

Moyers, M. F. "LLUPTF: eleven years and beyond." In *Nuclear Physics in the 21st Century.* New York: American Institute of Physics, 2002.

Moyers, M. F. "Method and device for delivering radiotherapy." *International Patent Cooperation Treaty Publication Number WO 0131039212 A1, PCT/US02/34556.* Issued: June 7, 2004. *U.S. Letters Patent No. 6,769,806.* Issued: August 3, 2004.

Moyers, M. F. (2008). "Basics of Light Ion Treatments: Depth Dose and Range." Proton Therapy Educational Workshop, Jacksonville, Florida, May 19–24, 2008.

Moyers, M. F. (2010). "NCI/RPC Initiative for approval of proton facilities to participate in inter-institutional clinical trials." Presented at the ICRU Annual Meeting, Essen, Germany, November 17, 2010.

Moyers, M. F. (2011). "Comparison of CTN to Proton RLSP Conversion Functions." Presented at the Particle Therapy Co-operative Group meeting, Philadelphia, Pennsylvania, May 12–14, 2011.

Moyers, M. F. (2014). "Comparison of x-ray computed tomography number to proton relative linear stopping power conversion functions using a standard phantom." *Med. Phys.* 41(6):061705.

Moyers, M. F. and W. Lesyna. (2004). "Isocenter characteristics of an external ring proton gantry." *Int. J. Radiat. Oncol. Biol. Phys.* 90(5):1622–1630.

Moyers, M. F. and A. Ghebremedhin. (2008). "Spill-to-spill and daily proton energy consistency with a new accelerator control system." *Med. Phys.* 35(5):1901–1905.

Moyers, M. F. and D. W. Miller. (2003). "Range, range modulation and field radius requirements for proton therapy of prostate cancer." *Technol. Cancer Res. Treat.* 2(5):445–447.

Moyers, M. F. and J. V. Siebers. (1995). "Charged particle beam scattering system." *U.S. Letters Patent No. 5,440,133* Issued: August 8, 1995. *European Letters Patent No. 0740569 Korean Letters Patent No. 0341511.*

Moyers, M. F., D. W. Miller, J. V. Siebers, R. Galindo, S. Sun, M. Sardesai, and L. Chan. (1992). "Water equivalence of various materials for 155 to 250 MeV protons." *Med. Phys.* 19(3):829.

Moyers, M. F., P. B. Saganti, and G. A. Nelson. (2006). "EVA space suit proton and electron threshold penetration energies by XCT and rangeshifting." *Radiat. Meas.* 41(9–10):1216–1226.

Moyers, M. F., G. B. Coutrakon, A. Ghebremedhin, K. Shahnazi, P. Koss, and E. Sanders. (2007). "Calibration of a proton beam energy monitor." *Med. Phys.* 34(6):1952–1966.

Moyers, M. F., M. Sardesai, S. Sun, and D. W. Miller, D. W. (2010). "Ion stopping powers and CT numbers." *Med. Dosim.* 35(3):179–194.

Moyers, M. F. and S. M. Vatnitsky. *Practical Implementation of Light Ion Beam Treatments.* Madison, WI: Medical Physics Publishing, 2012.

Moyers, M. F., G. S. Ibbott, R. L. Grant, P. A. Summers, and D. S. Followill. (2014). "Independent dose per monitor unit review of eight U.S.A. proton treatment facilities." *Med. Phys.* 41(1):012103, 1–5.

Mustafa, A. A. and D. F. Jackson. (1983). "The relation between x-ray CT numbers and charged particle stopping powers and its significance for radiotherapy treatment planning." *Phys. Med. Biol.* 28(2):169–176.

Mutic, S., J. R. Palta, E. K. Butker, I. J. Das, M. S. Huq, L. N. Loo, et al. (2003). "Quality assurance for computed-tomography simulators and the computed-tomography-simulation process: report of the AAPM Radiation Therapy Committee Task Group No. 66." *Med. Phys.* 30(10):2762–2792.

Myerson, R. J., M. C. Garofalo, I. El Naga, R. A. Abrams, A. Apte, W. R. Bosch, et al. (2009). "Elective clinical target volumes for conformal therapy in anorectal cancer: a radiation therapy oncology group consensus panel contouring atlas." *Int. J. Radiat. Oncol. Biol. Phys.* 74(3):824–830.

Njeh, C. F. (2008). "Tumor delineation: the weakest link in the search for accuracy in radiotherapy." *J. Med. Phys.* 33(4):136–140.

Newhauser, W., J. Fontenot, Y. Zheng, J. Polf, U. Titt, N. Koch, et al. (2007). "Monte Carlo simulations for configuring and testing an analytical proton dose-calculation algorithm." *Phys. Med. Biol.* 52(15):4569–4584.

Newhauser, W. D., A. Giebeler, K. M. Langen, D. Mirkovic, and R. Mohan. (2008). "Can megavoltage computed tomography reduce proton range uncertainties in treatment plans for patients with large metal implants?" *Phys. Med. Biol.* 53(9):2327–2344.

Ng, M., T. Leong, S. Chander, J. Chu, A. Kneebone, S. Carroll, et al. (2012). "Australasian Gastrointestinal Trials Group (AGITG) contouring atlas and planning guidelines for intensity-modulated radiotherapy in anal cancer." *Int. J. Radiat. Oncol. Biol. Phys.* 83(5):1455–1462.

Nichiporov, D., W. Hsi, and J. Farr. (2012). "Beam characteristics in two different proton uniform scanning systems: a side-by-side comparison." *Med. Phys.* 39(5):2559–2568.

Niemierko, A. (1987). "Reporting and analyzing dose distributions: A concept of equivalent uniform dose." *Med. Phys.* 24(1):103–110.

Paganetti, H., H. Jiang, K. Parodi, R. Slopsema, and M. Engelsman. (2008). "Clinical implementation of full Monte Carlo dose calculation in proton beam therapy." *Phys. Med. Biol.* 53(17):4825–4853.

Paganetti, H. *Proton Therapy Physics.* New York: CRC Press, 2012.

Paganetti, H. (2012). "Range uncertainties in proton therapy and the role of Monte Carlo simulations." *Phys. Med. Biol.* 57(11):R99–R117.

Palmans, H. and S. Vatnitsky. "Dosimetry and beam calibration." In *Principles and Practice of Proton Beam Therapy* (AAPM 2015 Summer School), I. J. Das and H. Paganetti, eds. Madison, WI: Medical Physics Publishing, 2015.

Palta, J. R. and T. R. Mackie. *Uncertainties in External Beam Radiation Therapy.* Madison, WI: Medical Physics Publishing, 2011.

Park, P. C., X. R. Zhu, A. K. Lee, N. Sahoo, A. D. Melancon, L. Zhang, and L. Dong. (2012). "A beam specific planning target volume (PTV) design for proton therapy to account for setup and range uncertainties." *Int. J. Radiat. Oncol. Biol. Phys.* 82(2):e329–336.

Parkes, M. J., S. Green, A. M. Stevens, S. Parveen, R. Stephens, and T. H. Clutton-Brock. (2016). "Safely prolonging single breath-holds to >5 min in patients with cancer, feasibility and applications for radiotherapy." *Br. J. Radiol.* 89:1–9.

Pedroni, E., S. Scheib, T. Boehringer, A. Coray, M. Grossmann, S. Lin, and A. Lomax. (2005). "Experimental characterization and physical modelling of the dose distribution of scanned proton pencil beams." *Phys. Med. Biol.* 50(3):541–561.

Peterson, S., J. Polf, G. Ciangaru, S. J. Frank, M. A. Bues, and A. Smith. (2009). "Variations in proton scanned beam dose delivery due to uncertainties in magnetic beam steering." *Med. Phys.* 36(8):3693–3702.

Petterson, M., N. Blumenkrantz, J. Feldt, J. Heimann, D. Lucia, A. Seiden, D. C. Williams, H. F.-W. C. Sadrozinski, V. Bashkirov, R. Schulte, M. Bruzzi, D. Menichelli, M. Scaringella, C. Talamonti, G. A. P. Cirrone, G. Cuttone, D. Lo Presti, N. Randazzo, and V. Sipala. (2006). "Proton Radiography Studies for Proton CT." *IEEE Nuclear Science Symposium Conference Record, October 29–November 1, 2006, San Diego, California.* ISBN:1-4244-0560-2.

Pflugfelder, D., J. Wilkens, and U. Oelfke. (2008). "Worst case optimization: a method to account for uncertainties in the optimization of intensity modulated proton therapy." *Phys. Med. Biol.* 53:1689–1700.

Ploguin, N., A. Rangel, and P. Dunscombe. (2008). "Phantom evaluation of a commercially available three modality image guided radiation therapy system." *Med. Phys.* 35(12):5303–5311.

Remouchamps, V. M., N. Letts, F. A. Vicini, M. B. Sharpe, L. L. Kestin, P. Y. Chen, A. A. Martinez, and J. W. Wong. (2003). "Initial clinical experience with moderate deep-inspiration breath hold using an active breathing control device in the treatment of patients with left-sided breast cancer using external beam radiation therapy." *Int. J. Radiat. Oncol. Biol. Phys.* 56(3):704–715.

Romano, M., C. Cavedon, A. B. Porcaro, and A. Grandinetti. (2013). "Does preradiation oxygen breathing prolong deep inspiration breath hold?" *Int. J. Radiat. Oncol. Biol. Phys.* 87(2):S66.

Rutherford, R. A., B. R. Pullan, and I. Isherwood. (1976). "X-ray energies for effective atomic number determination." *Neuroradiology* 11:23–28.

Sahoo, N., X. R. Zhu, B. Arjomandy, G. Ciangaru, M. Lii, R. Amos, R. Wu, and M. T. Gillin. (2008). "A procedure for calculation of monitor units for passively scattered proton radiotherapy beams." *Med. Phys.* 35(11): 5088–5097.

Sawakuchi, G. O., X. R. Zhu, F. Poenisch, K. Suzuki, G. Ciangaru, U. Titt, A. Anand, R. Mohan, M. T. Gillin, and N. Sahoo. (2010). "Experimental characterization of the low-dose envelope of spot scanning proton beams." *Phys. Med. Biol.* 55(12):3467–3478.

Schardt, D., P. Steidl, M. Krämer, U. Weber, K. Parodi, and S. Brons. (2008). "GSI Scientific Report 2007." *GSI Report No.* 2008-1:373.

Schaffner, B. and E. Pedroni. (1998). "The precision of proton range calculations in proton radiotherapy treament planning: experimental verification of the relation between CT-HU and proton stopping power." *Phys. Med. Biol.* 43:1579–1592.

Schippers, J. M., J. Duppich, G. Goitein, M. Jermann, A. Lomax, E. Pedronis, H. Reist, B. Timmermann, and J. Verweij. (2006). "The use of protons in cancer therapy at PSI and related instrumentation." *J. of Physics: Conference Series* 41:61–71.

Schneider, U. and E. Pedroni. (1994). "Multiple Coulomb scattering and spatial resolution in proton radiography." *Med. Phys.* 21(11):1657–1663.

Schneider, U. and E. Pedroni. (1995). "Proton radiography as a tool for quality control in proton therapy." *Med. Phys.* 22:353–363.

Schneider, U., E. Pedroni, and A. Lomax. (1996). "The calibration of CT Hounsfield units for radiotherapy treatment planning." *Phys. Med. Biol.* 41(1):111–124.

Schulte, R., V. Bashkirov, T. Li, Z. Liang, K. Mueller, J. Heimann, L. R. Johnson, B. Keeney, H. F. -W. Sadrozinski, A. Seiden, D. C. Williams, L. Zhang, Z. Li, S. Peggs, T. Satogata, and C. Woody. (2004). “Conceptual Design of a Proton Computed Tomography System for Applications in Proton Radiation Therapy.” *IEEE Trans. Nucl. Sci.* 51(3):866–872.

Schulte, R., V. Bashkirov, M. C. L. Klock, T. Li, A. J. Wroe, I. Evseev, D. C. Williams, and T. Satogata. (2005). “Density resolution of proton computed tomography.” *Med. Phys.* 32(4):1035–1046.

Schulthess, G. K. and H. J. Smith. *The Encyclopedia of Medical Imaging. Physics. Techniques and Procedures*. H. Petterson, ed. Oslo: The NIGER Institute, 1998.

Siewerdsen, J. H., I. A. Cunningham, and D. A. Jaffray. (2002). “A framework for noise-power spectrum analysis of multidimensional images.” *Med. Phys.* 29:2655–2671.

Sigmund, P., A. Schinner, and H. Paul. (2009). “Errata and Addenda for ICRU Report 73, Stopping of ions heavier than helium.” *J. ICRU* 5(1):1–10.

Slopsema, R. and H. Kooy. (2006). “Incorporation of the aperture thickness in proton pencil-beam dose calculations.” *Phys. Med. Biol.* 51:5441–5453.

Su, Z., O. Zeidan, et al. (2010). “Experimental Investigation of Dosimetric Impact of lntrafraction Target Motion during Proton Uniform Scanning Treatment using Polymer Gel Dosimeters and a 4D Phantom.” *Int. J. Radiat. Oncol. Biol. Phys.* 78(3):S801–S802.

Summers, P., G. Ibbott, M. Moyers, R. Grant, and D. Followill. (2012). “The Approval Process for the Use of Proton Therapy in NCI-Sponsored Clinical Trials.” *Med. Phys.* 39(6):3866.

Szymanowski, H. and U. Oelfke. (2002). “Two-dimensional pencil beam scaling: an improved proton dose algorithm for heterogeneous media.” *Phys. Med. Biol.* 47(18):3313–3330.

Takahashi, S. (1960). “A new device of Co-60 rotation therapy.” *Clin. Radiol.* 5:653–648.

Toita, T., T. Ohno, Y. Kaneyasu, T. Uno, R. Yoshimura, T. Kodaira, et al. (2010). “A consensus-based guideline defining the clinical target volume for pelvic lymph nodes in external beam radiotherapy for uterine cervical cancer.” *Jpn. J. Clin. Oncol.* 40 (5):456–463.

Torikoshi, M., S. Minohara, N. Kanematsu, M. Komori, M. Kanazawa, K. Noda, N. Miyahara, H. Itoh, M. Endo, and T. Kanai. (2007). “Irradiation system for HIMAC.” *J. Radiat. Res. Tokyo* 48:A15–A25.

Toth, T. L. “Image quality in CT: challenges and perspectives.” In *Radiation Dose from Multidetector CT,* D. Tack, M. K. Kalra, and P. A. Gevenois, eds. Berlin: Springer-Verlag, 2012.

Toth, T. L., E. Cesmeli, A. Ikhlef, and T. Horiuchi. (2005). “Image Quality and Dose Optimization Using Novel X-ray Source Filters Tailored to Patient Size.” *Proc. SPIE 5745, Medical Imaging 2005: Physics of Medical Imaging, 283* (August 30, 2005). doi:10.1117/12.595465.

Toth, T. L., N. B. Bromberg, T-S Pan, J. Rabe, S. J. Woloschek, J. Li, and G. E. Seidenschnur. (2000). “A dose reduction x-ray beam positioning system for high-speed multislice CT scanners.” *Med. Phys.* 27(12):2659–2668.

Toth, T. L., Z. Ge, and M. P. Daly. (2007). “The Influence of Patient Centering on CT Dose and Noise.” *Med. Phys.* 34(7):3093–3101.

Trofimov, A., J. Unkelbach, T. Delaney, and T. Bortfeld. (2012). “Visualization of a variety of possible dosimetric outcomes in radiation therapy using dose-volume histogram bands.” *J. Pract. Rad. Oncol.* 2(3):164–171.

Tsunashima, Y., T. Sakae, Y. Shioyama, K. Kagei, T. Terunuma, A. Nohtomi, and Y. Akine. (2004). “Correlation between the respiratory waveform measured using a respiratory sensor and 3D tumor motion in gated radiotherapy.” *Int. J. Rad. Oncol. Biol. Phys.* 60(3):951–958.

Tsunoo, T., M. Torikoshi, Y. Ohno, K. Uesugi, and N. Yagi. (2008). “Measurement of electron density in dual-energy x-ray CT with monochromatic x-rays and evaluation of its accuracy.” *Med. Phys.* 35:4924–4932.

Unkelbach, J., M. Alber, M. Bangert, R. Bokrantz, T. C. Y. Chan, J. O. Deasy, A. Fredriksson, B. L. Gorissen, M. van Herk, W. Liu, H. Mahmoudzadeh, O. Nohadani, J. V. Siebers, M. Witte, and H. Xu. (2018). "Robust radiotherapy planning." *Phys. Med. Biol.* 63(22):1–28.

Unkelbach, J., P. Botas, D. Giantsoudi, B. L. Gorissen, and H. Paganetti. (2016). "Reoptimization of intensity modulated proton therapy plans based on linear energy transfer." *Int. J. Radiat. Oncol. Biol. Phys.* 96(5):1097–1106**.**

Unkelbach, J., T. C. Y. Chan, and T. Bortfeld. (2007). "Accounting for range uncertainties in the optimization of intensity modulated proton therapy." *Phys. Med. Biol.* 52:2755–2773.

Unkelbach, J., B. Martin, M. Soukup, and T. Bortfeld. (2009). "Reducing the sensitivity of IMPT treatment plans to setup errors and range uncertainties via probabilistic treatment planning." *Med. Phys.* 36:149–163.

Urie, M., M. Goitein, and M. Wagner. (1983). "Compensating for heterogeneities in proton therapy." *Phys. Med. Biol.* 29(5):553–566.

Van Dyk, J., J. J. Battista, and G. S. Bauman. "Accuracy and uncertainty considerations in modern radiation oncology." In *The Modern Technology of Radiation Oncology*: *A Compendium for Medical Physicists and Radiation Oncologists,* vol. 3, J. Van Dyk, ed. Madison, WI: Medical Physics Publishing, 2013.

van Herk, M., P. Remeijer, C. Rasch, and J. V. Lebesque. (2000). "The probability of correct target dosage: dose-population histograms for deriving treatment margins in radiotherapy." *Int. J. Radiat. Oncol. Biol. Phys.* 47(4):1121–1135.

Vatnitsky, S. M. and M. F. Moyers. "Radiation therapy with light ions." In *The Modern Technology of Radiation Oncology, A Compendium for Medical Physicists and Radiation Oncologists,* vol. 3*.,* J. Van Dyk, ed. Madison, WI: Medical Physics Publishing, 2013.

Velec, M., J. L. Moseley, T. Craig, L. A. Dawson, and K. K. Brock. (2012). "Accumulated dose in liver stereotactic body radiotherapy: positioning, breathing, and deformation effects." *Int. J. Radiat. Oncol. Biol. Phys.* 83(4):1132–1140.

Wambersie, A., P. M. Deluca, P. Andreo, and J. H. Hendry. (2004). "Light or heavy ions: a debate of terminology." *Radiother. Oncol.* 73(S2):iiii.

Weiss, E. and C. F. Hess. (2003). "The impact of gross tumor volume (GTV) and clinical target volume (CTV) definition on the total accuracy in radiotherapy: theoretical aspects and practical experiences." *Strahlenthe. Onkol.* 179(1):21–30.

Wilkens, J. J. and U. Oelfke. (2005). "Optimization of radiobiological effects in intensity modulated proton therapy." *Med. Phys.* 32(2):455–465.

Wrightstone, T., C. Crowell, M. Urie, and M. Goitein. *The Treatment Planning Program (RX): The User's Manual*. Boston: Massachusetts General Hospital, 1989.

Yamamoto, T., U. Langner, W. W. Loo, J. Shen, and P. J. Keall. (2008). "Retrospective analysis of artifacts in four-dimensional CT images of 50 abdominal and thoracic radiotherapy patients." *Int. J. Radiat. Oncol. Biol. Phys.* 72(4):1250–1258.

Yang, M., G. Virshup, J. Clayton, X. R. Zhu, R. Mohan, and L. Dong. (2010). "Theoretical variance analysis of single- and dual-energy computed tomography methods for calculating proton stopping power ratios of biological tissues." *Phys. Med. Biol.* 55:1343–1362.

Yang, M., X. R. Zhu, P. C. Park, U. Titt, R. Mohan, G. Virshup, J. E. Clayton, and L. Dong. (2012). "Comprehensive analysis of proton range uncertainties related to patient stopping-power-ratio estimation using the stoichiometric calibration." *Phys. Med. Biol.* 57(13):4095–4115.

Yester, M. V. and G. T. Barnes. (1977). "Geometrical Limitations of Computed Tomography (CT) Scanner Resolution." *Proc. SPIE, Appl. Opt. Instr. In Medicine VI* 127:296–303.

Yi, S. K., W. H. Hall, M. Mathai, A. B. Dublin, V. Gupta, J. A. Purdy, and A. M. Chen. (2012). "Validating the RTOG-endorsed brachial plexus contouring atlas: an evaluation of reproducibility among patients treated by intensity-modulated radiotherapy for head-and-neck cancer." *Int. J. Radiat. Oncol. Biol. Phys.* 82(3):1060–1064.

Yoon, M., J. S. Kim, D. Shin, S. Y. Park, S. B. Lee, D. Y. Kim, T. Kim, K. H. Shin, and K. H. Cho. (2008). "Computerized tomography-based quality assurance tool for proton range compensators." *Med. Phys.* 35(8):3511–3517.

Zenklusen, S. M., E. Pedroni, D. Meer, C. Bula, and S. Safai. (2011). "Preliminary investigations for the option to use fast uniform scanning with compensators on a gantry designed for IMPT." *Med. Phys.* 38(9):5208–5216.

Zhang, R. and W. D. Newhauser. (2009). "Calculation of water equivalent thickness of materials of arbitrary density, elemental composition and thickness in proton beam irradiation." *Phys. Med. Biol.* 54(6):1383–1395.

Zhang, R., P. J. Taddei, M. M. Fitzek, and W. D. Newhauser. (2010). "Water equivalent thickness values of materials used in beams of protons, helium, carbon and iron ions." *Phys. Med. Biol.* 55(9):2481–2493.

Zhao, L., G. Sandison, J. Farr, R. Zamenhoff, and M. Fitzek. (2008). "Measurement of initial respiration phase effect on simulated lung cancer treatment: A comparison between a proton beam passive scattering delivery system and a uniform scanning delivery system." *Int. J. Radiat. Oncol. Biol. Phys.* 72(1):S633–S634.

Zhu, T. C., H. Lin, and J. Shen. "Monitor unit (MU) calculation." In *Principles and Practice of Proton Beam Therapy* (AAPM 2015 Summer School), I. J. Das and H. Paganetti, eds. Madison, WI: Medical Physics Publishing, 2015.

Zhu, X. R., F. Poenisch, M. Lii, G. O. Sawakuchi, U. Titt, M. Bues, X. Song, X. Zhang, Y. Li, G. Ciangaru, H. Li, M. B. Taylor, K. Suzuki, R. Mohan, M. T. Gillin, and N. Sahoo. (2013). "Commissioning dose computation models for spot scanning proton beams in water for a commercially available treatment planning system." *Med. Phys.* 40(4):41723.

Zhu, X. R., F. Poenisch, X. Song, J. L. Johnson, G. Ciangaru, M. B. Taylor, M. Lii, C. Martin, B. Arjomandy, A. K. Lee, S. Choi, Q. N. Nguyen, M. T. Gillin, and N. Sahoo. (2011). "Patient-specific quality assurance for prostate cancer patients receiving spot scanning proton therapy using single-field uniform dose." *Int. J. Radiat. Oncol. Biol. Phys.* 81(2):552–559.

Zhu, X. R., N. Sahoo, X. Zhang, D. Robertson, H. Li, S. Choi, A. K. Lee, and M. T. Gillin. (2010). "Intensity modulated proton therapy treatment planning using single-field optimization: the impact of monitor unit constraints on plan quality." *Med. Phys.* 37(3):1210–1219.

Zygmanski, P., K. P. Gall, M. S. Z. Rabin, and S. R. Rosenthal. (2000). "The measurement of proton stopping power using proton-cone-beam computed tomography." *Phys. Med. Biol.* 45:511–528.

Appendix: List of Acronyms

2DRS	two-dimensional range shifter
ABC	active breathing control
BEV	beam's eye view
CMM	computerized measuring machine
CNC	computer numerically controlled
CSDA	continuous slowing down approximation
CT	computed tomography
CTV	clinical target volume
D/MU	dose per monitor unit
DECT	dual energy x-ray computed tomography
DF	detection function
DIBH	deep inspiration breath hold
DRR	digitally-reconstructed-radiograph
DTA	distance-to-agreement
DP_{80-20}	distal penumbra between the 80% and 20% dose values
DVH	dose volume histogram
EDM	electrical discharge machine
EFM	energy and fluence modulation
EUD	equivalent uniform dose
FDF	focal distribution function
FTV	field target volume
GTV	gross tumor volume
HU	Hounsfield unit
k_p	coverage factor
kVXCT	kilovoltage x-ray computed tomography
LAU	lateral alignment uncertainty
LP_{80-20}	lateral penumbra between the 80% and 20% dose values
MCS	multiple Coulomb scattering
MLC	multi-leaf collimator
MLFC	multi-layer Faraday cup
MLIC	multi-layer ionization chamber
MPO	multiple portal optimization
MU	monitor unit
MVXCT	megavoltage x-ray computed tomography
OAR	organ at risk
OTF	optical transfer function
PDF	probability density function
PMMA	polymethylmethacrylate
PTV	planning target volume
PRV	planning organ at risk volume

PUBD	penetration uncertainties due to beam delivery
PUPC	penetration uncertainties due to physical characterization
QA	quality assurance
QEF	quality equivalent filtration
RFOV	reconstructed field of view
RLSCP	relative linear scattering power
RLSTP	relative linear stopping power
SAD	source-to-axis distance
SD	standard deviation
SFOV	scan field of view
SID	source-to-imager distance
SPO	single portal optimization
SSD	source-to-skin distance
SXCTN	scaled x-ray computed tomography number
TPS	treatment planning system
URS	uniform range shifter
VSAD	virtual source-to-axis distance
WEQ	water equivalence
WED	water-equivalent depth
WET	water-equivalent thickness